HER●N

Contents

FRACTURE OF CONCRETE UNDER COMPLEX STRESS

J. G. M. van Mier
TNO Institute for Building Materials and Structures,
Rijswijk, The Netherlands
Formerly: Eindhoven University of Technology, Dept. of. Struct.
Engineering, Eindhoven, The Netherlands

Abstract

Results of displacement controlled multiaxial experiments on concrete are discussed in Part 1 of this paper. The experiments were carried out in a recently developed true triaxial apparatus for cubes of size $D = 100$ mm. The specimens were loaded between brushes. The scope of the experiments was rather wide, ranging from simple proportional loads paths to complicated paths, which involve changes of principal stresses. Main emphasis is laid on fracture modes, and the experiments suggest that failure of concrete, both in tensile and compressive loading combinations is a localized phenomenon. During the softening branch the specimens become highly non-uniformly loaded, and interactions with the experimental environment are very pronounced.

In Part 2, the outline for a physical model for concrete fracture is proposed. In principle the model also should apply for rock. The model is valid for loading combinations involving both tensile and compresive components such that brittle fracture prevails. The model is divided into three stages: microcracking, crack joining and localization. The crack joining phase is considered as a transition from distributed microcracking (which can be handeled in traditional continuum models), to localized macrocracking (which should be approached with a discrete model). A simple fracture mechanics solution is proposed, for explaining the shape of the softening branch in direct tension. These theoretical considerations lead, in combination with the experimental observations, to the conclusion that geometrical changes in the post-peak range form the major ingredients of the softening phenomenon. When assuming non-uniform displacement distributions, typical response of direct tension experiments loaded between non-rotatable loading platens can be explained. This is shown in the final part of the paper by means of a non-linear numerical simulation with the DIANA finite element package. The results strongly suggest that the widely accepted process zone model, which explains pre-pack microcracking on basis of typical post-peak behaviour, should be approached with some sceptisism. The physical processes underlying the pre- and post-peak stress-displacement response are basically different, and should be treated separately in material models. The proposed crack joining mechanism may serve as a transition in such a dual model.

2

Fracture of concrete under complex stress

Introduction

Concrete is a complex heterogeneous material, and its response under load, especially fracture nucleation and propagation mechanisms are hardly understood. When loading conditions become more diversified, fundamental knowledge on the behaviour of the material is required. As a result, the scope of the usual "material experiments", both in compression and tension should be extended to complex load paths. Micromechanisms should be studied, under the same complex load-paths, as these form the basis for observed "macro behaviour". Phenomenological formulations of macroscopic material behaviour become especially unwieldy when anisotropy (initial or load-induced), in combination with rotation of the loading axes occurs. In this case, for example, the description of macroscopic failure and damage surfaces becomes extremely difficult, and until now no such formulations are available in literature.

New theories require adequate experimental data, and especially in the post-peak regime (softening), as well as for complex multiaxial loads paths, hardly any results are available. Post-peak data for concrete under multiaxial states of stress have only recently been published for the case of standard triaxial tests [i.e. Ahmad & Shah 1982, Jamet etal. 1984, and Hurlbut 1985]. Non-proportional load paths have been investigated for the first time by Scavuzzo etal. 1983, but are restricted to the pre-peak region only.

In this paper, results of displacement controlled true triaxial experiments on concrete are reported. The scope of the load paths investigated was rather wide [Van Mier 1984b], ranging from uniaxial tension and compression to complex displacement-ratio paths and rotation experiments. Necessarily, only part of the experimental results are shown in Part 1 of this paper. Main objective of the study was to understand the mechanism known as "strain-softening", and in Part 2, a possible fracture mechanism is discussed, whereas also some numerical simulations of a tension experiment are shown. Modelling of micromechanisms seems inevitable in order to simulate certain behaviour observed in tension experiments. It is shown that the behaviour of the specimen is very much dependent on the prevailing boundary conditions, and that the obeserved response cannot be modelled when the widely accepted fracture process zone is adopted.

1 Displacement controlled multiaxial testing

The results, which are discussed in this part have been obtained in a triaxial apparatus, developed and tested during the period 1980–1984. Some of the results have been reported before [Van Mier 1984a, 1985, 1986a-b], but in this extensive paper some additional results can be reported in detail, and discussed in relation to some theoretical considerations [Part 2].

First in section 1.1, the experimental technique is explained. In the subsequent sections, some results of uniaxial compressive experiments are shown, and the results of displacement controlled multiaxial tests are discussed.

1.1 *Experimental technique*

In this section the experimental apparatus that was developed and built at Eindhoven University of Technology is described, and discussed in relation to previously developed multiaxial machines. First, attention is paid to the global lay-out of the multiaxial apparatus. Next, the choice of the loading application system is discussed, and the load and displacement measuring systems are explained in detail. The test-control system, as well as the data aquisition system are discussed shortly, whereafter attention is paid to the manufacturing method of the specimens. Finally, the scope of the complete experimental program is given.

Triaxial cubical apparatus

The apparatus developed is a servo-controlled triaxial machine, suitable for testing cubical specimens of size D = 100 mm. The apparatus consists of three identical loading frames that are hung in a fourth overall frame by means of steel cables. In Fig. 1.1, an
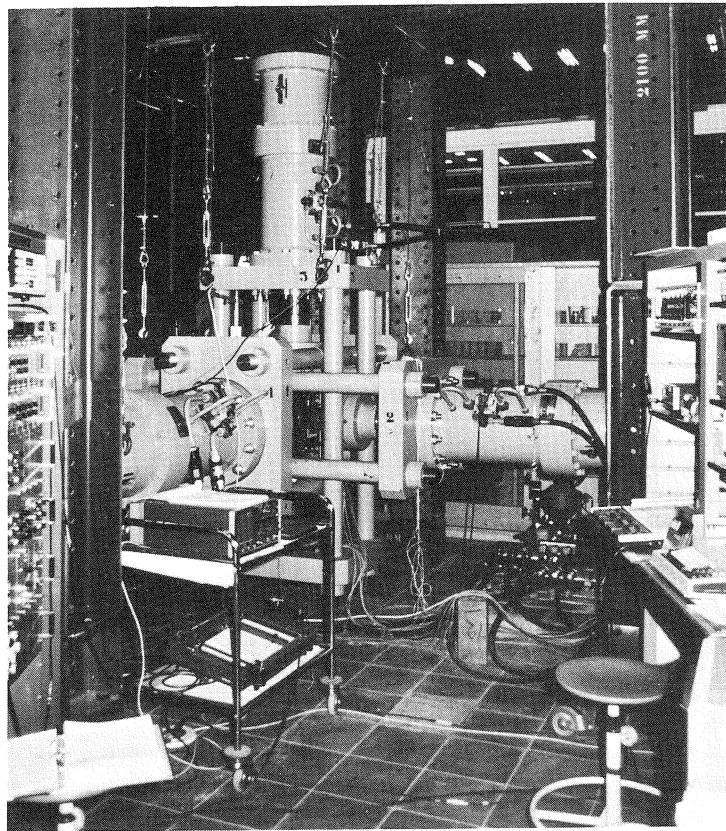

Fig. 1.1. General view of the triaxial apparatus.

4

deformed cube
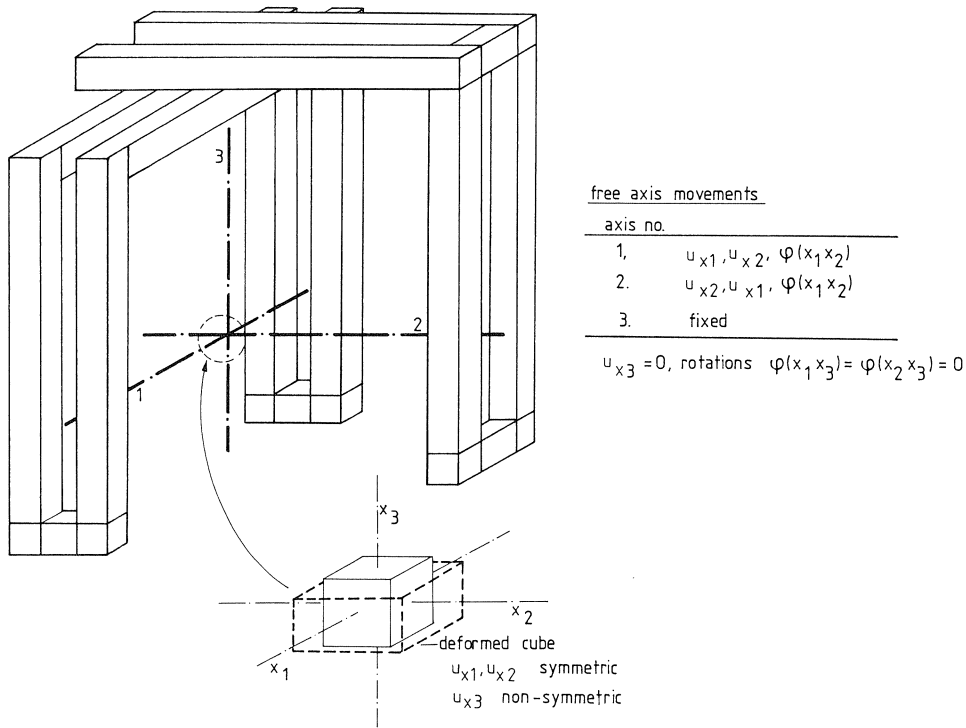u_{x1}, u_{x2} symmetric
u_{x3} non-symmetric

Fig. 1.2. Schematic view of the triaxial apparatus (movement of loading axes and specimen deformation).

overall view of the experimental machine is shown. The three loading axes are not connected to each other, and can act completely independent. Movement of the three axes with respect to each other is not restricted in the horizontal plane, in the vertical direction however, the frames are fixed. The translations and rotations of the three frames permitted, and the resulting specimen deformations are shown in Fig. 1.2. The deformations of the specimen are symmetric in the horizontal plane of the multiaxial apparatus, yet in the vertical direction non-symmetric deformations are applied to the concrete cube. Comparable multiaxial machines have been developed previously in Berlin [Schickert & Winkler 1977] and Munich [Linse 1978]. In the Munich triaxial machine the three loading axes were fixed to one another, and the specimen was deformed completely non-symmetric. In the machine developed in Berlin, either the axes could be fixed or could operate independently from each other, and from an extensive experimental study, Winkler [1985] concluded that the loading situation was more favourable when the three loading axes could move independently with regard to one another. In the current set up, the direction in which the smallest deformation was expected always was loaded in the vertical axis (non-symmetric deformations were applied to the specimen in this direction).

Fig. 1.3. Construction of a single loading axis.

1. frame rods
2. end-platens
3. hydraulic actuator
4. piston
5. spherical seating
6. load-cell
7. brush bearing platen
8. specimen, cube D = 100 mm
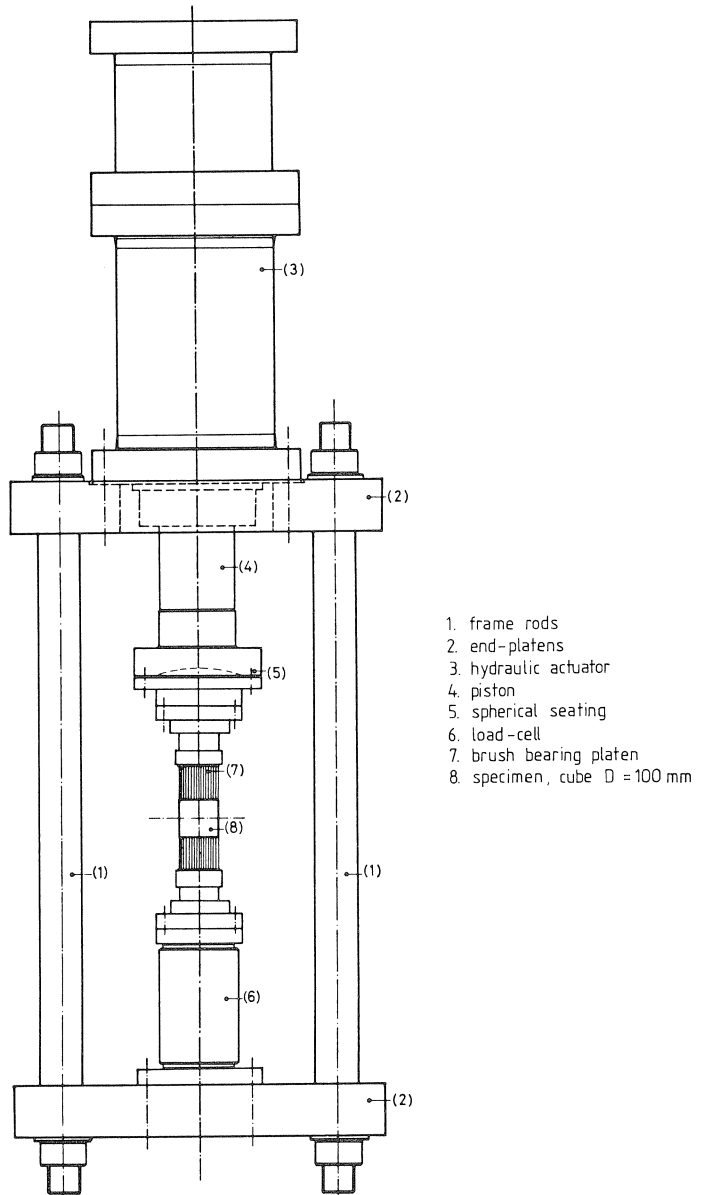
The construction of a single loading axis is shown in Fig. 1.3. Each loading axis consists of four steel rods (1), fixed in a rectangular configuration (as can be seen from Fig. 1.1) between two rigid steel end platens (2). At one side of this frame a 2MN compression/ 1.4 MN tension hydraulic actuator (3) is connected, and the piston (no. 4, stroke $\pm$ 100

mm) can move freely through an opening in the upper end-platen. At the piston side, a brush-bearing platen (7) is connected through a spherical seating (5). The radius of the spherical seating was chosen to ensure that the centre of rotation coincided with the specimen surface centre (cube D = 100 mm, no. 8). If desired, the spherical seating could be fixed during an experiment. As known from previous investigations [Newman & Sigvaldason 1965/1966 and Paterson 1978], the allowable rotations of the end-platens will have a considerable influence on the obtained result. In the triaxial experiments, as well as in the uniaxial tensile experiments, the spherical seating was fixed. Yet, it should be mentioned that rotations were allowed in a triaxial experiment in the horizontal plane as a direct result of the cable construction. In the uniaxial compressive experiments, the spherical seating was not fixed.

At the lower end-platen, the load-cell (6) was fixed. On top of this load-cell the second brush bearing platen was connected. Due to the chosen lay-out of the experimental machine, two right angles were present in the "triaxial chamber" at the load-cell sides (i.e. between the horizontal and vertical loading axes, see Fig. 1.2). This set-up required an extremely accurate setting of the loading axes with respect to each other, and consequently an accurate specimen manufacturing as well. Although sufficiently accurate specimens could be manufactured (by sawing cubes from initially larger blocks, and subsequently grinding them to the required size and shape), the application of a capping was considered favourable for the alignment of the specimen in the triaxial apparatus. By applying an epoxy-resin capping, also more reliable deformation measurements were obtained.

Loading application system

Several types of loading application systems have been developed and used in the past by many investigators. Globally four types can be distinguished: rigid loading platen (both used un cubical tests and in the axial direction in triaxial cylinder tests, e.g. [Ahmad & Shah 1982 and Jamet et al. 1984]), rigid loading platens with friction reducing measures by means of intermediate layers [e.g. rubber, Kobayahi & Koyanagi 1972; talc powder with aluminium sheets, Launay etal. 1970; polyethylene sheets with molybdenum sulfide grease, Bertacchi & Bellotti 1972; and teflon, Mills & Zimmerman 1970], non-rigid platens (brushes, originally developed by [Hilsdorf 1965], and later extensively used by others [e.g. Nelissen 1972, Kupfer 1973, Linse 1978]); flexible platens, [Schickert & Winkler 1977, Schickert 1980]; elastic supported brush packets, [Winkler 1985], and fluid cushions (applied in true triaxial tests on prismatic specimens [Ko & Sture 1974, Sture & Desai 1979, Andenaes et al. 1977, Michelis & Demiris 1984], but also for applying confining stress in conventional triaxial tests on cylinders). The above review is rather limited, but more comprehensive reviews are found in literature [e.g. Newman 1979]. Main purpose of all these systems is to apply a uniform state of stress to a material sample. It should be mentioned that this is not the case when rigid loading platens are used, but in many investigations (on cubical specimens), the method is used for comparison with friction reducing load application systems.

As mentioned before, in the current set-up the specimen was loaded by means of brush bearing platens. The brushes were chosen for several reasons. From one side the condition of unconstrained boundaries had to be fulfilled, on the other hand, also a uniform boundary displacement was needed in the displacement controlled experiments. Yet, the latter condition only is met when rigid steel platens are used, but then the first condition is violated. In this view, the brushes, which have been extensively tested in the past, were considered a good choice: friction between the specimen and the loading system is reduced due to the bending of the brush-rods, and the axial stiffness of the brushes resembles that of a rigid loading platen. Another reason was that with the brushes also tensile experiments could be carried out. In this context it should be mentioned that it was considered more favourable to use only one system in all experiments,
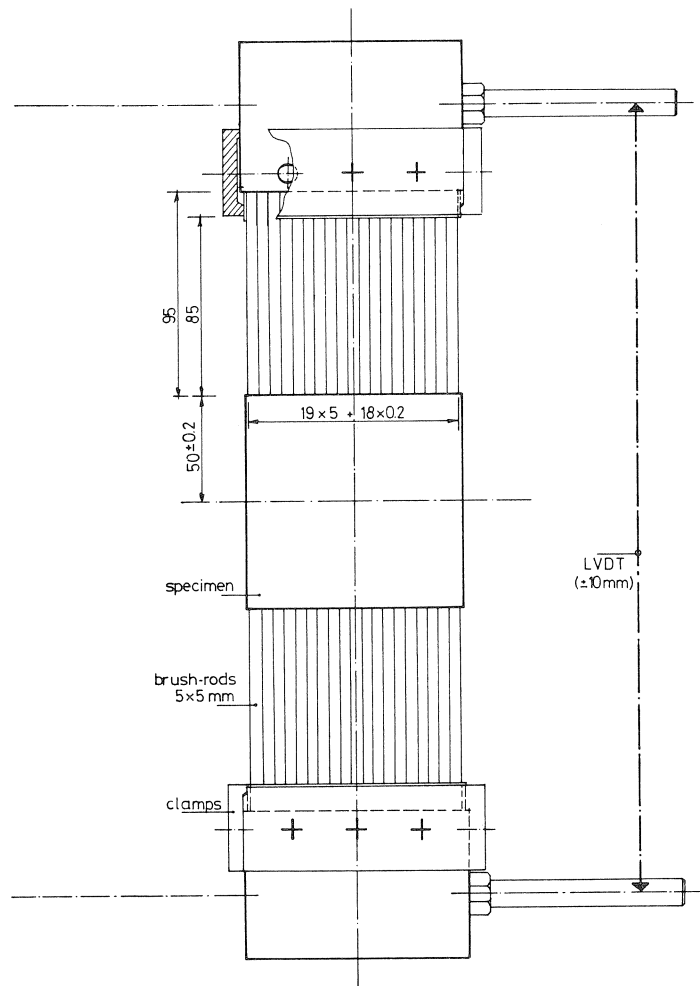

Fig. 1.4.   Brush construction and deformation measuring system.

rather than working with mixed boundary conditions (although recent tension-compression tests with mixed boundary conditions showed quite good results, see [Meier et al. 1985]).

In Fig. 1.4 the brush construction and deformation measuring system are shown. The brush rods (5×5 mm^2) are separated by means of a grid consisting of 0.2 mm thick phosfor bronze strips at the clamped side of the rods. The rod-packet is clamped as a whole at a solid steel block. The effective length of the rods is 85 mm. Due to the construction of the brushes, the specimen deformations were limited to approximately 3.0 mm.

Before starting each test series, the brushes were carefully ground. During grinding, 0.2 mm strips were inserted between the brush-rod-tips, and the complete rod-packet was rigidly clamped near the top in a special frame. A grinding sequence always started with the two inner contact surfaces (brush-rod packet – steel block interface). In view of the chosen deformation measuring system (i.e. measuring the relative displacement between two opposite loading platens, see Fig. 1.4), it was extremely important to avoid surface irregularities. In this context, the application of a capping was very favourable as well.

As mentioned, one of the reasons for choosing brushes was that also tensile experiments could be carried out. In this case, the rod-packet was glued to the steel block, and also an epoxy connection was made between the rod-packet and the concrete specimen. Before the specimen was glued between the brushes (which was done in the machine), a plastic filler was inserted between the brush rods in order to prevent intrusion of the epoxy between the rods. A similar technique was used before by other investigators [Nelissen 1972, Kupfer 1973 and Linse 1978].

Load and displacement measurements

Forces were measured by means of calibrated load-cells (no. 6 in Fig. 1.3). The load-cells consisted of a dumbell shaped steel measuring cylinder, upon which four strain-gauges were mounted in a full Wheatstone bridge configuration.
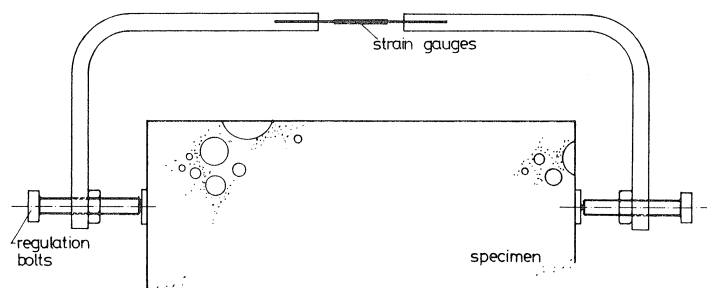

Fig. 1.5. Clip-gauge, used for measuring deformations in the "unstressed" direction(s).
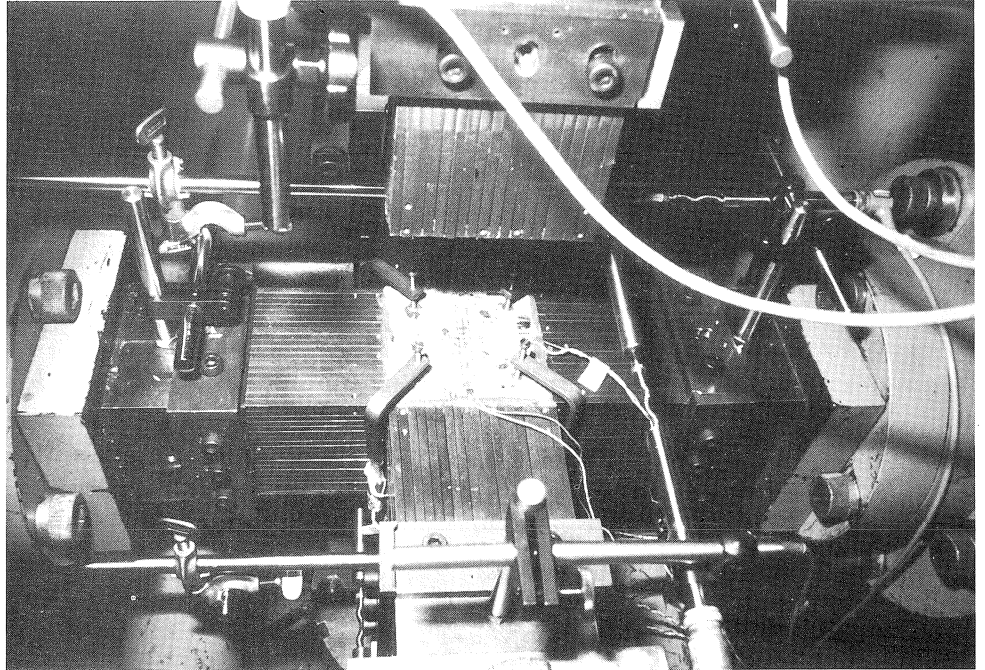
Fig. 1.6.   Fully instrumented biaxial compression test, showing the LVDT measurement, sur-
face measurement by means of strain-gauges, and the clip-gauges (which are attached
to the specimen in the corners between the brushes).

In the experiments, deformations were measured following three different methods,
depending on the type of test. Overall displacements were always measured by means of
LVDTs, as indicated in Fig. 1.4. Two or three LVDTs (stroke ± 10 mm) were attached to
the solid steel blocks upon which the brush rods were clamped, measuring the relative
displacement between two opposite loading platens. The LVDT-measurement was, as
mentioned, applied in all the experiments, and served in the closed loop servo-control.
In the uni- and biaxial experiments, that were carried out as a part of the testprogram,
additionally surface strain measurements were carried out by means of 60 mm long
strain gauges (type TML PL-60-11, polyester adhevise TML-PS). Furthermore, in the
uni- and biaxial experiments, strains in the unloaded direction(s) were measured by
using clip gauges (Fig. 1.5). In the middle (thin) part of a clip gauge two strain gauges
are mounted; the bending of the thin part is a measure of the displacement between the
regulation bolts. In Fig. 1.6, a fully instrumented biaxial experiment is shown. All de-
formation measuring methods were applied in this experiment. Needless to say that the
LVDT-measurement should be calibrated carefully. Details of this calibration can be
found elsewhere [Van Mier 1984b].

10

Test-control

Main differences between the current set-up and previous investigations [Kupfer 1973, Schickert & Winkler 1977, Linse 1978, Ko & Sture 1974, Sture & Desai 1979, Andenaes etal. 1977], is the circuit of regulation. The complete load-displacement diagram, including the softening branch, could be determined with the current apparatus, whereas a variety of different load paths could be applied very easily. A similar development has occured simultaneously in the field of rock-mechanics [Michelis & Demiris 1984], and of course standard triaxial compression and extension tests (using cylindrical specimens) in the softening region were possible for quite some time now, but have been used for testing concrete specimens only very recently [Ahmad & Shah 1982, Jamet etal. 1984 and Hurlbut 1985]. It should be mentioned that the machine developed by Michelis & Demiris operates under mixed boundary conditions. This is also the case in the standard triaxial tests where axial loading is applied through rigid steel platens, and confinement is applied through fluid pressure.

The regulation circuit for the triaxial experiments consists of a hydraulic and an electric part. The hydraulic part consisted of three servo-hydraulic actuators (Hydraudine, servo-valve MOOG model 76-375, capacity 28.5 l/min), connected through accumulators (SCHENCK PN 250 T) with a high pressure oil pump (SCHENCK PP-20B, 280–285 bar).

The electric part of the regulation circuit for a triaxial constant stress-ratio experiment ($\sigma_1/\sigma_2/\sigma_3 = 1/\alpha/\beta$, with α and β constant and $\alpha, \beta \leq 1$) with a constant displacement rate (du_1/dt = constant), is shown in Fig. 1.7. In this particular experiment, direction 1 (solid lines in Fig. 1.7) is in displacement control, while the other two directions are loaded in "force control", proportional to the major compressive stress σ_1 (dash-dotted line and dashed line for direction 2 and 3 respectively). In each loop a servo-controller (type SCHENCK-RV 35), and a carrier amplifier (type SCHENCK-MV-15 or Hottinger KWS 3073) were needed. The required load path was applied through an EXACT (model 340) materials testing generator. The regulation circuit could easily be adjusted for different load histories. For example, in the experimental program displacement-ratio test ($u_2/u_1 = \alpha, \alpha \leq 1$) and so-called "rotation paths" (with changing major stressed direction after some damage was sustained to a specimen) were investigated too. Results of displacement-ratio experiments will be discussed in this paper, as well as some limited results of the "rotation experiments". The results of the "rotation experiments" were published before in more detail [Van Mier 1985, 1986b].

For scanning the measuring devices, processing and storing data during an experiment, a computer controlled data logger (PEEKEL Autolog 900S System) was used. Loading was applied to a specimen continuously, and no stops were made for measuring purposes. In each measuring step, all the connected devices including the elapsed time (loads were measured at the beginning and end of each scan), were scanned and the data were stored on a floppy diskette for future processing. A typical scan took approximately 200–400 ms, in which a maximum stress increase of 0.10 N/mm^2 could occur. Two plotters were available for visual control of load-displacement response during an experiment.
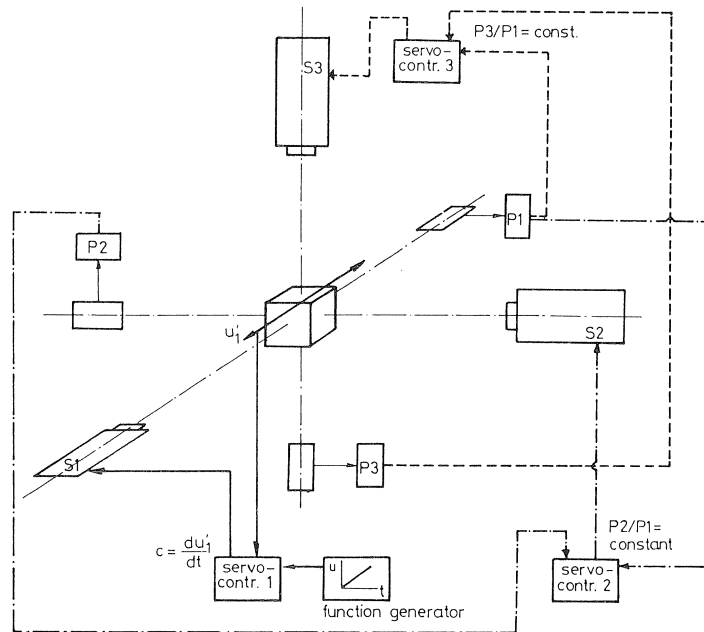
Fig. 1.7. Regulation circuit for constant stress-ratio experiments with a constant displacement rate (du_1/dt).

In the current report, results are presented as stress-strain curves or as stress-displacement curves. Stresses are determined by dividing the total load $P_{t,i}$ (i.e. the average value of the load measurement at the beginning and at the end of each scan) through the total cross-sectional area A_i of the specimen ($\sigma_i = P_{t,i}/A$), whereas strains are derived from the specimen displacements following $\varepsilon_i = u_i/H_i$, where H_i is the specimens dimension in the direction (i) in which the displacement (u_i) is measured. Needless to say that the displacements, measured with the overall displacement measuring system, were corrected for the brush deformations before these were translated into strains.

Specimens and materials

The triaxial apparatus was prepared for cubes with side D = 100 mm. Due to the relatively large stroke of the pistons, also prisms with a height up to 250 mm could be tested in the current configuration ($H/D = 2.5$).

The specimens (either 100 mm cubes or prisms with different height and cross-sectional area $A = 100 \times 100$ mm^2) were cast in larger blocks with dimensions $135 \times 135 \times 700$ mm^3. The blocks were cast horizontally. In the standard case, six cubes (D ≈ 103 – 104 mm) were sawn from the central part of the blocks after 28 days hardening under water,
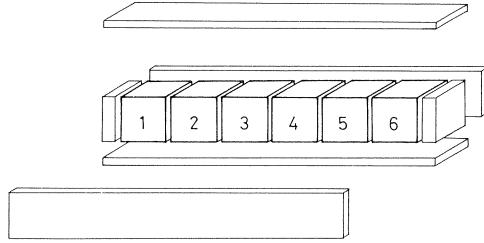
Fig. 1.8.   Cubes (D=100 mm), sawn from initial larger prisms.

mm) were sawn from the central part of the blocks after 28 days hardening under water, and by using a very stiff rotation diamond saw (see Fig. 1.8). After sawing, the opposite sides of the cubes were ground flat and parallel to each other of the required size (D = 100 mm) using a diamond grinding disk. The original prism size assured that a layer with thickness d_a (= maximum aggregate size = 16 mm) was removed from each side of the cubes. This largely eliminated the segregation effect which arose during hardening of the concrete. Also by using sawn specimens, the six surfaces of a cube were treated similarly.

For all tests the same concrete mix was used. The maximum aggregate size chosen was $d_a = 16$ mm. Consequently the ratio between cube size and maximum aggregate size $D/d_a = 6$–7, which was considered the minimum requirement for describing the concrete as a continuum. The grain size distribution of the aggregate (sand and gravel larger than 0.25 mm originated from the river Meuse at Panheel, the sand smaller than 0.25 mm was obtained from the Kempen), was taken according curve B16 of the Dutch Codes (NEN 3861) VB74, and is shown in Table 1.1. The cement content used was 320 kg/m^3, the type of cement being an ordinary portland cement (type A). The w/c ratio was chosen 0.5.

Table 1.1.   Grain size distribution of the aggregates used.

sieve-mesh (mm)	16–8	8–4	4–2	2–1	1–0.5	0.5–0.25	<0.25
%	24	20	14	10	12	12	8

The specimens were cast in batches containing two blocks (Fig. 1.8), three control cylinders (ø 100 x 250 mm) and 3–6 control cubes (150 mm). Two batches (A and B) always were cast on the same day. During casting, the specimens were vibrated (vibrating table, 50 Hz, centrifugal force 1 kN) for 180 seconds. Approximately 1 hour after casting, the specimens were vibrated a second time for 120 seconds. The casting surfaces were finished, and the specimens were placed under a plastic cap to avoid drying out. Two days after casting, the specimens were demoulded and placed in a fresh water basin. After 28 days the specimens were sawn and ground to the required size. The cubes were sealed (wet) in a plastic bag, and stored in a room with constant temperature

13

T = 20 °C. Two days before testing, the specimen was taken from the plastic bag, and strain gauges or other measuring devices were applied to the surfaces. The age at testing was always higher than 70 days.

Summary of experiments

In Table 1.2, a review is given of all experiments that were carried out. The different test-series are distinguished by their "batch number".
The loading speed of the uni- and triaxial experiments, using 100 mm cubes, was slightly different in the subsequent test-series. A specimen was always loaded with a constant displacement rate in the major compressive direction (or tensile direction when fracture prevailed in the tensile direction). For series 2/3 the displacement rate was equal to 0.5 μm/s, for series 5/6, 10 and 15, 1.0 μm/s, and in the triaxial experiments (series 8/9 and 7), du/dt = 1–2 μm/s. These differences in loading speed are very small and hardly will affect the results [Suaris & Shah 1982].

Table 1.2. Summary of experiments.

batch no.	short description	section
2A/2B 3A/3B	– uniaxial compression tests influence of manufacturing related parameters such as initial anisotropy and replicability	1.2
5A/5B/6A	– biaxial experiments preliminary experiments with variables load-path and monotonic/cyclic loading	1.3.2
7A/7B	– triaxial compression rotation experiments, with changing major and minor loading directions	1.5
8A/8B 9A/9B	– triaxial series main series of triaxial compression and tension-biaxial compression tests with variables load-path, initial anisotropy, and monotonic/cyclic loading	1.3 1.4
10A/10B	– uniaxial compression calibration of deformation measuring system, and size effect tests	1.2
15A	– uniaxial compression size effect tests	1.2

1.2 *Uniaxial experimental results*

Before the multiaxial experiments were carried out, a relatively large number of uniaxial displacement controlled compression tests' was carried out. Main purpose of these experiments was to determine possible systematic differences in stress-displacement behaviour of the cubes due to manufacturing related parameters. From these experiments some insight was gained regarding the homogeneity of the specimen deforma-

tions in relation to the observed fracture modes. The uniaxial results have been reported in detail in [Van Mier 1984a, b], and here only the most important results are discussed.

Scope of experiments

A total of 70 cubes and prisms was loaded in uniaxial compression between the brush bearing platens. All uniaxial experiments were carried out in the vertical axis of the triaxial apparatus.

In a first group of experiments manufacturing related parameters were investigated: the replicability between batches, the influence of initial anisotropy on the uniaxial stress-displacement behaviour, and the effect of different cube positions in the original prism before sawing was investigated (see Fig. 1.8).

In the second group of experiments, attention was paid on the complex deformational response of the specimen-brush system. In this series, prisms with different heights were tested: $h = 50$, 100 and 200 mm, with constant cross-sectional area $A = 100 \times 100$ mm^2. Extensive surface strain measurements were carried out in these experiments. In all experiments test-control was via the overall displacement measuring system (see Fig. 1.4). Lateral deformations were measured using the clip gauges, and in several experiments extensive surface strain measurements were carried out by means of 60 mm long strain gauges. Only in some of the prism tests also 30 mm gauges were used. The loading speed in the uniaxial compression tests (displacement rate) was equal to 0.5 to 1.0 μm/s.

In the following emphasis is placed on the influence of initial anisotropy on the uniaxial compressive stress-strain behaviour. Furthermore, the results of the surface strain measurements are discussed in relation to the structural changes that were observed in a specimen, and finally, the influence of the prism height on the stress-strain response is shown. Also these results are interpreted in terms of structural changes.

Initial anisotropy

The influence of the direction of loading with regard to the direction of casting is shown in Fig. 1.9. In Fig. 1.9.a, the axial stress-strain curves of a parallel loaded specimen and a perpendicular loaded cube are shown, and in Fig. 1.9.b and c, axial strain - lateral strain plots obtained from several experiments are depicted. In the ascending branch of the stress-strain curves, the initial slope is found to be smaller when loading is applied parallel. Eventually the peak stress-level is reached, the strain at peak stress being higher in the case of parallel loading. In the descending branch of the stress-strain curves, similar behaviour is observed, irrespective of the specimen's initial orientation. The differences in the pre-peak region could be explained from micro-structural differences, see Hughes & Ash [1970], and Van Mier [1985].

The implications in the lateral directions are shown in Fig. 1.9.b and c. In Fig. b, the axial strain - lateral strain plots of three perpendicular loaded cubes are shown, and in
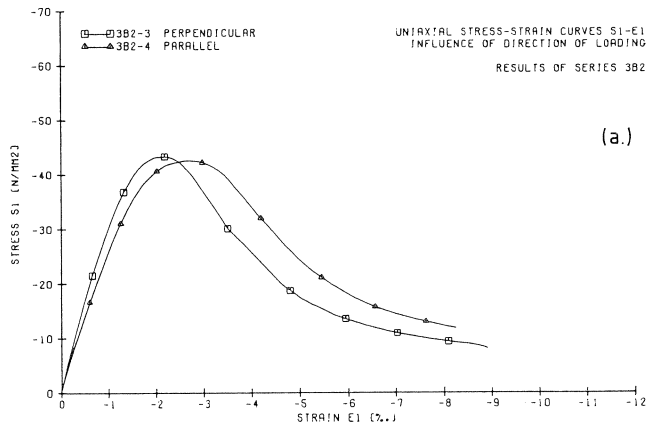
Fig. 1.9.a. Influence of initial anisotropy on the uniaxial stress-strain curve ($\sigma_1 - \varepsilon_{1,\text{loa.pl.}}$) in compression.
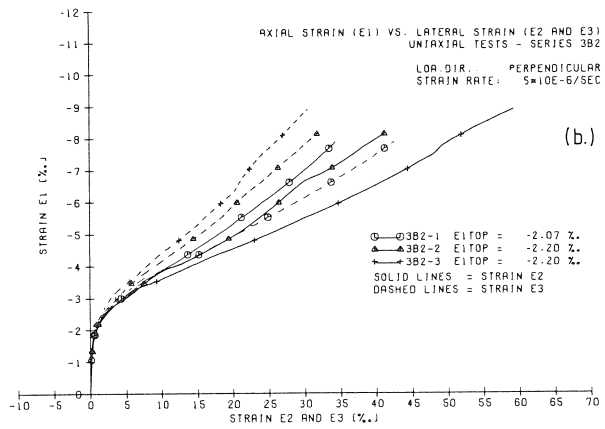
Fig. 1.9.b. Axial strain $\varepsilon_{1,\text{loa.pl.}}$ vs. lateral strains ε_2 and ε_3 for three perpendicular loaded specimens (resp. 3B2-1, 3B2-2 and 3B2-3).
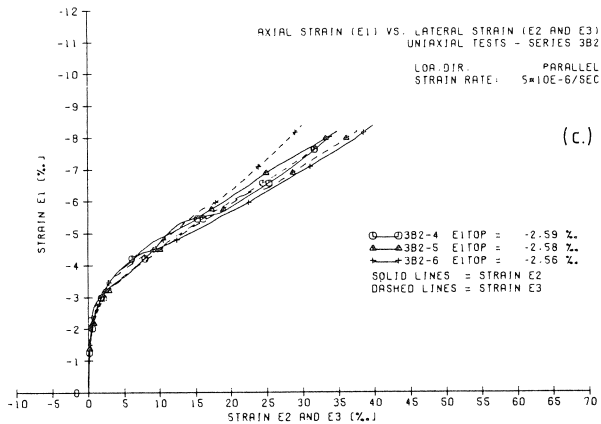
Fig. 1.9.c. Axial strain $\varepsilon_{1,\text{loa.pl}}$ vs. lateral strains ε_2 and ε_3 for three parallel loaded specimens (resp. 3B2-4, 3B2-5 and 3B2-6).

16

Fig. 1.10.   Definition of ε_2 and ε_3 in the case of perpendicular loading (a) and parallel loading (b), uniaxial loading.

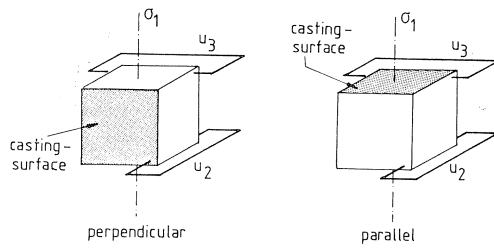Fig. c, the axial strain - lateral strain plots for three parallel loaded specimens. The axial strain at peak is indicated for each experiment. Always ε_2 is indicated with a solid line, whereas ε_3 is shown with a dashed line. Each line is the average result of two deformation measurements in the same direction (viz. the average value measured with the two diagonally placed clip gauges). The orientation of both ε_2 and ε_3 with regard to the casting surface is shown in Fig. 1.10. Beyond peak, these always show a sharp increase in lateral strains, suggesting severe cracking. In the perpendicular loaded experiments, the lateral strain measured in the direction of casting (i.e. perpendicular to the casting surface, ε_2) was generally larger than the lateral strain ε_3 (see Fig. 1.9.b). In contrast, in the parallel loaded specimens, ε_2 and ε_3 were almost equal to each other and all results were situated in a relatively narrow band (see Fig. 1.9.c). These results indicate that failure occurs dominantly in planes parallel to the casting surface when a cube is loaded perpendicular, whereas the loading situation is more uniform when a specimen is loaded parallel.

Note that the differences between ε_2 and ε_3 in the perpendicular loaded cubes is not systematic. Probably the results are affected by surface splitting which seemed to be a rather random process (see also the following section). As will be shown in section 1.3.4, in the triaxial experiments, where no surface splitting could occur, the effect was more systematic.

Surface strain measurements

In Fig. 1.11 the axial stress-strain curves for three parallel loaded cubes are shown. All cubes originated from the same initial prism (see Fig. 1.8). The solid lines in this figure are results obtained from the overall LVDT-measurement (between the two opposite loading platen $\varepsilon_{1,\text{loa.pl.}}$), the dashed lines are the stress-strain curves obtained from the surface strain measurement by means of the two central placed strain gauges ($\varepsilon_{1,\text{surf}}$). The replication of the uniaxial stress-strain curves was very good when the cubes originated from the same initial prism, whereas the differences became somewhat larger when results obtained from specimens originating from different batches were compared [see Van Mier 1984b].

The differences between overall (loading platen) strain measurement and the surface
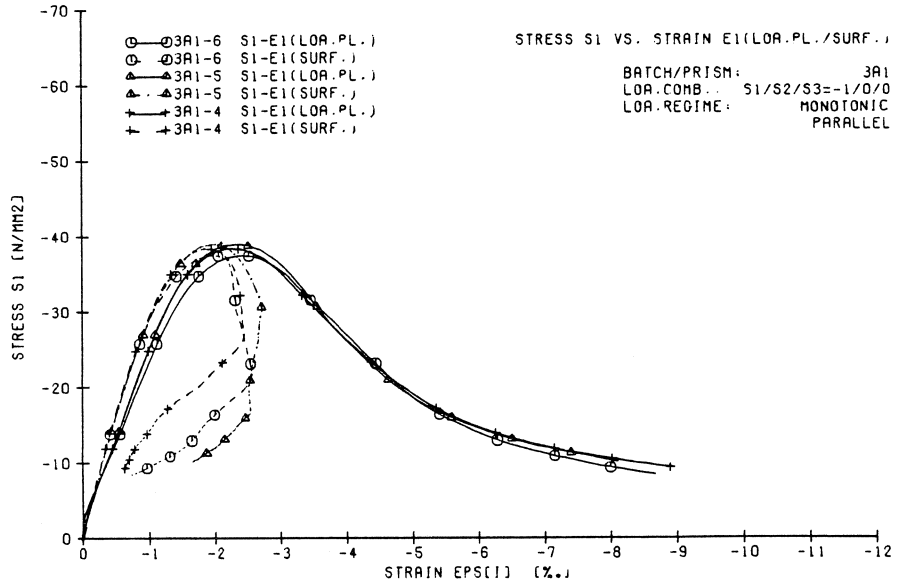
17

Fig. 1.11. Uniaxial stress-strain curves ($\sigma_1 - \varepsilon_{1,\text{loa.pl.}}$ and $\sigma_1 - \varepsilon_{1,\text{surf}}$) fot three parallel loaded specimens (3A1-4, 3A1-5 and 3A1-6).

strain measurement is striking. In the pre-peak region the surface strains $\varepsilon_{1,\text{surf}}$ always were smaller than the strain $\varepsilon_{1,\text{loa.pl.}}$, which was derived from the relative displacement between the two loading platens. The differences in pre-peak surface and overall strains were systematic. In some of the uniaxial compression tests a difference up to 30% of $\varepsilon_{1,\text{surf}}$ with respect to $\varepsilon_{1,\text{loa.pl.}}$ was measured. Similar differences were reported by Schickert [1980] using the flexible platen systems as well as dry steel platens as load application system in an extensive experimental research on concrete and mortar prisms subjected to uniaxial compression. The differences between $\varepsilon_{1,\text{surf}}$ and $\varepsilon_{1,\text{loa.pl.}}$ are mainly the result of the load application system and disturbances at the specimen - load application interface (in Van Mier [1984b] the subject is treated exhaustively). In the post-peak region the differences between $\varepsilon_{1,\text{surf}}$ and $\varepsilon_{1,\text{loa.pl.}}$ become very large. The overall strains increase, whereas the strains measured at the specimens surface decrease, suggesting that unloading takes place in the outer layers of the specimen. The "residual carrying capacity" of the now highly fractured specimen seems to be the result of the "more or less" intact specimen core. Similar results were reported by Kotsovos [1983] at the time when these experiments were carried out. The results indicate that in the post-peak region the specimen deformations are non-uniform, and that structural response rather than a material property is being measured in the descending branch of the stress-strain curve.

Six cubes were subjected to an extensive surface strain measurement. In the axial direction six strain gauges were mounted at two opposite surfaces of each cube (see Fig.
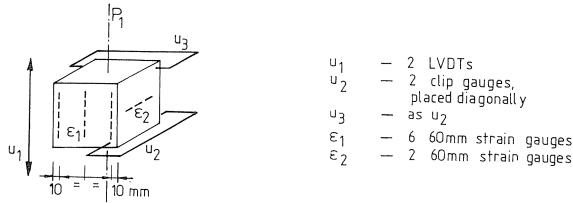
18

Fig. 1.12. Positions of measuring devices (clip gauges and strain gauges) in uniaxial compression tests series 3B2.

1.12). In Fig. 1.13a and b the separate strain-gauge readings of the six axial gauges are plotted against the elapsed time for both a perpendicular (3B2-2) and a parallel loaded specimen (3B2-6). Along the horizontal axis in these figures the elapsed time from the beginning of the experiment is given. The dashed-dotted lines which are drawn perpendicular to the time axis show where the peak stress-level σ_{1p} is reached (at $t = 500$ s for 3B2-6, and at $t = 465$ s for 3B2-2). In Fig. 1.14, the strain gauge locations for the two specimens are shown in a cross-section of the cube perpendicular to the direction of σ_1. The shaded area in the cross-section of specimen 3B2-2 indicates the upper surface of the specimen during casting. For the parallel loaded specimen 3B2-6 the casting surface does not appear in the relevant cross-section.

Up to peak stress level the strain gauge readings were situated in a relatively narrow band. The uniformity of the surface deformations was better for the parallel loaded specimen. For the perpendicular loaded specimen, the loading seemed initially to be
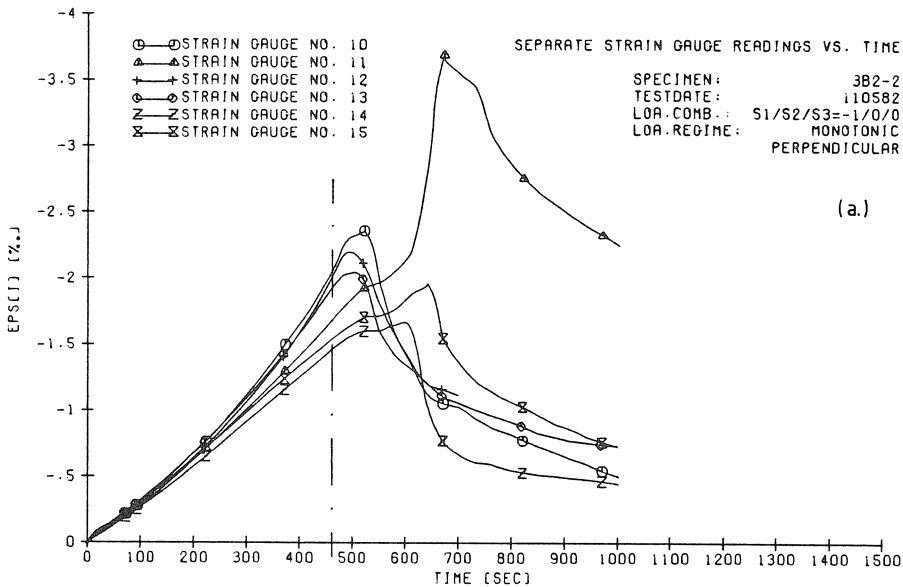

Fig. 1.13.a. Separate strain gauge readings vs. time for specimen 3B2-2, loading direction perpendicular.

19
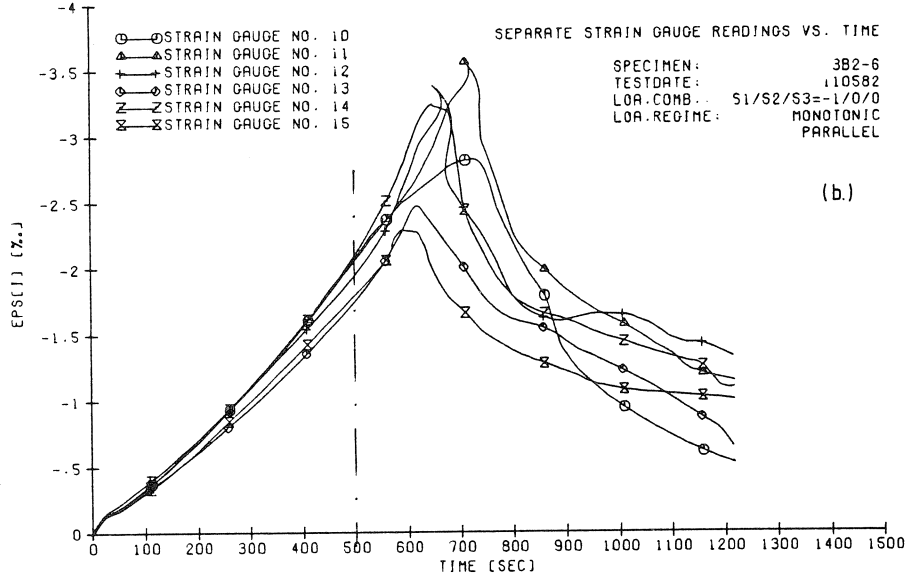
Fig. 1.13.b. Separate strain gauge readings vs. time for specimen 3B2-6, loading direction parallel.

rather centric (up to $\varepsilon_{1,\text{surf}} = -0.5\ ^0/00$), yet at higher levels of overall deformation, the loading became increasingly more excentric and at peak stress the strains measured at the casting surface (i.e. gauges no. 10, 12 and 13) were considerably larger than those measured at the opposite surface (no. 11, 14 and 15). Several factors may be responsible for this effect, but most important seems the fact that the density of the casting surface is less compared to that of the remainder of the specimen. These differences are a direct result of the method of making the specimens, and from these results it can be concluded that a larger portion of the initial prism (by increasing its size of course), has to be removed in order to obtain a more or less homogeneous specimen.

Now return to Fig. 1.13 and 1.14. The differences between the separate strain gauge readings become even more pronounced when the peak stress level is exceeded.

Fig. 1.14. Strain gauge locations and fracture propagation for specimens 3B2-2 (a) and 3B2-6 (b).

20

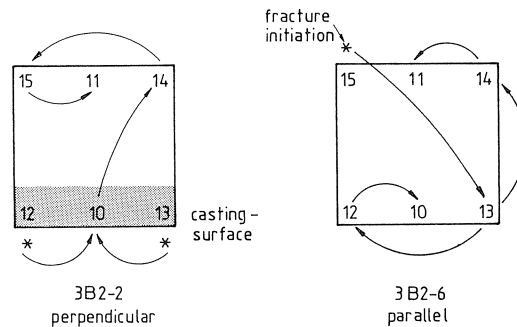Initially just beyond σ_{1p}, the surface strains continue to increase. Upon further axial straining (in terms of the loading platen strain $\varepsilon_{1,\text{loa.pl.}}$), a sudden unloading is observed at the specimen surface. In the case of the perpendicular loaded specimen this unloading is first observed for gauges no. 12 and 13 at t = 492 s (specimen 3B2-2, Fig. 1.13.a). For all three perpendicular loaded cubes, surface unloading was first observed near the casting surface. It is therefore not too hazardous to assume that fracture starts at the casting surface in the case of perpendicular loading. After a further increase of $\varepsilon_{1,\text{loa.pl.}}$, fracture (surface unloading) spreaded gradually throughout the complete specimen's cross-section as indicated in Fig. 1.14.

In the case of parallel loading also surface unloading was observed, yet fracture initiation did not occur at any particular place. As may be seen from Fig. 1.13.b, the pre-peak strains were located in a rather narrow band, which suggests that the cube is loaded more uniformly in this case. Note that surface unloading is delayed when a specimen is loaded parallel. In general the deviations between surface and loading platen measurement occured only after the specimen was loaded somewhat beyond peak.

Visible cracks (i.e visible with the naked eye) appeared in a specimen just beyond peak stress level, and the previous results indicate that macroscopic fracture starts with surface spalling, which seems to take place mainly in the first part of the descending branch before the inflection point in the overall stress-strain curve is reached. Stress redistributions take place in the specimen when the peak stress level is exceeded, and it seems that the remaining carrying capacity is due to a more or less intact core. Surface unloading in uniaxial compression was recently successfully simulated numerically by Ottosen [1984] by using a simple continuum softening model, and by Costin & Stone [1986] who used a microcrack model. Also the statistical parallel spring model developed by Bažănt & Panula [1978] should be mentioned, and which corresponds quite well with the physical nature of the strain-softening phenomenon. In these models al-
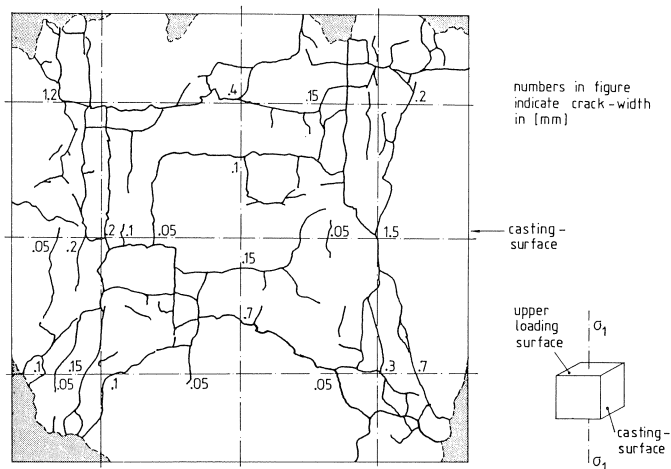

Fig. 1.15.   Crack pattern of the upper loading surface for specimen 2B2-3 after test termination (uniaxial compression, loading direction perpendicular).

ways the boundary conditions were assumed to correspond to rigid loading platens. Some further evidence in favour of the "intact core" model is shown in Fig. 1.15. Here the crack pattern of the upper loading surface of a perpendicular loaded specimen is shown. This particular specimen (2B2-3), was deformed up to $u_1 = 860$ μm, and the remaining deformation after unloading was 580 μm. The average lateral deformation for this specimen was determined from the four clip gauges and was equal to 3860 μm. In Fig. 1.15, only those cracks which were visible with the naked eye are shown. The shaded areas show where some material was torn loose. At three levels in the horizontal and vertical direction, the crack widths are indicated. The crack widths were measured under 10 x magnification. Close scrutiny of the crack widths shows that the cracks with the greatest widths are situated close to the edges of the specimen. In one case, near the casting surface even a crack width of 1.5 mm was measured. Although some cracks run through the centre, the widths of these cracks are limited (up to 0.15 mm). This may indicate that the innermost cracks are prevented from opening, probably still as a result of constraint between the brush platen and the specimen. In recent work by Ortiz [1986], this particilar crack pattern was refered to as evidence for distributed fracturing in uniaxial compression. However, even though the cracks seem to be distributed uniformly through the specimen, deformations and crack widths are highly non-uniform. Note in Fig. 1.15 the more or less rectangular crackpattern imposed to the specimen by the brushes.

The previous results strongly suggest that the measured stress-strain curve is the response of the complete system formed by the loading platen and the concrete specimen. During loading, and when large lateral deformations appear, bending of the brush-rods occurs, and a spherical loading platen "develops". Of course this effect was known before [Linse 1978], and has been shown to occur also when the flexible platen system is used [Schickert 1980]. The implications for fracture have now been demonstrated.

Size effect in uniaxial compression

As was mentioned before, several experiments on prisms with different height were included in the experimental scheme. Prisms with three different heights ($H = 50$, 100 and 200 mm), and constant cross-sectional area ($A = 100$ x 100 mm^2) were loaded between the brushes in the vertical axis of the triaxial apparatus. While the specimens were sawn from the same original prisms that were used for making the 100 mm cubes (see Fig. 1.8), only "perpendicular" specimens could be obtained.

In Fig. 1.16, the peak stresses and strains (both $\varepsilon_{1,\text{surf}}$ and $\varepsilon_{1,\text{loa.pl}}$) for specimens with different height are gathered. From the strenght results (squares), it is obvious that in this respect the brushes yield good results: the same strength is measured for all specimens irrespective of the specimen's height. This in contrast to experiments where dry steel platens are used [e.g. Schickert 1980], and for which usually a huge increase of "apparent" strength is measured when the specimens height is decreased. The strain results in the lower part of the figure indicate that the differences between surface and
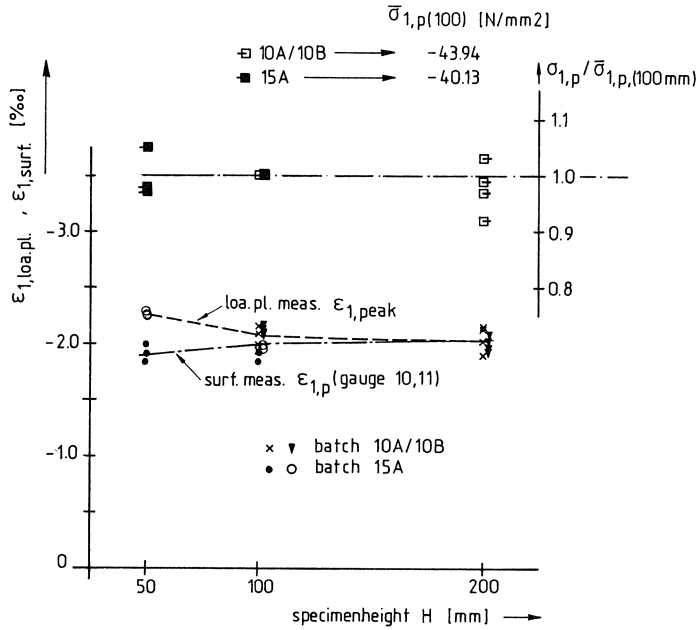
22

Fig. 1.16. Conditions at peak stress level for specimens with different height (H = 50, 100 and 200 mm), and constant cross-sectional area (A = 100 x 100 mm²).

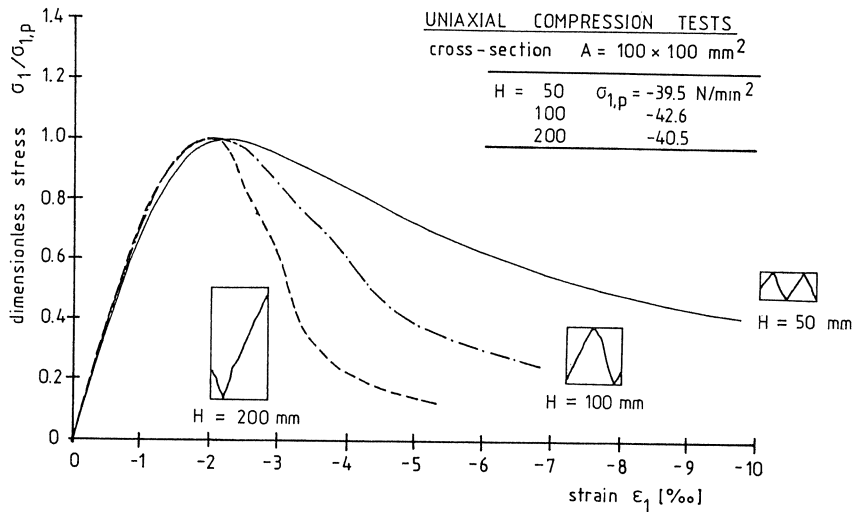Fig. 1.17. Influence of specimenheight on the uniaxial stress-strain curve $(\sigma_1 - \varepsilon_{1,\text{loa.pl.}})$ in compression.

23

loading platen measurement increases when the specimen height decreases. This is obvious: the effect of boundary disturbances increases when the effective length over which they are smeared decreases.

The full implications of decreasing the specimenheight are shown in the next figures. In Fig. 1.17 the axial stress-strain curves for three specimens with different height are plotted. Note that the stress-axis has been made dimensionless with regard to the peak stress measured in each separate experiment. The maximum stress measured in the three tests is given in the same figure. The differences are obvious: in the pre-peak region the stress-strain curve is the same for the three heights investigated, in the descending branch however, the slope of the softening branch decreases when the height of the specimen decreases. Similar results are measured when prisms are loaded in uniaxial compression, reinforced with stirrups, and the distance between the stirrups is varied [Roy & Sozen 1964].

When now the post-peak curves are plotted as stress-displacement curves, as is done in Fig. 1.18, the differences in post-peak behaviour disappear almost completely. In Fig. 1.18, the "post-peak" displacement plotted, has been calculated following $u_{1,tot}-u_{1,\sigma 1p}$, i.e. the total specimen deformation has been decreased by the deformation at peak. The conclusion is evident. A localized deformation is smeared over different specimen heights, leading to the observed decrease of the softening slope (in terms of stress and strain). In fact it is now shown that failure in unaxial compression is similar to the loclized fracture mode observed in uniaxial tension [e.g. Reinhardt 1984, Gopalaratnam & Shah 1985]. Only the location and orientation of the macroscopic fracture planes is different. In uniaxial tension, a localized macroscopic fracture plane develops perpendicular to the tensile direction, in uniaxial compression a shear type fracture plane develops which takes the form of a zig-zag band when the specimen height is decreased (see Fig. 1.17). Consequently, in case of a high specimen a few large rest pieces are
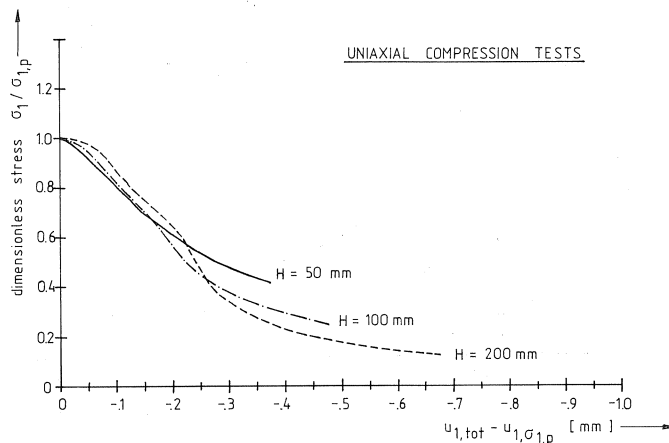

Fig. 1.18. Post-peak stress-displacement diagrams for three specimens with different height, loaded in uniaxial compression.
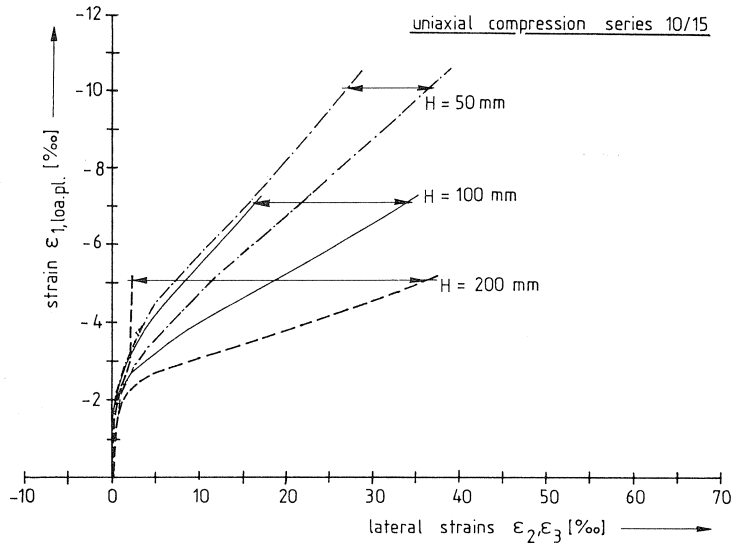
24

Fig. 1.19. Axial strain - lateral strain plots for specimens with different height.

formed, whereas for the smaller prism many small sized rest pieces result after fracture. In the limiting case a horizontal softening branch would be measured (in terms of stress and strain), and the specimen would be separated in infinitely many rest-pieces. In this theoretical case the specimen height would be equal to zero.

The desintegration of the prism with different height into elements of different size is demonstrated with the axial strain - lateral strain plots of Fig. 1.19. For each specimen size, the range of lateral strain readings (ε_2 and ε_3) is indicated in Fig. 1.19. The width of the zone in which lateral strains are recorded (which is indicated with arrows in Fig. 1.19) becomes more narrow when the specimenheight decreases. In fact the desintegration of the prisms in rather large rest pieces is responsible for the very long range that is measured for the 200 mm specimens. In this case a measuring device may accidentally be situated on a larger rest piece, thus registrating unloading. For the smaller sized specimens ($H = 50$, 100 mm), this is simply not possible as a result of the large number and smaller size of the rest pieces. Therefore large differences in lateral strain readings can not occur.

1.3 Multiaxial experimental results

In this section, the triaxial experimental results are shown. After, the experimental program is reviewed, subsequently the strength results, deformational results, load-displacement diagrams and fracture modes are discussed (section 1.4). Finally, in section 1.5, some limited results of rotation experiments are shown. In view of the results of the uniaxial size-tests, which clearly indicated the localized nature of fracture in uniaxial compression, in the following sections all results are plotted as stress-displacement diagrams. This representation is considered more objective.

1.3.1 Experimental design

In the main triaxial testing program, the number of parameters that was varied was restricted to four.

First, attention was given to the influence of the loading path in the σ_1–σ_2 plane. Loading was applied by either following a constant stress-ratio path ($\sigma_2/\sigma_1 = \alpha$, with $\alpha = -0.2$, 0.0, 0.1 and 0.33), or by following a constant displacement-ratio path ($u_2'/u_1' = \alpha$, with $\alpha = -0.2$, 0.0, 0.1 and 0.33). Note that the displacements u_i' are the total displacements of the specimen-brush system that is included in the measuring length covered by the LVDTs (see Fig. 1.4). As will be shown, a non-linear stress-path was applied to a specimen by following such a constant displacement-ratio path.

The second parameter is the confinement in the third principal direction, σ_3. The third principal stress was chosen proportional to the major compressive stress at test initiation: $\sigma_3 = \beta \sigma_1$, with $\beta = 0.05$ or 0.10. Consequently, σ_3 always was compressive. The level of β was restricted to 0.10, while the lay-out of the brushes allowed for specimen deformations up to 3 mm only. As will be shown, the restriction was already quite noticeable in the experiments at the higher confinement level ($\beta = 0.10$), and the softening branch could not be followed to the residual stress-level in some cases.

The third parameter to be studied was the influence of the orientation of the initial damage field with respect to the applied triaxial loading. From the preliminary uniaxial experiments, already a considerable influence of initial anisotropy on the overall stress-displacement response of a specimen was measured. It was considered favourable to vary this parameter, as it might yield some information about the influence of micro-cracking on the macroscopic stress-displacement response under triaxial loading. The variations of this parameter are shown in Fig. 1.20.

Finally, loading was applied to a specimen either monotonically or with load cycles to

a) parallel loading
  - triaxial compression
    $$\sigma_1 < \sigma_2 < \sigma_3 < 0$$
  - tension-biaxial compression
    $$\sigma_1 < \sigma_3 < 0 < \sigma_2$$

b) perpendicular loading
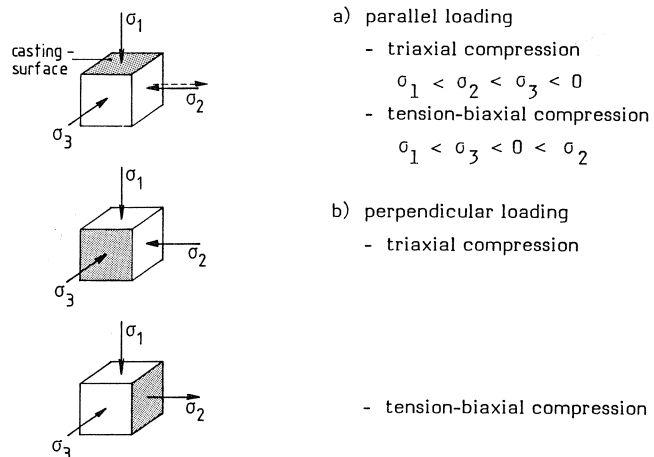 - triaxial compression

  - tension-biaxial compression

Fig. 1.20. Orientation of the initial damage field with respect to the applied external stress combination.
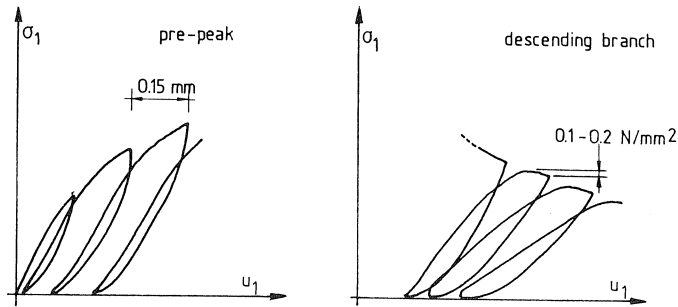
Fig. 1.21. Criteria for load reversal in the triaxial experiments with load cycles to the envelope curve.

the envelope curve. Main reason for carrying out these cyclic experiments is that they might give some more information on damage sustained to a specimen (for example by using the compliance variations as a measure for the amount of cracking). Such information can not be subtracted from monotonic experiments. Yet, several monotonic tests were carried out as well in order to investigate if any influence of load cycling on the overall stress-displacement behaviour occured.

In the cyclic triaxial compression tests as well as in the cyclic tension - biaxial compression displacement-ratio experiments, the major compressive direction was used for defining the unloading and reloading criteria. In Fig. 1.21 the adopted criteria for load reversal, both in the pre-peak and the post-peak region are shown. In the tension - biaxial compression stress-ratio experiments, the tensile stress-displacement curve was guiding. No load cycles were carried out in the pre-peak region in these experiments. When each combination of parameters should be tested only once, a total of 64 triaxial experiments would be required. Instead, only half of the scheme was carried out, as shown in Table 1.3. The experimental design was made using the theory of linear models [Cochran and Cox, 1957], and the experimental scheme is a half replicate of a 2.4^2 factorial in four blocks (i.e. 4 factors at two levels each, and 1 factor at 4 levels). It should be mentioned that the specimens for the triaxial series were obtained from four batches (viz. 8A, 8B, 9A and 9B). Differences between batches could be estimated from the block effect.

As can be seen from Table 1.3, the cubes originating from the prism-end (no. 1 and 6), were omitted from the triaxial experimental design. From the preliminary uniaxial experiments it was found that these "end-cubes" had a significant larger strength than the "middle-cubes". Also in the preliminary biaxial experiments an increase of strength was observed towards the prism ends, and it was expected that the effect would become even more prominent in the triaxial tests.

Therefore, it was considered expedient to rule out the effects of the specimen positions, by simply omitting the cubes originating from the prism ends. In spite of the expected over-estimation of strength, it was considered useful to use these "end-cubes" for determining the uniaxial response of the concrete, both in tension and compression. Thus

27

Table 1.3. Triaxial Experimental Design

			$\sigma_3/\sigma_1 =$			
			$-0.05/-1.0$		$-0.10/-1.0$	
			perp.	para.	perp.	para.
$\sigma_2/\sigma_1 =$ +0.2 /−1.0		M		8A1-4	9A1-5	
		C	8B1-5			9B1-4
	0.0 /−1.0	M	9A1-3			8A2-2
		C		9B1-3	8B1-4	
	−0.1 /−1.0	M		9A2-4	8A2-5	
		C	9B1-2			8B1-2
	−0.33/−1.0	M	8A1-3			9A2-5
		C		8B2-4	9B1-5	
$u_2'/u_2' =$ +0.2 /−1.0		M	9B2-5			8B2-2
		C		9A1-4	8A2-3	
	0.0 /−1.0	M		8B2-5	9B2-4	
		C	8A2-4			9A2-3
	−0.1 /−1.0	M	8B1-3			9B2-3
		C		8A1-2	9A2-2	
	−0.33/−1.0	M		9B2-2	8B2-3	
		C	9A1-2			8A1-5

M = monotonic loading
C = cyclic loading (load cycles to the envelope curve)

para. = parallel loading (Fig. 1.20)
perp. = perpendicular loading (Fig. 1.20)

9A2-4
⊤│ └ position
│ prism no. 2
batch

the total number of experiments was extended to 48, including 8 uniaxial compressive and 8 uniaxial tensile experiments. All the uniaxial tests were loaded parallel (see Fig. 1.20). The displacement rate in the triaxial experiments was 2 μm/s in the major compressive direction.

1.3.2 Strength results

The triaxial experimental design, as presented in the previous section, included several displacement-ratio experiments (see Table 1.3). The response of such experiments in "stress-space" is non-linear as shown by the example in Fig. 1.22. In this figure the stress-path $\sigma_1 - \sigma_2$ is shown for a biaxial experiment loaded in displacement-ratio $u_1'/\ u_2' = -1.0/-0.33$. (this particular specimen (5B2-3) was part of the preliminary biaxial test series, see Table 1.2).

At this place a clear distinction between the control parameters u_i', and the specimen deformations u_i should be made. The total displacements of the brush-specimen system
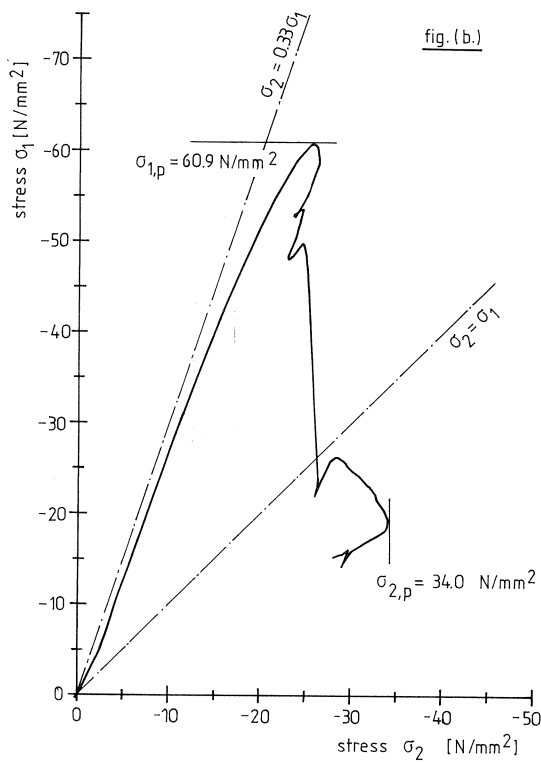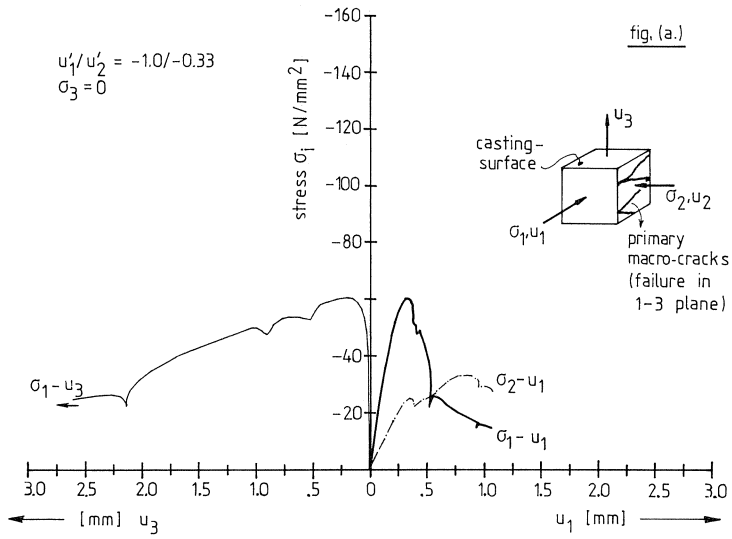
Fig. 1.22. Example of a biaxial constant displacement-ratio experiment (5B2-3, $u'_1/u'_2 = -1.0/$ -0.33, $\sigma_3 = 0$), stress-displacement curves (fig. a.), and stress-path $\sigma_1 - \sigma_2$ (fig. b.).

(see Fig. 1.4), were used for test-control. Consequently, as already mentioned in section 1.1, the measured displacements u_i' had to be corrected for the brush deformations. The calibration of the brush deformations was carried out very carefully [see Van Mier 1984b]. Always a displacement-ratio experiment is defined by the ratio between the total displacements (u_1' and u_2'). Consequently, the specimen deformations are not according this ratio, but will deviate from it depending on the level of external loading. However these deviations are small compared to the total deformations.

The initial slope of the $\sigma_1 - \sigma_2$ curve is fully determined by the "elastic properties" of the material and the applied displacement ratio (in the triaxial experiments also the confinement in the third principal direction σ_3 is important). Due to microcracking, an increasing curvature of the stress-path is measured, until a limit-point (σ_{1p}) is reached, and when the experiment is carried out in displacement control a stable softening branch is measured. As can be seen from Fig. 1.22.a, in this experiment still some instabilities occured in the descending branch, yet in the triaxial experiments, the stability was improved considerably as be will shown in the subsequent sections. It should be mentioned that in general, in biaxial experiments which fail in the third (unstressed) direction, failure was rather explosive which implies that the descending branch is rather unstable.

When the experiment proceeds in the softening branch, σ_1 decreases considerably. The stress in the second (actively) deformed direction (σ_2), starts to increase when the residual stress-level in the major compressive direction (σ_1) is reached. The changes are
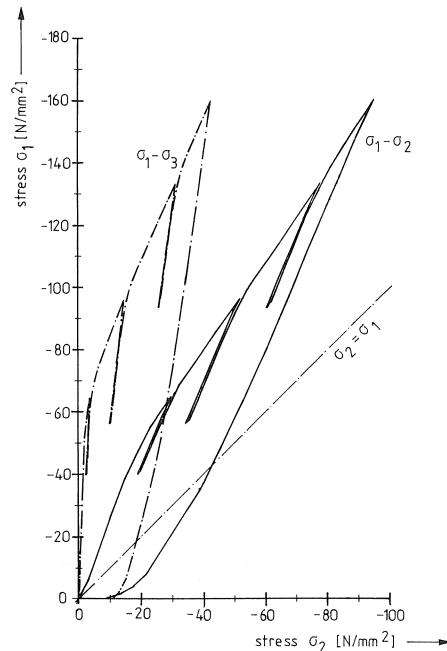

Fig. 1.23. Example of a triaxial constant displacement-ratio experiment (pilot test 4B2-3, $u'_1/u'_2/u'_3 = -1.0/-0.33/0$).

dramatic, and eventually, σ_2 grows larger than σ_1: a gradual rotation of principal stesses takes place (see section 1.5). Subsequently, a second limit point is measured in the σ_2-direction, whereafter again a stable softening branch develops. The maximum stress-level in the σ_2-direction is considerably lower than the first limit point in the σ_1-direction. This is obvious, because σ_2 is applied to a highly damaged specimen, and the reason that still a stress-level of approximately $-35\,\text{N/mm}^2$ is atainable can be explained from the directions of the fracture planes which develop in the first "softening branch" (see inset in Fig. 1.22). Failure modes are discussed in detail in section 1.4.

In the previous example only two directions were kept under displacement control, and free displacements were possible in the third (unstressed) direction. Things become more complicated when the displacement is controlled in all three directions. The result of a triaxial displacement-ratio experiment $(u_1'/u_2'/u_3' = -1.0/-0.33/0.0)$ is shown in Fig. 1.23. This result was obtained from one of the pilot tests, which preceded the triaxial series. In this particular pilot test no epoxy capping between the loading platen and the specimen was applied, which means that some initial settings may influence the stress-ratio in the "linear-elastic" stage. In this experiment, all three stresses were compressive, and no "stress failure point" was reached. In fact under these conditions never such a failure (in terms of stresses) can be found. Eventually, the stress-path may reach the strength failure envelope, but will then, likely after some re-distributions, proceed into the high triaxial compression region. The stress-paths in Fig. 1.23 become almost linear after a first bend at a level of $\sigma_1 \approx -70\,\text{N/mm}^2$. The first bend is likely associated with significant microcracking in the specimen.

Failure envelopes

In Fig. 1.24, the strength results of both the preliminary biaxial experiments and of the triaxial tests are shown. All results have been plotted on the plane $\sigma_3 = 0$, which implies that for the triaxial experiments the projection of planes $\sigma_3 = \beta\,\sigma_1$, with $\beta = 0.05$ and 0.10 on the plane $\sigma_3 = 0$ are shown. Each data point in Fig. 1.24 is the result of a single experiment. For a stress-ratio experiment, the peak stress is reached in all three (or two) directions simultaneously, and this limit state has been plotted. As shown in the previous section, a highly non-linear stress-path is measured in the displacement-ratio experiments. Several limit-points, in different directions, may occur in such experiments, but in Fig. 1.24, only the first limit point (i.e. the stress combination when σ_{1p} is reached) is indicated. An exception is made for the triaxial tensile-compressive dis-placement-ratio experiments, for which both the first limit point (which is tensile and occurs in σ_2-direction), and the second (compressive) limit point in the σ_1-direction, are shown.

The strength results obtained from the 8 additional uniaxial compressive and uniaxial tensile experiments are gathered in Table 1.4. The stress-displacement response of se-veral of the uniaxial compression and uniaxial tension tests are included in the appen-dix. The dashed contours in Fig. 1.24 are computed with the recently published failure criterion of Podgorski [1985]. The values of the five parameters which must be specified
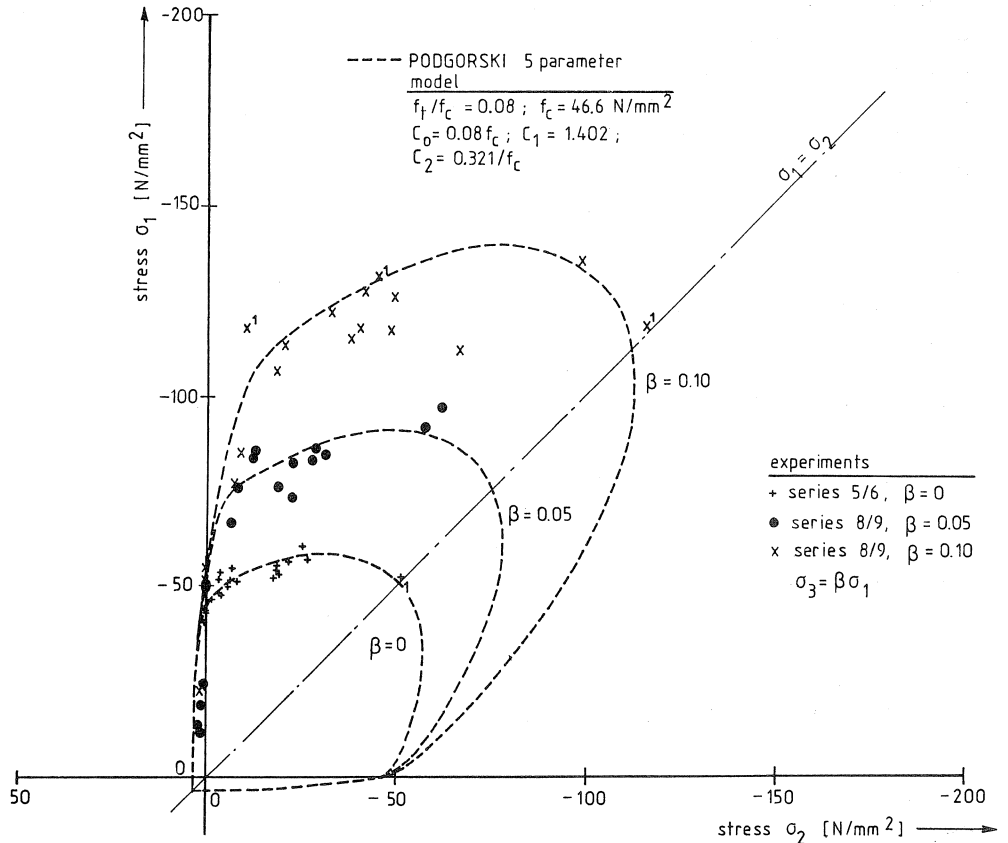
Fig. 1.24. Strength results of the preliminary biaxial experiments (series 5A/5B/6A) and the triaxial experiments (series 8A/8B/9A/9B). The results are compared with the recent failure criterion of Podgorski.

for this model are indicated in Fig. 1.24 as well. The uniaxial compressive strength f_c has been derived from the values in Table 1.4. In fact, the average compressive strength of batches 8A through 9B has been used. Note that the experiments marked with (1) in Fig. 1.24, are the results of some succesful pilot tests, which preceded the triaxial series.

The agreement between the Podgorski model and the experimental results is satisfac-

Table 1.4. Uniaxial strength results (in $[N/mm^2]$) obtained from 100 mm cubes loaded between brushes (the numbers between brackets indicate the number of successful experiments).

batch	f_c	f_t
8A/8B	45.3 (4)	2.8 (3)
9A/9B	47.9 (4)	3.1 (4)

tory, especially in the compressive region. Note that the contours $\sigma_3 = \beta\sigma_1$ are non-symmetric, and intersect with the $\sigma_1 = \sigma_2$ diagonal non-orthogonal. This is a direct result of intersecting the three dimensional failure envelope with tilted planes ($\sigma_3 = \beta\sigma_1$), see Van Mier & De Borst [1986]. Thus, a direct consequence of the decision of carrying out proportional load path experiments is that all combinations σ_1/σ_2 must be investigated for determining the shape of the failure envelope in stress-space.

In Fig. 1.25, the biaxial experimental results are shown somewhat enlarged, and are compared with results obtained by Kupfer [1973], Liu et al. [1972], and Gerstle et al. [1978]. The agreement is good, and this may give some confidence in the adopted experimental technique. One remark should be made. The experiments marked with (1) in Fig. 1.25, are the results obtained from experiments on "end-cubes" (no. 1 and 6 in Fig. 1.8). It can easily be seen that the strength of these specimens was generally larger than the specimens originating from the middle part of the "casting prisms". The effect, which was statistically significant, was also observed in the uniaxial compression tests [see Van Mier 1984b].
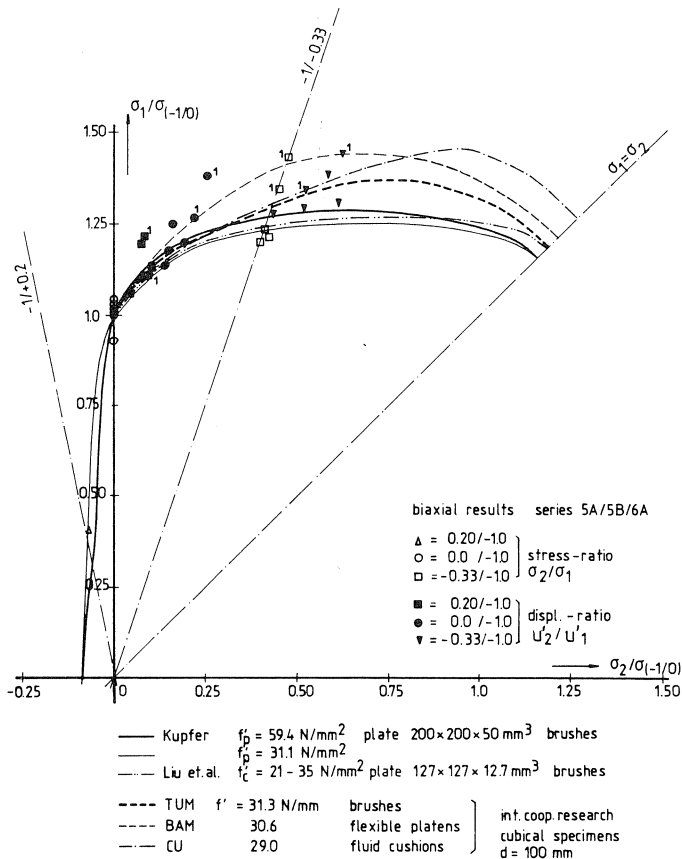

Fig. 1.25.   Comparison of biaxial strength results with previous investigations.
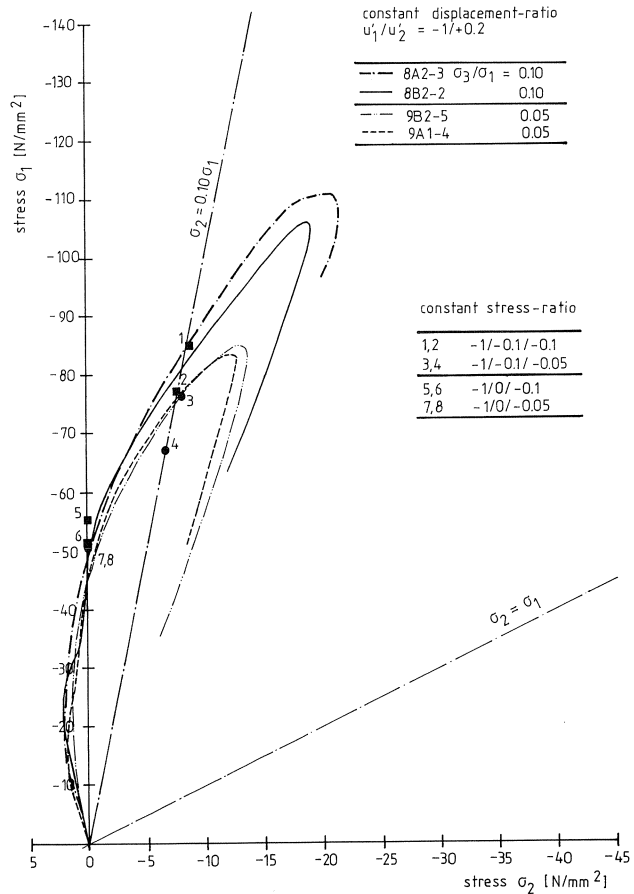
Fig. 1.26. Stress-paths $\sigma_1 - \sigma_2$ for the tensile-compressive constant displacement-ratio experiments.

The strength results of the triaxial series were analyzed statistically as well. From this analysis, only the main effects due to the intermediate and minor principal stress, and the effects due to a displacement or stress-ratio were found to be significant at the 5% level. These differences are apparent from Fig. 1.24. All other effects were not significant. Yet it should be mentioned that more experiments are needed for deriving at more definite conclusions. The scatter is still rather large, and also the treatment of the displacement ratio experiments was not very satisfactory (only a linear term was available for including this effect in the statistical model).

In Fig. 1.26, the stress-paths $\sigma_1 - \sigma_2$ of four tensile-compressive constant displacement-ratio experiments are shown. Note that the scale of the σ_2-axis is different from the scale of the σ_1-axis. In these experiments, first a tensile peak was reached in the σ_2-direction, whereafter a stable softening branch was measured. Subsequently, when the compressive stress σ_1 increased (and consequently also the "poisson's ratio"), σ_2 became com-

34

pressive and a second limit point was measured in the triaxial compressive region. After this limit point has been exceeded, a stable descending branch was measured in the major compressive direction.

Also plotted in the same figure are the limit points of eight constant stress-ratio experiments (viz. along the axes $\sigma_2 = 0$, and $\sigma_2 = 0.10\sigma_1$). Comparison between these constant stress-ratio experiments, and the stress-paths of the displacement-ratio tests in the compressive region suggests that the failure locus is followed in the latter experiments. It is not certain if the same effect occurs in the tensile-compressive region as well, while not very much tensile-compressive constant stress-ratio experiments were carried out. Future research should solve these questions. However, if indeed the failure contour is followed in such experiments, only a limited number of tests are needed to study the transition from cleavage to shear failure.

1.3.3   Displacement-paths

Before discussing the stress-displacement behaviour of concrete under multiaxial states of stress, attention is paid to the displacement-paths that were either measured or followed. In a constant displacement-ratio experiment, the situation is rather simple, and the displacement path is a straight line. However, when a constant stress-ratio is applied, the stress-path is a straight line, but the displacement-path becomes highly non-linear. Comparison of the response of both types of experiments, might yield some insight of how stress-space and deformation-space are mapped onto each other.

In Fig. 1.27, two families of displacement-paths are plotted. In Fig 1.27.a, the results are shown of eight biaxial constant displacement-ratio experiments ($u_2'/u_1' = \alpha$), with a variable confinement in the third principal direction (i.e. $\sigma_3/\sigma_1 = \beta$), and in Fig. 1.27.b, the displacement-paths of six triaxial constant stress-ratio experiments are shown ($\sigma_1/\sigma_2/\sigma_3 = -1.0/\alpha/\beta$).

Each experiment is characterized by two displacement paths: $u_1 - u_2$ and $u_1 - u_3$. The two paths, belonging to the same experiment are marked similarly: the same line type and marking letter are used. For example in Fig. 1.27.a, the experiment marked with a dash-dotted line, and the letter "e" is a constant displacement-ratio experiment $u_2'/u_1' = 0.10$, with $\sigma_3/\sigma_1 = 0.05$.

The applied displacement-ratio's are recognized from the almost straight lines in Fig. 1.27.a. The deviations between the displacement-ratio which is actually applied to the specimen (u_2/u_1), and the total displacement-ratio (u_2'/u_1'), can easily be seen from the so-called "plane-strain" tests ($u_2' = 0$). Obviously, the deviations become larger when a higher confinement in the third principal direction is applied (compare experiments "c" and "d" in Fig. 1.27.a). While in the third principal direction the specimen is confined by a constant stress-ratio ($\sigma_3/\sigma_1 = \beta$), a non-linear displacement-path u_3/u_1 is measured. The results fall for both confinement levels ($\beta = 0.05$ and 0.10) in relatively narrow bands (experiments "a", "c", "e" and "g" are at the lower confinement level $\beta = 0.05$, experiments "b", "d", "f" and "h" are at the higher confinement level with $\beta = 0.10$). It should be mentioned that all experiments shown in Fig. 1.27 were loaded parallel with
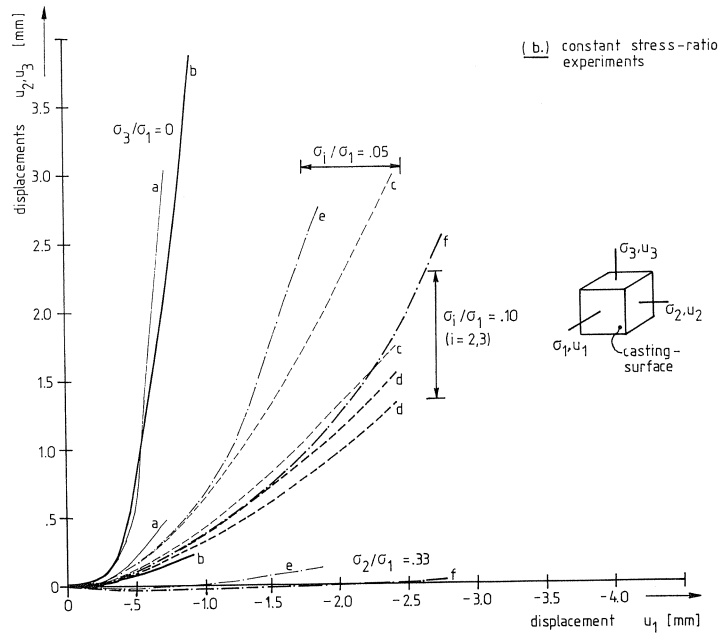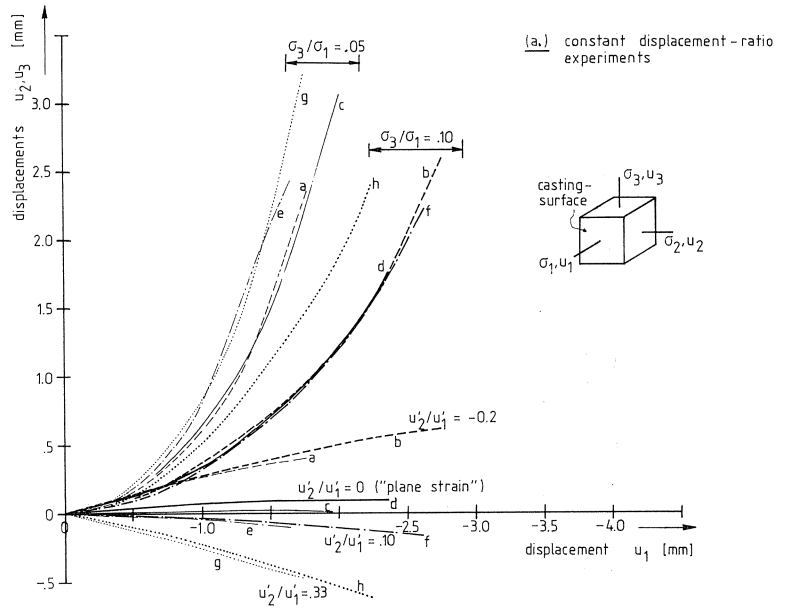
Fig. 1.27. Displacement-paths for eight biaxial constant displacement-ratio experiments with a variable confinement in the third principal direction (fig. a.), and for six triaxial constant stress-ratio experiments (fig. b.).

36

regard to the direction of casting. In general a somewhat larger scatter was measured when the specimens were loaded perpendicularly to the direction of casting, which is in agreement with the uniaxial experiments (see Fig. 1.9).

From Fig. 1.27.a it can be concluded that the deformational behaviour in the third principal direction (σ_3, u_3), is independent of the applied displacement-ratio. The effect of increasing the confinement is that larger deformations can be sustained by the specimen. The implications for the stresses that can be carried in a certain direction after the specimen has undergone deformations in the order of 2–3 mm will be shown in the next section.

The results shown in Fig. 1.27.b for the six constant stress-ratio experiments can be interpreted in a similar manner. In this case however, as expected, all displacement-paths are highly non-linear. Furthermore, when a stress-ratio increases, for example from $\alpha = 0$ *to* $\alpha = 0.33$, the displacement-paths become gradually less steep. In fact we see that the rate at which tensile deformations can occur is reduced considerably when the confining stress is increased. When $\alpha = 0.33$, the displacements u_2 are close to zero, and the displacement-paths fall almost along the u_1-axis. In fact, these experiments are almost similar with regard to deformational and strength response to the so-called "plane-strain" tests. This can be seen from Table 1.5, where the conditions at "peak stress" are given for the four "plane-strain" experiments (with $u_2 = 0$), and for the four constant stress-ratio experiments $\sigma_1/\sigma_2/\sigma_3 = -1.0/-0.33/\beta$, with $\beta = 0.05$ and 0.10.

Table 1.5. Peak-stresses $\sigma_{i,p}$ (in [N/mm^2]), and displacements u_i (in [mm]) for displacement-ratio tests $u'_1/u'_2 = -1.0/0.0$, and stress-ratio experiments $\sigma_1/\sigma_2 = -1.0/-0.33$.

specimen	σ_3/σ_1	ld	σ_{1p}	σ_{2p}	σ_{3p}	u_1	u_2	u_3
$u'_1/u'_2 = -1.0/0.0$								
8A2-4	0.05	perp.	-76.27	-18.96	-4.15	-0.73	0.04	0.57
8B2-5	0.05	para.	-82.16	-22.70	-4.51	-1.21	0.05	0.92
9B2-4	0.10	perp.	-121.12	-33.13	-12.15	-1.60	0.08	1.04
9A2-3	0.10	para.	-117.59	-40.81	-12.13	-2.11	0.10	1.36
$\sigma_1/\sigma_2 = -1.0/-0.33$								
8A1-3	0.05	perp.	-82.91	-27.95	-4.61	-0.69	-0.06	0.52
8B2-4	0.05	para.	-85.59	-28.67	-4.62	-1.03	0.01	0.69
9B1-5	0.10	perp.	-115.02	-38.41	-11.68	-1.54	-0.01	1.07
9A2-5	0.10	para.	-127.00	-42.02	-13.30	-2.12	0.00	1.39

ld   = loading direction
perp. = perpendicular (see Fig. 1.20)
para. = parallel (see Fig. 1.20)

Displacement contours

Similar as for the strength results, the deformational results can be presented as contours in deformation space. In this case, however, the results can not be compared with data obtained by other investigators. In the past, in general "load-controlled"

37

multiaxial tests were performed [see for example the results obtained in the cooperative international research, Gerstle etal. 1978, 1980], and displacement-controlled tests were carried out along the compressive meridian only [using cylindrical specimens, see for example the experiments carried out by Jamet, etal. 1984]. In general it is difficult to estimate the peak deformations in load-controlled experiments, as failure is very explosive. Only an exception should be made for experiments carried out at high confinement levels when the slope of the descending branch decreases, and often the machine stiffness is sufficient for measuring (at least a) part of the softening branch. Unfortunately, the experimental results obtained in the current investigation are restricted to a small segment in deformation space. This is shown in Fig. 1.28, where the displacement u_1 and u_2 measured at "peak stress" are plotted for all triaxial experiments, as well as for some pilot-tests (which are marked with "1"). The results are shown in four groups: perpendicular loaded and parallel loaded specimens at both confinement levels $\beta = 0.05$ and $\beta = 0.10$. The displacement-ratio experiments can be distinguished from the stress-ratio experiments. In the first case, two displacement-ratio experiments, loaded under similar conditions, but with different orientations with respect to the initial damage field are connected with a dashed line. For example experiments marked with "A" and "B" are displacement-ratio experiments $u_1'/u_2' = -1.0/ -0.33$, carried out at the higher confinement level $\beta = 0.10$. Now easily, the deviations
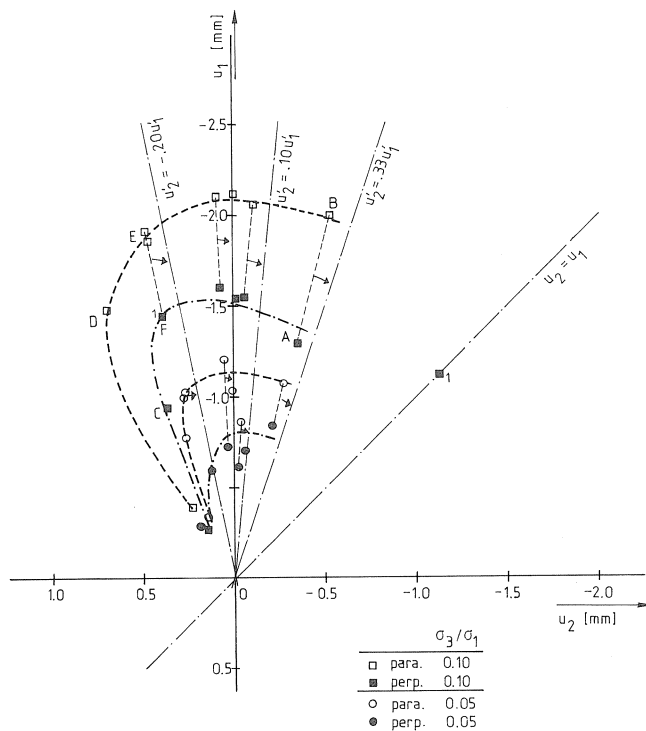

Fig. 1.28.   Displacement-contours for the triaxial experiments.

38

between the applied displacement-ratio (u_2'/u_1^-) and the actually occuring (specimen) displacement-ratio (u_2/u_1) can be seen. A small arrow indicates (for the pairs of displacement-ratio experiments), along which radial the specimen-brush system was loaded.

Pairs of stress-ratio experiments (for example the experiments "C" and "D" loaded along the path $-1.0/-1.0/-1.0$) are not connected by dashes lines. In general the peak deformations of tests carried out under similar loading ratio's, are situated along the same radial. For example, the peak displacements of all stress-ratio experiments $\sigma_1/\sigma_2 = -1.0/-0.33$, are situated along a radial which coincides almost with the u_1- axis.

Specimens belonging to the same group have been connected with a contour. The differences due to confinement are obvious. An enormous increase of peak-deformations is measured when the confinement level is increased by 5%. In fact the peak-deformations are almost doubled (compare for example the results of the parallel loaded specimens, at both confinement levels (dashed contours)).

The differences in response by simply changing the orientation of the initial damage field is also remarkable. Especially at the higher confinement level ($\beta = 0.10$), a 50% increase of peak deformations is measured in some of the experiments. As was already shown in figure 1.20, slight differences in orientation with respect to the initial damage field occured for the tension - biaxial compression experiments. The implication of these differences can be seen from figure 1.28. Displacement-ratio experiments $u_1'/u_2' = -1.0/+0.2$ (for example the two experiments marked "E" and the open squares) do not show the large differences due to initial anisotropy, which can be explained from the slight differences in orientation of the initial damage field [see also Van Mier 1985]. This is the reason for marking both tests with an open square, which corresponds to parallel loading. For this particular loading path however, also a pilot test was carried out (i.e. the experiment marked "F"), which was loaded perpendicularly. By comparing the results of experiments "E" and "F", the same difference in response due to initial anisotropy is observed.

Note that from the statistical analysis of the triaxial strength results no significant influence of the initial orientation of a specimen was found. Yet, although no statistical analysis was carried out for the deformational results, it may be concluded that, for the concrete tested, a considerable influence of initial anisotropy occured.

More experiments must be carried out in order to determine the complete shape of the displacement contours. Yet by comparing figures 1.24 and 1.28 it is obvious that the mapping between stress-space and deformation-space is very complex, especially when factors such as initial anisotropy become important.

1.3.4 Multiaxial stress-displacement behaviour

In this section some examples of multiaxial stress-displacement behaviour are discussed. Results of cyclic experiments, with load cycles to the envelope curve, are presented

by their envelopes only. For results of the cyclic experiments, the reader is refered to previous publications [Van Mier 1984b, 1986b].

Influence of minor principal stress

In Fig. 1.29, three stress-displacement curves are shown for experiments carried out under "plane-strain" conditions ($u_2' = 0$). The confinement in the minor principal direction $\sigma_3 = \beta\sigma_1$, was varied: $\beta = 0.0$, 0.05 and 0.10. In the upper part of the figure, displacements u_1 and u_3 are plotted against the major compressive stress σ_1, in the lower part of the figure σ_2 is plotted against u_1. All three experiments were loaded pendicular to the direction of casting. Note that one of the experiments was part of the preliminary biaxial series (viz. 5A1-3).

As was already shown in Fig. 1.24 and 1.28, an increase of confinement results in an increase of peak-stresses and displacements. The differences are quite large, especially in the pre-peak region. In the post-peak region, however, a strikingly similar response is measured. The shape and gradient of the softening branch is the same for the three confinements investigated, only the residual stress-level increases when β increases. The rate of increase of u_3 decreases in the presence of confinement. Up to "peak", an increasing stress σ_2 is measured in the zero-displacement direction. Beyond "peak", σ_2 decreases, which may indicate that failure occurs mainly in the 1–3 plane [see section 1.4].

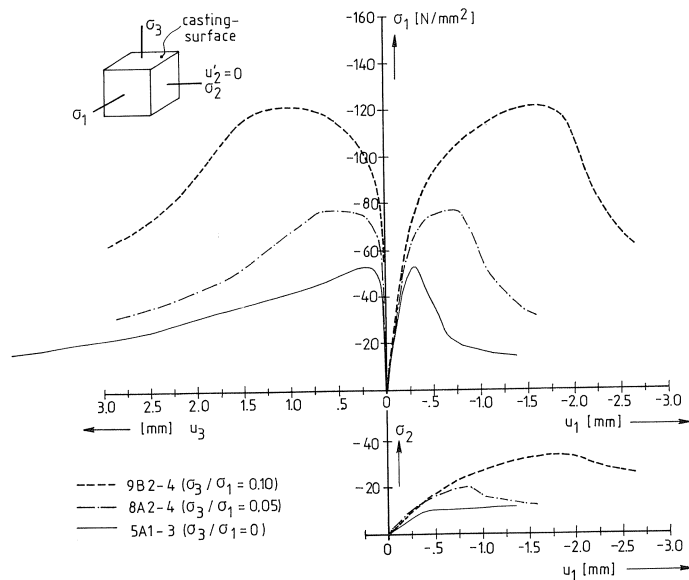

Fig. 1.29. Stress-displacement curves for experiments under "plane-strain" conditions ($u'_2 = 0$), with increasing confinement $\sigma_3 = \beta\sigma_1$.
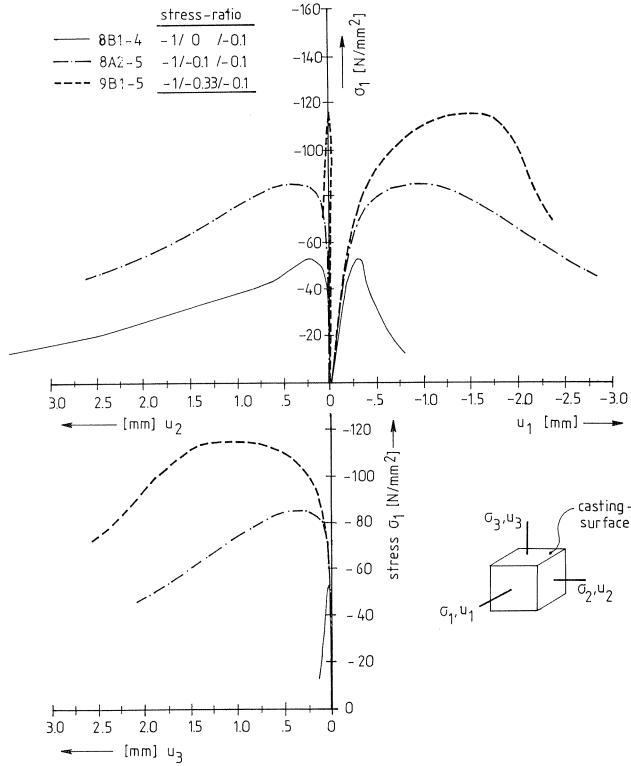
Fig. 1.30. Stress-displacement curves for constant stress-ratio experiments $\sigma_3/\sigma_1 = 0.10$, and $\sigma_2/\sigma_1 = \alpha$, with $\alpha = 0$, 0.10 and 0.33.

Influence of the intermediate principal stress

In Fig. 1.30 the stress-displacement results of three constant stress-ratio experiments are shown. The confinement in the third principal direction was the same for all three experiments, viz. $\sigma_3 = 0.10\sigma_1$. Three intermediate stress-levels were investigated: $\sigma_2/\sigma_1 = \alpha$, with $\alpha = 0.0, 0.10$ and 0.33. All three experiments were loaded perpendicular to the direction of casting. In the upper part of the figure, displacements u_1 and u_2 are plotted against the major compressive stress σ_1, in the lower part the three $\sigma_1 - u_3$ curves are shown. Again, in view of the results presented in Fig. 1.24 and 1.28), the pre-peak behaviour is as expected, yet the differences in post-peak response are striking. Where the experiments $-1/0$ and $-1.0/-0.33$ both display a very steep descending branch, the softening branch of the experiment $-1/-0.1$ has a rather small gradient. This type of behaviour was observed in all experiments leading to two large (not necessarily equal) tensile deformations. In this type of experiments a stress failure point close to the compressive meridian in strength space is found.

When the stress-displacement diagrams of specimen 9B2-4 (see Fig. 1.29) are compared with those of specimen 9B1-5 (see Fig. 1.30), an almost similar behaviour is observed.

41

The similarity between so-called "plane-strain" tests and the constant stress-ratio tests $-1/-0.33/-\beta$ was discussed before (see Table 1.5), but now the complete stress-displacement response of both experiments can be compared. In fact the strength and deformational response of concrete specimens either subjected to a constant displacement-ratio or a constant stress-ratio is not very different. Only in a displacement-ratio experiment more than one limit-point can be measured (see section 1.3.2).

The above results are not consistent with observations by Buyukozturk & Zisman [1982], who reported an increase of strength in displacement confined biaxial experiments in favour of normal proportional biaxial experiments. However, Buyukozturk & Zisman compared their own results with experiments carried out by Kupfer [1973], which were carried out in a different experimental context. As known, from the extensive international cooperative research by Gerstle etal. [1978, 1980], one should be careful in comparing results obtained with different experimental techniques.

Initial anisotropy

One of the parameters investigated was the influence of the orientation of the applied loading combination with regard to the direction of casting of the specimen. Due to shrinkage, differential temperatures and segregation during hardening of the concrete, microcracks and weaker matrix material zones may develop preferentially under the larger aggregates, and as observed in the uniaxial preliminary experiments may have considerable influence on the deformational response of the specimens (see Fig. 1.9). In Fig. 1.31, the influence of initial anisotropy on the multiaxial stress-displacement behaviour is shown for four constant stress-ratio experiments ($\sigma_2/\sigma_1 = 0.33$, and $\sigma_3/\sigma_1 = \beta$, with $\beta = 0.05$ and 0.10). The differences are similar as reported for the uni-
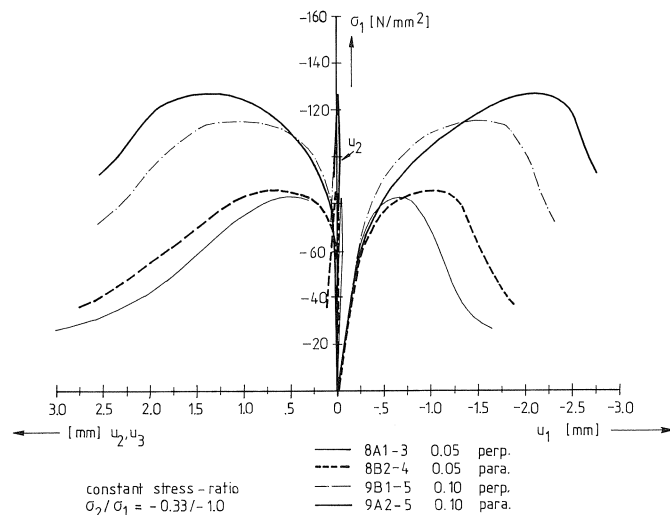

Fig. 1.31. Influence of initial anisotropy on the stress-displacement behaviour for constant stress-ratio experiments $-1/-0.33/\beta$.

42

axial compressive case in section 1.2. The pre-peak stress-displacement behaviour is largely affected, whereas the post-peak response seems to be undisturbed by changing the specimen's orientation with respect to the applied loading combination. The "peak deformations" increase considerably when a specimen is loaded parallel, whereas the carrying capacity is almost the same for the two orientations investigated. Note that the displacements u_2 in the intermediate stressed direction are almost equal to zero in these particular experiments.

"Plane-stress" versus "plane-strain"

In Fig. 1.32 the stress-displacement curves measured in the four "plane-stress" tests (i.e. biaxial compression, $(\sigma_2/\sigma_1 = 0.0$, and $\sigma_3/\sigma_1 = \beta)$ and the four "plane-strain" experiments (i.e. $u_2'/u_1' = 0.0$, and $(\sigma_3/\sigma_1 = \beta)$ are shown. The experiments at the lower confinement level $(\beta = 0.05)$ are compared in Fig. 1.32.a and b, those carried out the higher
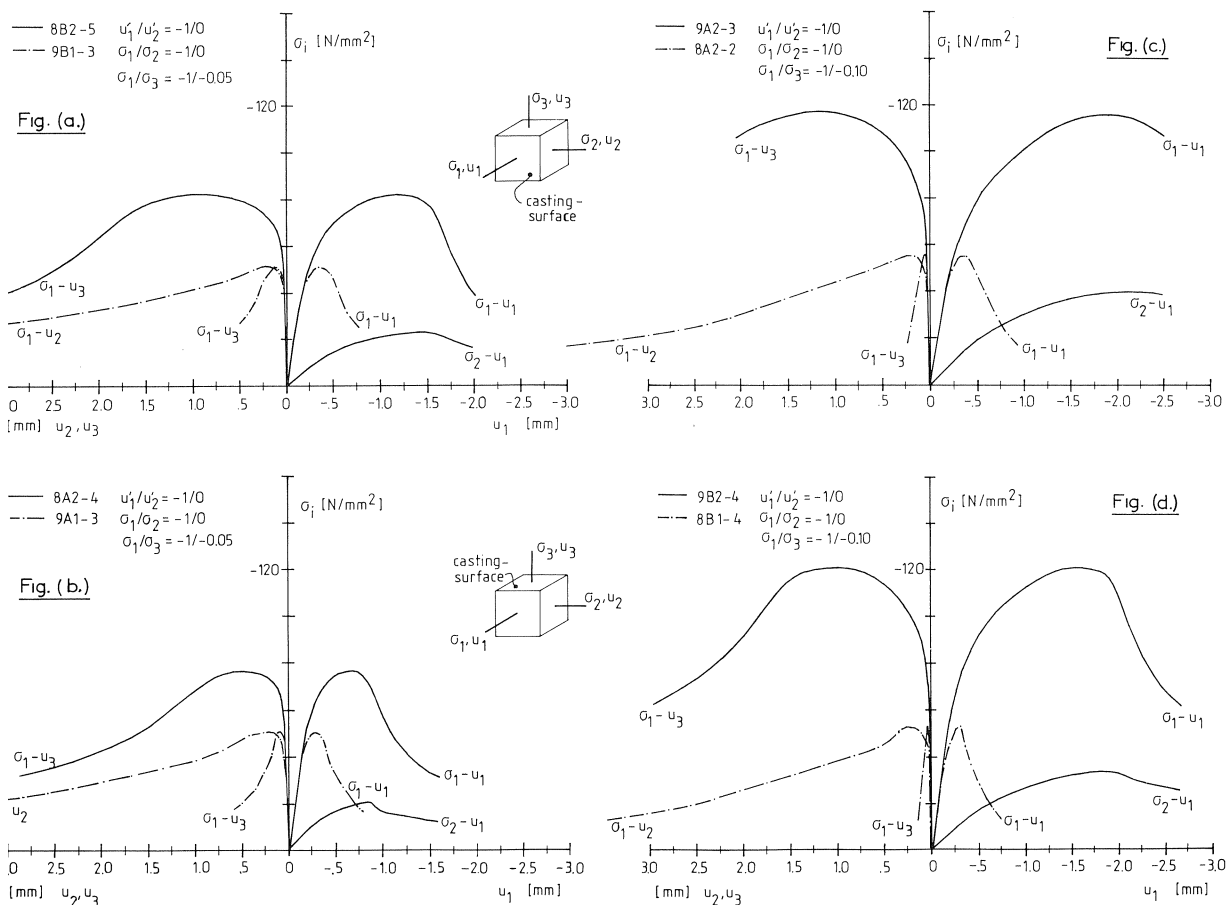

Fig. 1.32. Comparison between "plane-stress" and "plane-strain" experiments.

43

confinement level ($\beta = 0.05$) are shown in figures c and d. Furthermore, the experiments that were loaded parallel to the direction of casting (see Fig. 1.20) are gathered in Fig. 1.32.a and c, the experiments that were loaded perpendicularly are shown in Fig. 1.32.b and d.

Very clear is the enormous difference in strength, especially in the experiments carried out at the higher confinement level. The results show differently the sharp increase of the strength failure contours by increasing the stress-ratio $\alpha = \sigma_2/\sigma_1$ from 0.0 to approximately 0.33. As was shown in Fig. 1.24, the largest increase of the major compressive stress occurs in this interval (that is when experiments on the same "contours" are compared). The pre-peak stress-displacement response is affected most by changing the loading conditions from "plane-stress" to "plane-strain", the post-peak behaviour seems to be indentical in all four combinations. This implies, as will be shown in the following section that macroscopic failure is similar for these experiments. Both types of experiments fail in the direction of the minor compressive stress. In the "plane-stress" experiments this is the σ_2-direction, and in the "plane-strain" tests the σ_3-direction. Again as shown before in Fig. 1.29, the rate at which tensile deformations develop in the direction of the minor compressive direction depends very much on the level of confinement (compare the $\sigma_1 - u_2$ curves for the "plane-stress" experiments with the $\sigma_1 - u_3$ curves for the "plane-strain" experiments).

Both types of experiments are simplifications of triaxial loading cases. The fact that in one of the principal directions either a "stress-component" or a "strain-component" is kept
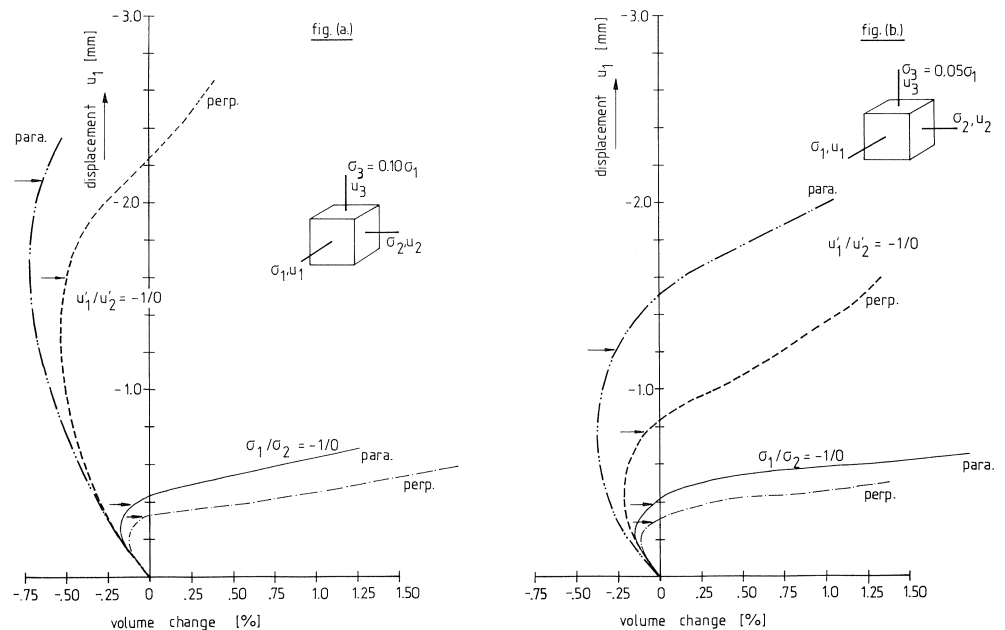

Fig. 1.33. Volume change in "plane-stress" and "plane-strain" experiments (the arrows indicate where a limit point is measured in the major compressive direction).

44

zero, is considered as a welcome simplification. However, the results shown in Fig. 1.32, indicate that complex triaxial effects also occur in such experiments. Due to the heterogeneity of the material local tensile stress-concentrations lead to cracking in the material and non-linear effects are observed.

In Fig. 1.33, the volume changes $(\Delta V/V)$ observed in both the "plane-stress" experiments and the "plane-strain" experiments are shown. The volume change has been plotted against the major compressive displacement u_1, while this was the only continuously increasing "control-parameter" in every experiment. In all triaxial compression tests, after an initial compaction, a considerable dilation was observed. Tensile deformations occur in the biaxial stress-ratio experiments already rather pronounced in the pre-peak region (the displacement-level u_1, at which a stress limit point is measured in the major compressive direction σ_1 is indicated with an arrow for each experiment), but increase at a considerably higher rate in the post-peak region as indicated by the enormous increase of volume $(\Delta V/V)$.

In the "plane-strain" experiments the behaviour is slightly different, especially when the level of confinement increases (σ_3/σ_1). When the confinement increases (compare the "plane-strain" results in figure 1.33.a and b), the rate at which dilation occurs decreases, both before and beyond "peak". The stress limit point shifts gradually towards the minimum-volume point when the confinement increases. Note that the volume change in the "plane-strain" tests $(u_2' = 0)$ is due to increasing (tensile) displacements u_3 and decreasing (compressive) displacements u_1 only.

Also from these figures the differences in behaviour due to initial anisotropy are evident (as discussed in the previous section). Always, when a specimen was loaded parallel, a reduced dilation was measured at comparable levels of compressive displacement u_1. However, beyond peak, the slope of the dilation curves is independent of the specimen's orientation.

1.4 *Fracture*

From the uniaxial compression tests on prisms with variable height (section 1.2), it was concluded that fracture in uniaxial compression is a localized phenomenon, similar to the mechanism observed in uniaxial tension. The formation of a localized shearzone was observed in the triaxial experiments as well. However, in contrast to the uniaxial experiments, where the localized zone was partly hidden due the splitting of the outer concrete layers, the shear-bands could more easily be detected in the multiaxial experiments. The effect of boundary conditions reduces when confinement is present, and the specimen becomes more uniformly stressed [as also known from rock mechanics experiments, see Paterson 1978, Brodsky 1985 and Costin & Stone 1986].

When a cube was removed from the triaxial machine after an experiment was done, it was completely covered by the epoxy-resin capping. An orthogonal "crack-pattern" was imposed to the surfaces of the cube, mainly due to local splitting stresses induced by the separate brush rods. By means of a diamond grinding disk, the outer layers of a
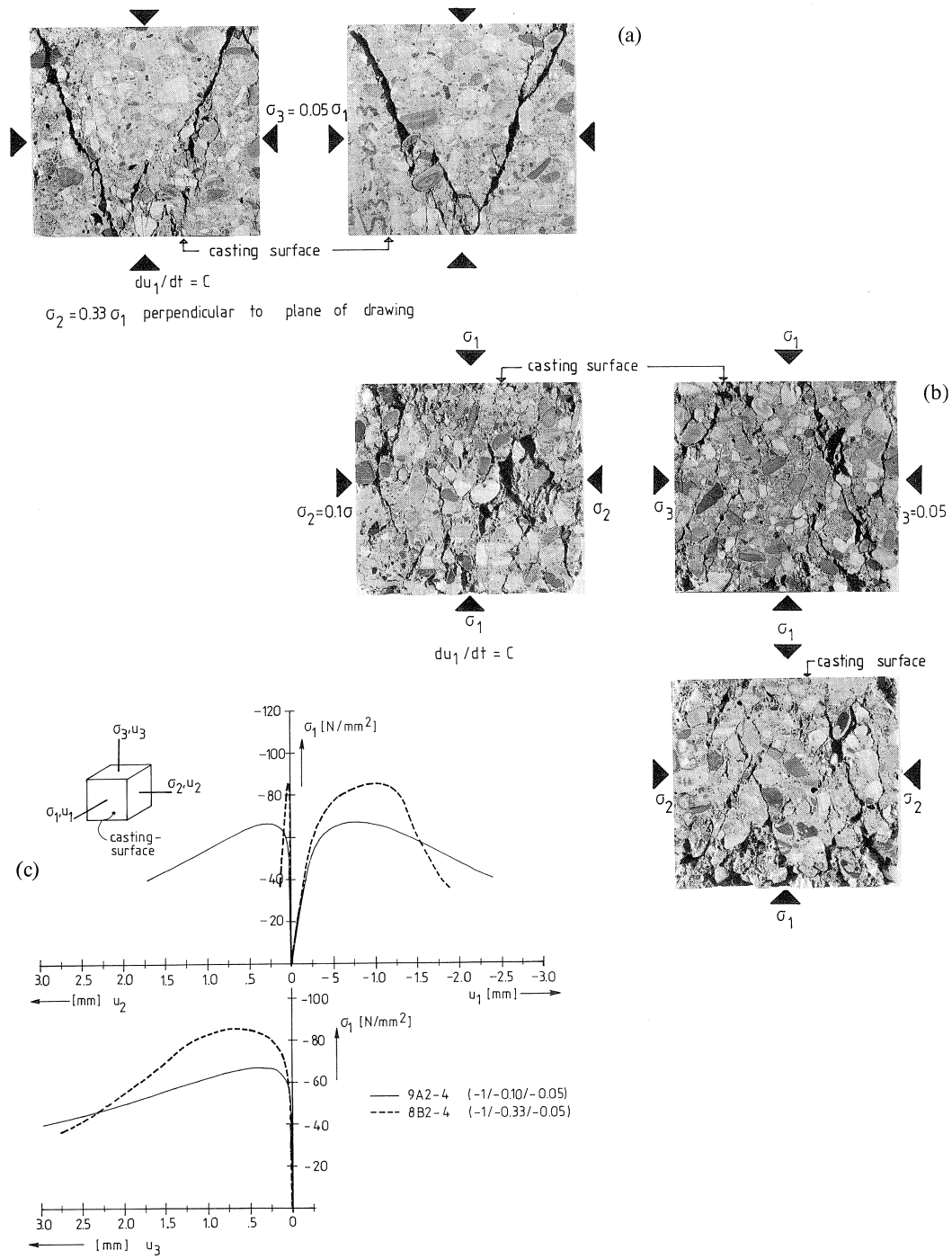
Fig. 1.34. Fracture modes and stress-displacement curves for two multiaxial constant stress-ratio experiments. Fig. (a): Fracture pattern for specimen 8B2-4 $(\sigma_1/\sigma_2/\sigma_3 = -1.0/-0.33/-0.05)$, Fig. (b): Fracture pattern for specimen 9A2-4 $(\sigma_1/\sigma_2/\sigma_3 = -1.0/-0.10/-0.05)$, and Fig. (c): stress-displacement curves.

cube were removed to a depth of approximately 2 mm. Although the grinding of the highly fractured cubes was carried out very carefully, it could not be avoided that some of the surface material was torn loose during the grinding process.

In Fig. 1.34 the fracture modes of two triaxially loaded specimens are shown. In Fig. 1.34.a and b, respectively the fracture pattern of specimen 8B2-4 $(\sigma_1/\sigma_2/\sigma_3 = -1.0/-0.33/-0.05)$ and specimen 9A2-4 $(\sigma_1/\sigma_2/\sigma_3 = -1.0/-0.10/-0.05)$ are shown. The stress-displacement curves for both experiments are shown in Fig. 1.34.c. The distinct stress-displacement response observed in these two experiments, leads to different fracture models. In the experiment 8B2-4, a pronounced shear band developed in the plane formed through the major and minor compressive stresses. In the other experiment (Fig. 1.34.b), a rather crumbly structure appeared after test-termination. A closer view of Fig. 1.34.b, reveals that the "crumbly" structure is the result of mutually crossing shear-bands. In similar experiments, in which two large tensile deformations occured, such a distributed fracture mode was observed. In all experiments where only one large tensile deformation was allowed, a discrete shear-band developed through the plane of the major and minor compressive stresses. In the latter case, the concrete cube seemed to desintegrate into a few more or less intact rest-pieces, separated by weak joints. It should be mentioned however, that it was still rather difficult to separate these rest-pieces from one another (for example, the wedge shaped rest-pieces of the cube shown in Fig. 1.34.a, could not be removed from each other by hand).

Two additional examples of discrete shear-band development are shown in Fig. 1.35. In this figure (1.35.c), the stress-displacement curves of two constant displacement-ratio experiments $(u_1'/u_2' = -1.0/-0.33)$ are shown. The two experiments were carried out at different levels of confinement in the third principal direction $(\sigma_3/\sigma_1 = \beta)$. Specimen 9B2-2 was loaded at the lower confinement level, $\beta = 0.05$, the other specimen, 8A1-5, was loaded at the higher confinement level $\beta = 0.10$. In Fig. 1.35.a and b, the final structures of both specimens are shown. The specimen at the lower confinement level (9B2-2), was loaded until the residual stress-level in the $\sigma_1 - u_1$ diagram was almost reached. The experiment was terminated when $u_3 \approx 3$ mm, and from figure 1.35.a, it can be seen that the discrete shear-band had developed completely at two opposite surfaces. In the other specimen (8A1-5), loaded at the higher confinement level, the shear-band had advanced only partly. This particular experiment had to be terminated while the maximum allowable displacement was reached in the minor compressive direction $(u_3 \approx 3$ mm, see Fig. 1.35.b). At this moment, the specimen was loaded just beyond peak as can be seen from the load-displacement curve measured in the major compressive direction $(\sigma_1 - u_1)$. It should be mentioned, that no differences in fracture mode occured due to the differences in confining stress σ_3. This was already indicated in Fig. 1.29, where stress-displacement curves for three "plane-strain" experiments were shown. Irrespective of the level of confinement, the same descending branch was measured. Fracture modes of specimens loaded at the higher confinement level are reported in Van Mier [1984b]. It should be mentioned that the softening branch could not be measured in several of the experiments loaded at the higher confinement level $(\beta = 0.10)$. More particularly, some of the experiments that were loaded parallel to the

$\sigma_3 = 0.05\,\sigma_1$

(a)

casting surface

$du_1/dt = C$

$u'_2 = 0.33\,u'_1$, perpendicular to plane of drawing

casting surface

$\sigma_3 = 0.10\,\sigma_1$

(b)

$du_1/dt = C$

$u'_2 = 0.33\,u'_1$, perpendicular to plane of drawing

— · — 8A1-5 $\sigma_3/\sigma_1 = 0.10$
—— 9B2-2 $\sigma_3/\sigma_1 = 0.05$

(c)

σ_1, σ_2 [N/mm^2]

-160
-140
-120
-100
-80
-60
-40
-20

$\sigma_1 - u_3$

$\sigma_1 - u_3$

$\sigma_1 - u_1$

$\sigma_2 - u_1$

$\sigma_2 - u_1$

$\sigma_1 - u_1$

3.0 2.5 2.0 1.5 1.0 .5   0   -.5 -1.0 -1.5 -2.0 -2.5 -3.0

[mm] u_3

u_1 [mm]

σ_3, u_3
casting-surface
σ_2, u_2
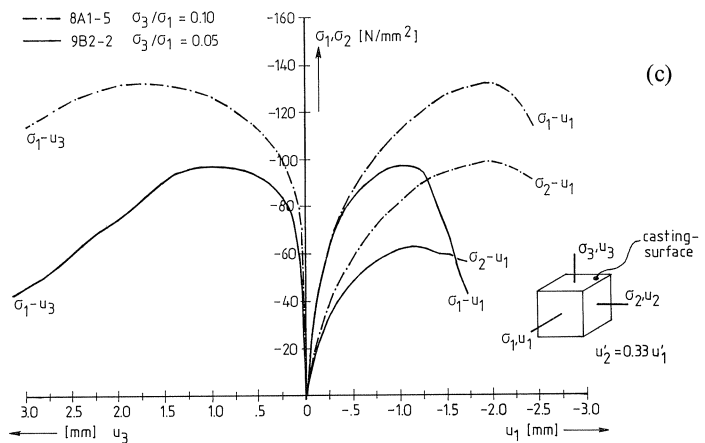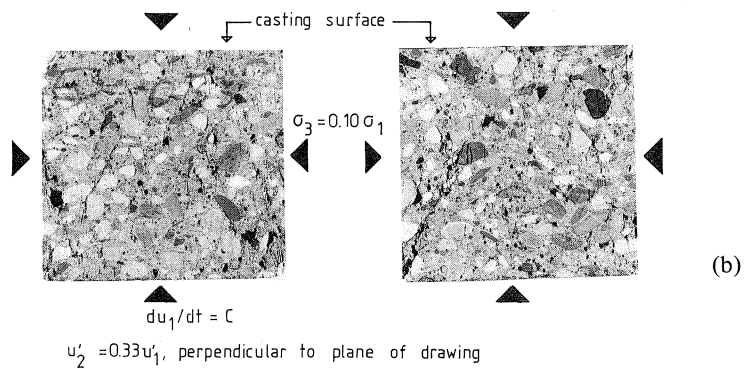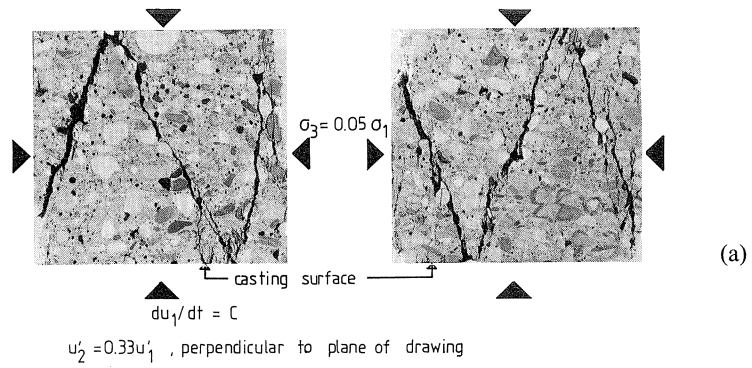σ_1, u_1
$u'_2 = 0.33\,u'_1$

Fig. 1.35 Fracture modes and stress-displacement behaviour for two constant displacement ratio experiments. Fig. (a): Fracture pattern for specimen 9B2-2, $u'_1/u'_2 = -1.0/-0.33$, $\sigma_1/\sigma_3 = -1.0/-0.05$. Fig. (b): Fracture pattern for specimen 8A1-5, $u'_1/u'_2 = -1.0/-0.33$, $\sigma_1/\sigma_3 = -1.0/-0.10$. Fig. (c): Stress-displacement curves.

direction of casting could be followed only partly in the descending branch (see also the results of the "plane-strain" tests in Fig. 1.32).

The results shown in Fig. 1.35, suggest strongly that the macroscopic fracture plane, or shear-band, develops gradually through the specimen's cross-section while the overall stress-displacement curve describes a descending branch. Similar observations were reported by Hallbauer etal. [1973] for quartzite specimens. The geometry of the specimen changes constantly in this stage, and the stress and deformation distributions within the specimen will be highly non-uniform.

Shear-band inclinations

In the multiaxial compression experiments, the shear-bands developed in planes in which a large compressive displacement occured in combination with a large tensile displacement. The normal on a shear-plane always was oriented perpendicular to the direction of the intermediate compressive stress.

For several multiaxial compression experiments, the average of the shearband inclination φ with the direction of the major compressive stress, was measured. The results are gathered in Table 1.6. (Note: the average inclination of all shear-bands in a specimen is indicated). The shear-bands are not smooth but showed rather large local and global curvatures. Therefore φ was derived from the slope of the straight lines connecting two points on the same shear-band, but at the opposing loading platen. In the preliminary biaxial experiments, similar values were measured, and are in agreement with values reported by Kupfer [1973]. He reported values of approximately 30° in uniaxial compression, and 18–27° for the biaxial compression experiments.

Table 1.6. Average value of shear-band orientation φ, with respect to the major compressive direction σ_1.

specimen	ld	lp	α	β	φ
9B1-2	perp.	S	0.10	0.05	20
9A2-4	para.	S	0.10	0.05	24.5
8B2-4	para.	S	0.33	0.05	21
9B1-5	perp.	S	0.33	0.10	25
9A2-5	para.	S	0.33	0.10	21.5
8B2-5	para.	D	0.0	0.05	21.5
9B2-3	para.	D	0.10	0.10	25
9B2-2	para.	D	0.33	0.05	20

$\sigma_1 < \sigma_2 < \sigma_3$
triaxial compression
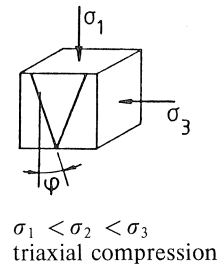
ld = loading direction (see Fig. 1.20)
lp = loading path
S = stress-ratio
D = displacement-ratio

At this point some experimental results obtained by Kotsovos [1983] may be recalled. In a series of uniaxial compression tests on concrete cylinders (of size ⌀ 100 x 250 mm, and uniaxial strength f_c = 51 N/mm^2), loaded with different load application systems, a

decreasing slope of the softening branch was measured when the shear at the specimen - loading application system boundary was reduced. The loading application systems tested by Kotsovos were (in order of decreasing restraint): "active restraint", rigid steel platens, brushes, MGA-pads and rubber. Not only, a decreasing slope of the softening branch was measured, but also the inclination of the shear-bands observed in the different experiments was reduced considerably. For the brushes, similar fracture modes were found as those observed in the current investigation, yet when MGA-pads or rubber layers were used, a more splitting type of failure was observed, and a discrete macrocrack ran almost parallel to the compressive direction. In the experiments with higher restraint, the shear-band developed from one specimen edge to the diagonally opposite edge. The shear-band appeared wider when the fracture modes of cylinders loaded with active restraint were compared to the results obtained with dry steel-platens. These results make it very difficult to decide if the measured shear-band inclinations are really material properties, or rather properties of the complete structure formed by the loading platen and the specimen.

In this context, once more the influence of allowable rotations of the loading platens should be mentioned [see Newman & Sigvaldason 1965/66, Nelissen 1972, Paterson 1978]. In the experiments of Kotsovos [1983], as well as in the current tests, the specimens were loaded with one platen effectively pinned, whereas the other platen could rotate freely. This set-up may induce failure along a single shear-plane, and in fact as soon as the shear-band starts to develop (as explained in the previous section), the process is accelerated due to rotation of one of the loading platen. In this context, two mutually crossing shear bands (in hour-glass configuration) are to be expected when both loading platen are effectively pinned. As a matter of fact, in recent true triaxial experiments carried out by Michelis & Demiris [1984] and Michelis [1985a, b], mutually crossing shear-bands (in hour-glass configuration) were observed in marble specimens. However, in these experiments on prisms of size 50 x 100 mm^3, the axial load was applied through two *rotating* rigid steel platens, whereas the confining stresses (σ_2 and σ_3) were applied through a series of steel prisms in the intermediate direction and through a fluid in the minor compressive direction. Thin lubricated copper plates were inserted between the specimen and the different loading platen. This measure however hardly affects the differences in axial stiffness of the three loading systems, and which may be of influence on the complete specimen deformation. The influence of these mixed boundary conditions on the observed fracture modes is not clear. Yet, from a close scrutiny of the machine developed by Michelis & Demiris, one might get the impression that the spherical seatings are not very effective. At least in the intermediate loaded direction, the loading platens also cover the sides of the spherical seating, which may then be prevented from rotating.

In the current experiments, the concrete rest-pieces in between of the discrete shear-bands seemed to be almost uncracked. The shear-band seemed to develop through an almost uncracked material structure (Fig. 1.35), but from previous research it is known

that a distributed network of microcracks develops when the specimen is loaded in the "pre-peak" region [e.g. Hsu etal. 1963, Stroeven 1973, Attiogbe & Darwin 1985]. When the shear-band has developed completely through the specimen's cross-section, the deformations seem to be the result of sliding in the shear-bands, in combination with local crushing on top of the conical rest-pieces. The latter mechanism will prevail when the residual stress-level in the descending branch is reached. In rock-mechanics frequently the assumption is made that unloading occurs in these "uncracked" rest-pieces [Bieniawski 1967, Sture & Ko 1978]. This assumption seems to be confirmed by the "plane-strain" experiments, by the unloading observed in the intermediate stressed direction. Unloading is observed to occur immediately when a softening branch develops in the major compressive direction (see Fig. 1.29).

Classification of fracture-modes

In Fig. 1.36, the observed fracture modes are shown in "stress-space". The classification is valid only for the range of experiments that were carried out, viz. $0 \leq \beta \leq 0.10$.
A few typical transition regions can be distinguished. First, when σ_3 is constant, a transition in the compressive region is defined by $u_2 = 0$. The "plane-strain" tests define (theoretically) the transition between the two distinct failure modes that were observed in the current experiment. When one large tensile deformation occurs in an experiment, failure is "uni-directional" and a discrete shear band developed normal to the intermediate compressive direction (Fig. 1.34.a). When two large tensile deformations can occur, failure is "two-directional", and a more distributed type of rupture mode is observed (Fig. 1.34.b). Of course the transition between the two types of failure modes
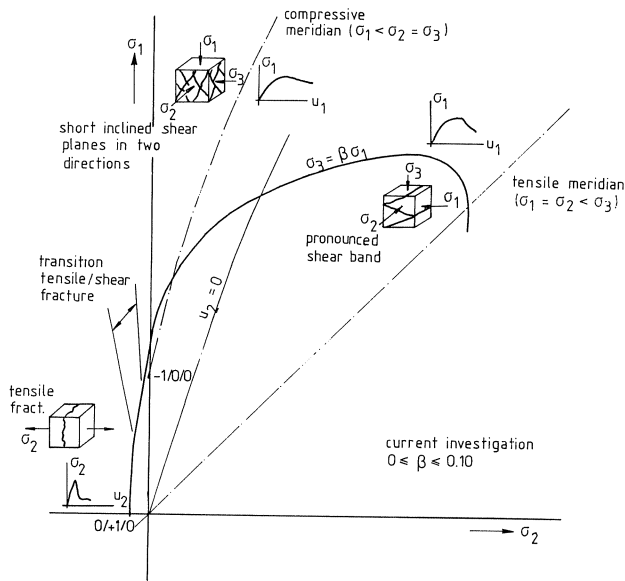

Fig. 1.36. Classification of fracture modes.

will not be very sudden, and may even not coincide with the $u_2 = 0$ criterion. Discrete shear bands or distributed fracture may appear depending on the ratio between the two tensile deformations.

Another transition, from distributed to discrete failure occurs when the contours $\sigma_3 = \beta \sigma_1$ are followed in the direction of the σ_1-axis. For stress combinations $-1/0/ - \beta$, discrete fracture can occur, depending on the value of β. When the contour $\sigma_3 = \beta \sigma_1$ is followed further into the tension-compression-compression region (for non-zero β values), a transition from discrete shear failure to cleavage (tensile) failure will be reached. In this region, however, only a limited number of experiments was carried out, and the transition cannot be defined clearly on basis of the current experiments. From biaxial investigations, Isenberg [1968] found that the cleavage-shear failure transition occurs when $\sigma_1/\sigma_2 \approx 17$.

The transition in the compressive region, from uni-directional failure to two-directional failure (near combinations with $u_2 = 0$, or $\sigma_2/\sigma_1 \approx -0.33/ - 1.0$), is predicted on basis of micro-mechanical considerations [e.g. Sammis & Ashby 1985]. However similar considerations do not lead to a prediction of the cleavage – shear failure transition, and considerations based on mode I cracking only, are not sufficient anymore in the latter case. The above transitions all occur along contours $\sigma_3 = \beta \sigma_1$. When β increases, the transition from brittle to ductile failure will be reached. The experimental results indicate that for load-paths close to or coinciding with conventional triaxial compression $(\sigma_1 < \sigma_2 = \sigma_3)$, this transition almost may have been reached. The slope of the softening branch of stress-ratio experiments $-1/-0.1/-0.1$ (Fig. 1.30 and 1.34.c) has been decreased already considerably. Jamet et.al. 1984, report that transition occurs when $\sigma_2/\sigma_1 = 0.25-0.30$. In this context also the results obtained by Palaniswamy & Shah [1974] may be recalled. Under low confining pressure significant microcracking and a decrease of pulse velocity was observed, whereas under high confinement very little microcracking and drop of pulse velocity was measured. Unfortunately, they were not able to measure the implications in the post-peak range with their load-controlled testing machine.

In the region where failure occurs dominantly in one direction under the formation of a discrete shear band, the results indicate that the transition is still far away. The stress-displacement diagrams, as for example those of Fig. 1.29, show no decrease of the softening branch when the confinement is increased. The limiting case for stress combinations for which uni-directional failure will be observed is the classical extension test $(\sigma_1 = \sigma_2 < \sigma_3 < 0)$. From rock-mechanics it is known that in such experiments, the transition from brittle to ductile behaviour occurs at extremely high levels of confinement σ_3 [see in Paterson 1978]. Two pilot tests were carried out along the tensile meridian, for which the strength failure points are indicated in Fig. 1.24. Both experiments showed a very unstable and steep descending branch. These stress-combinations, under which severe out-of-plane cracking occurs are considered as the most unfavourable and dangerous loading combinations in the triaxial compression region.

52

1.5 Rotation experiments

In a second series of triaxial tests several 'rotation experiments' were carried out. As pointed out by Bažănt [1983], no continuous loading axes rotation at angles $0 < \psi < 90°$ can be carried out in a cubical multiaxial cell. Abrupt rotations are no problem, and may obtained by sawing an inclined specimen from a pre-cracked (initially larger) specimen, and loading it again. As an alternative, Bažănt proposed cylindrical specimens subjected to axial load, lateral or internal pressure (i.e. solid or hollow cylinders may be used) and torsion. However, certainly problems will be encountered in such experiments as well, as the shear stress distribution varies with the distance to the cylinder axis in solid cylinder tests. The influence of this non-uniform stress-distribution on the mode of fracture is not clear.

In the multiaxial cubical machine, very easy 90° rotation experiments could be carried out, and main emphasis in this section is on results obtained from such experiments. Main advantage of the abrupt 90° rotation tests, which implied a simple change of the minor and major loading directions, is that the specimen could remain in the cubical machine. Note that the displacement-ratio experiments (that were reported in the previous sections), are in fact also 90° rotation tests. Some abrupt small angle rotation experiments were carried out as well, but are reported elsewhere [van Mier 1984b]. These latter experiments are more complex and difficult to interpret.

Type I and II rotation tests

In view of the two basic fracture modes observed in the triaxial experiments under proportional stress and/or displacement paths, two types of 90° experiments were defined. These two loading cases are:

1. Type I rotation test

In the type I rotation experiments (see Fig. 1.37.a), the first loading was carried out following $\sigma_1/\sigma_2 = -1/-0.5$, and $\sigma_3 = $ constant $= -1$ N/mm². The first loading was carried out until an arbitrary point $(\sigma_{1,unl.} - u_{1,unl.})$ in the stress-displacement curve, measured in the major stressed direction, was reached. Under these loading conditions, a discrete shear band will develop through the specimen in the plane formed through the major and minor stressed directions (see section 1.4). Near the unloading point the shear-band will have developed to some extent, and the specimen can be described as highly damaged.

Subsequently, the 90° rotation was carried out, and the major and minor compressive direction were changed. This was done after the specimen was unloaded to $\sigma_1 = -1$ N/mm². The second loading was now applied, following $\sigma_3/\sigma_2 = -1/-0.5$, and $\sigma_1 = $ contant $= -1$ N/mm². This second loading was applied until a tensile displacement of 2.0 mm was measured in the minor compressive direction (σ_1). Occasionally, an unloading/reloading cycle was carried out, as the maximum stiffness in the reloading path may be used as an indication for the damage that was sustained to the specimen [Van Mier 1984b, sec. 5.2.6].
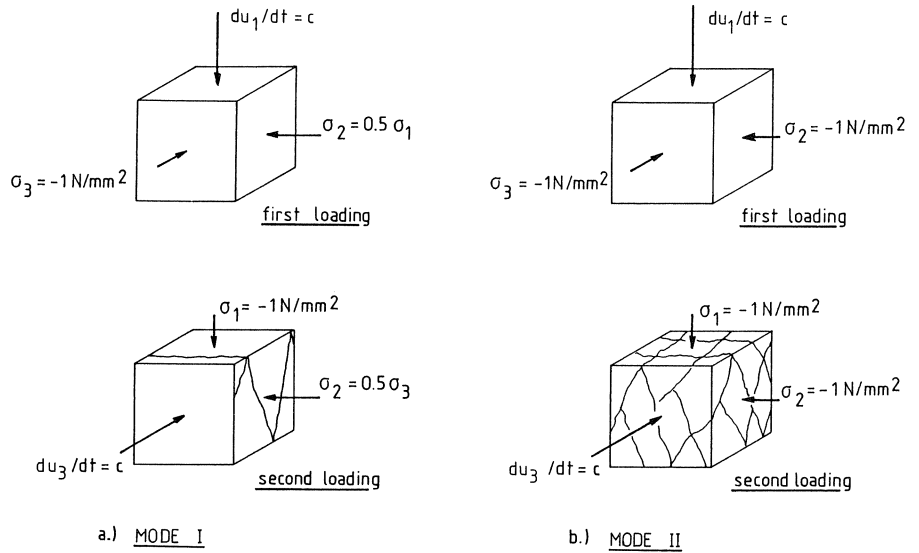
Fig. 1.37. Mode I (Fig. a.) and Mode II (Fig. b.) rotation experiments.

2. Type II rotation test

In the type II rotation tests (Fig. 1.37.b), the loading combination was chosen in such a way that two large tensile deformations could occur. The specimen was loaded by a displacement control in the major compressed direction (i.e. d u_1/dt = 1 μm/s), whereas in the two other directions a small constant confining stress was applied, $\sigma_2 = \sigma_3 = -1$ N/mm^2. Again, the specimen was loaded up to an arbitrary point in the descending branch of the major stress-displacement curve ($\sigma_1 - u_1$), whereafter it was unloaded to $\sigma_1 = -1$ N/mm^2. After rotation, the specimen was loaded following d u_3/dt = 1 μm/s, and confining stress $\sigma_1 = \sigma_2 = -1$ N/mm^2. An experiment was terminated when a tensile displacement level of 1.5 mm was reached in both minor compressed directions.

The direction of casting was defined with respect to the major and minor compressive direction in the first loading sequence. Thus when loading was applied parallel, the direction of casting coincided with the major compressive direction σ_1, and when the loading direction was perpendicular, the direction of casting coincided with the minor compressive direction σ_3. This implies that after rotation the situation was reversed as far as the orientation of the initial damage field with respect to the applied major compressive stress is concerned.

Stress-displacement behaviour

In figure 1.38 the response of a mode II rotation experiment is shown. The specimen was loaded perpendicularly. In Fig. a, the $\sigma_1 - u_1$ curve is shown, in Fig. b, the $\sigma_1 - u_2$ curve, in Fig. c, the $\sigma_1 - u_3$ curve and in Fig. d, the displacement paths $u_1 - u_2$ and $u_1 - u_3$. The first loading leads to a maximum stress σ_{1p} whereafter a smooth des-

cending branch is measured. After an additional unloading-reloading cycle, the specimen was unloaded, and the major and minor stressed directions were changed. From Fig. 1.38.d, it is obvious that the initial loading up to the rotation point yielded a similar result (in terms of displacement paths) as shown before for the stress-ratio experiments (Fig. 1.27.b). Note that in the minor compressive direction σ_3, the $\sigma_3 - u_3$ curve before rotation is the horizontal line parallel to the u_3-axis (before rotation $\sigma_3 = -1$ N/mm^2). After rotation, $\sigma_1 = -1$ N/mm^2, and the $\sigma_1 - u_1$ relation appears as a straight line in Fig. 1.38.a, but in the σ_3 direction another limit point is reached (Fig. c.), whereafter a second stable softening branch is measured. Yet, the limit point σ_{3p} is considerably lower than the limit point measured in the first loading sequence (σ_{1p}). The damage sustained to the specimen in the first loading is held responsible for this decrease of maximum carrying capacity. The stiffness of the ascending branch of the $\sigma_3 - u_3$ curve shows a significant 'run', and the effect must be attributed to closure of cracks that developed during the first loading sequence. When an unloading-reloading cycle was carried out in the ascending branch, it was found that the maximum tangent stiffness increased considerably [van Mier 1984b], which may indicate an increase of contact surface in the crack planes.

Close scrutiny of the stress-displacement curves yields some other typical behaviour in the lateral directions after rotation. Note for example the small horizontal branch in the
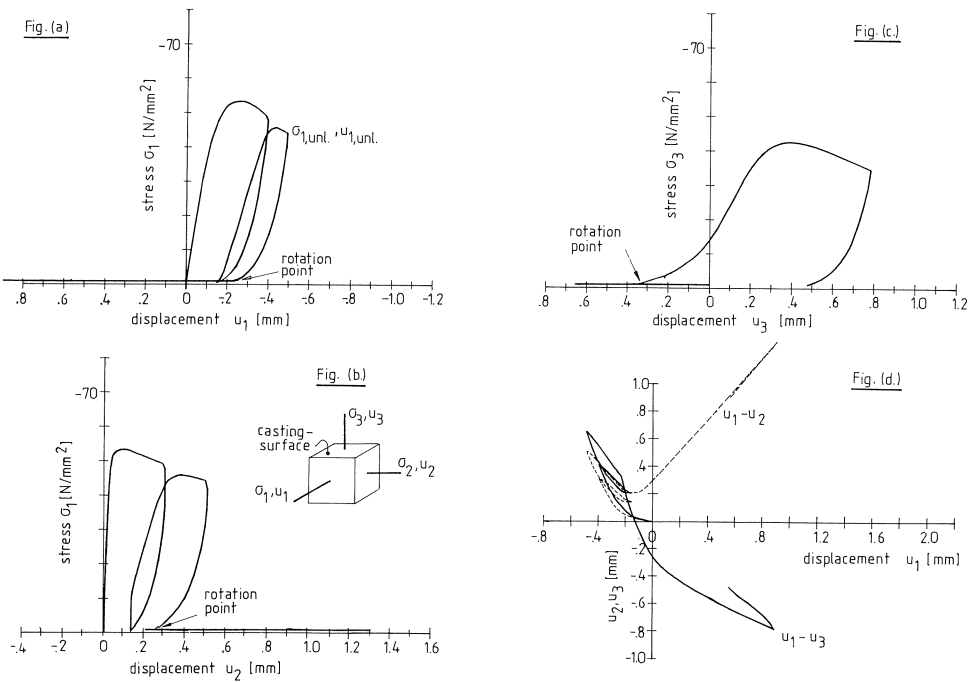

Fig. 1.38. Results of mode II rotation test 7A1-3, loading direction perpendicular, $\sigma_1 - u_1$ curve (Fig. a.), $\sigma_1 - u_2$ curve (Fig. b.), $\sigma_3 - u_3$ curve (Fig. c.), and displacement paths $u_1 - u_2$ and $u_1 - u_3$ (Fig. d.).

55

$\sigma_1 - u_2$ curve at the left of the rotation point. Obviously, the displacement in the u_2 direction decreases when σ_3 is applied (after rotation), whereas the other lateral strain after rotation (u_1) shows an immediate increase. The effect may be explained by considering the cracked structure after the first loading. Crack planes have developed perpendicular to the u_2 direction in the first loading sequence. These cracks obviously have to be closed again before u_2 will increase. The decrease of u_2 may be explained from relative displacements of the existing cracks surfaces with regard to one another, leading to crack closure. No cracks have developed perpendicular to the σ_1 direction in the first loading sequence, and consequently no disturbances will occur in this direction.

The major difference between the type I and type II rotation experiments is shown in Fig. 1.39. A direct comparison is made between the major compressive stress-displacement curves before and after rotation. In Fig.a, the $\sigma_1 - u_1$ curve (before rotation), and the $\sigma_3 - u_3$ curve (after rotation) are plotted in the same diagram for a type I rotation test (specimen 7A1-2). In Fig. b, a similar plot is shown for a mode II rotation experiment (specimen 7A1-3). Both specimens were loaded perpendicular.

The most important difference between the mode I and mode II rotation experiments is the peak stress level that can be reached after rotation (σ_{3p}). In the mode II experiment (fig. b.), and as shown before, the carrying capacity of the specimen has decreased considerably after rotation. Even the unloading stress in the first loading sequence ($\sigma_{1,unl.}$) is not exceeded and the figure suggests that the same softening branch is followed, both before and after rotation. For all mode II rotation tests such behaviour was observed [Van Mier 1984b].

The mode I experiment showed a distinct behaviour after rotation. The pre-peak behaviour after rotation was almost similar, and also in this case the long initial "run" in the $\sigma_3 - u_3$ curve suggests that crack closure occurs (which is no surprise in view of the mode of fracture; in this experiment, as a result of the first loading, cracks mainly develop in planes perpendicular to the σ_3 direction. Yet, although quite some damage was sustained to the specimen in the first loading, the same peak-stress was measured in the second loading after rotation, and the softening branches developed parallel to one
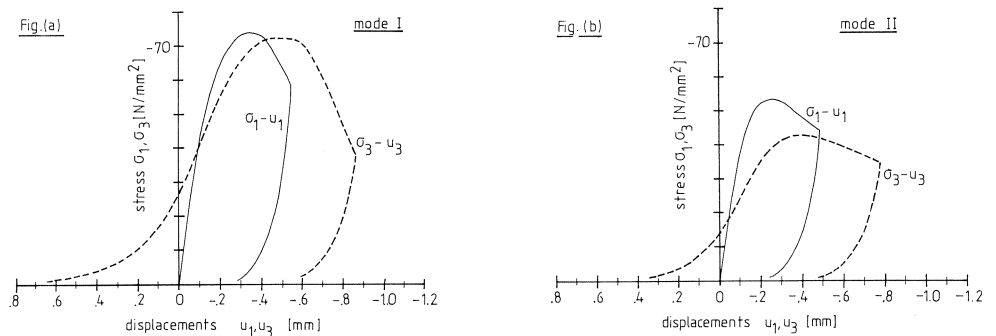

Fig. 1.39. Response of a Mode I (Fig. a.) and a Mode II (Fig. b.) rotation experiment.

another (fig. 1.39.a.). Obviously, the severe cracking due to the first loading does not affect the fracture behaviour of the specimen after rotation. The crack structure that evolved from the first loading must be considered passive with regard to the second loading as far as the fracture characteristics are concerned. Note that the shape of the softening branches in the mode I and the mode II experiments, before and after rotation, is similar to those of the uni-directional and two-directional fracture modes respectively (see section 1.4).

1.6 Concluding remarks

In this part, results of several displacement controlled uniaxial and multiaxial compression experiments were reported.

The results of several uniaxial compression tests on 100 mm cubes and prisms with varying height were described and interpreted in terms of structural changes. An uniaxial experiment was essentially considered as a special case of triaxial loading. Main conclusion from these experiments was that in the post-peak region the specimen is deformed highly non-uniform. Fracture initiation occurs at the outer layers, and the remaining carrying capacity seems to be the result of a "more or less" intact core. The roots for these non-homogeneous deformations have likely developed in the pre-peak region, when the specimen's response is influenced by microcrack processes. The impression is that the pre-peak microcrack processes are largely influenced by interactions between the specimen and the loading application system.

It was shown that fracture in uniaxial compression is a localized phenomenon, similar to the fracture process observed in uniaxial tension. The differences between the tensile and compressive loading cases are manifested by different orientations and properties of the macroscopic fracture planes. From uniaxial compression tests on prisms with varying heigth it was found that the fracture plane (which was a continuous shear plane in the experiments on high prisms, $h = 200$ mm) takes the form of a zig-zag band when the specimen's height is decreased.

Localized failure also was observed under multiaxial loading conditions, and in fact as long as the brittle ductile transition is not exceeded, localized failure will occur both under tensile and compressive loadings. Only by applying different loading combinations, the macroscopic fracture plane will have different orientations. In the softening region of the load-displacement curves, the cross-sectional area of a specimen decreased in the triaxial compression experiments by the propagation of a shear band through the specimen's cross-section.

The concrete used showed initial anisotropy. The pre-peak load-displacement curve was affected by changing the specimen's initial orientation, yet the softening branch was independent and the results indicate that macroscopic failure proceeds independent of the pre-peak behaviour. It is hypothesized that the shape of the softening branch depends mainly on the specimen's geometry, boundary conditions, and the applied loading combination. This hypothesis is confirmed by the rotation experiments, in

which mainly the pre-peak load-displacement curve was influenced when the major and minor stresses were exchanged after some damage was sustained to a specimen. Yet the softening branch always was similar irrespective of the specimen's loading history. It should be mentioned however, that the rotation experiments were restricted to 90° jump rotations. The above hypothesis is worked out further in part II.

2   Fracture propagation in concrete

In recent years, the development of numerical methods in engineering has had an enormous impact on the development of constitutive models for plain concrete. Stress-strain curves, derived from load-displacement diagrams obtained in experiments as those described in part 1 are normally used for tuning a model. Often macroscopic models are proposed, based on resemblances at the "load-displacement" level with other materials (i.e. with different micro-structures). For example plasticity models, originally developed for describing the behaviour of metals, were adopted for describing concrete stress-strain behaviour [e.g. Chen 1982]. These models may suffice for describing the pre-peak stress-strain behaviour, yet softening and material instabilities violate the basic assumptions of the classical framework. Complicated non-associated flow rules [e.g. Han & Chen 1984, Vermeer & De Borst 1984] are needed to model dilation (Fig. 1.33). In order to deal with softening (as a continuum phenomenon), alternative formulations were proposed, such as models decomposing strain in an additional fracture component and based on a formulation in strain-space using Il'yushin's postulate [Dougill 1976, Han & Chen 1984]. More recently a model based on friction hardening and cohesive softening was formulated in order to deal with the deficiencies of the classical theory [Vermeer & De Borst 1984].

It is rather questionable if such models, aimed at directly describing the macroscopic stress-strain behaviour as observed in "material experiments", can be used in finite element codes for predicting the response of structures with different geometries. As shown in part 1, the interactions between the experimental environment and the material sample are still very important at this „macroscopic" level. Especially in the softening region, it becomes more and more debatable if a continuum description of the observed behaviour is still feasible. Quite often in these continuum models, "material parameters" are proposed that lack a sound and solid physical basis, and in the worst case cannot be determined experimentally at all, or cannot be separated from other parameters.

In this context, comments made by Freudenthal in 1950 become timely again:

"Most of our knowledge concerning the mechanical behaviour of engineering materials is derived from phenomenological (large scale) observations, and frequently, an empirical interpretation of a large volume of partially coordinated observed facts. The shortcomings of this approach become more and more evident as the materials increase in complexity, as the conditions of service under which the materials will perform become more diversified, and, finally, as the number of "laws" that must be devised to express the interrelation between the relevant variables necessary increases.

58

In general such "laws" are valid only within the range of the observations that serve as a basis for their derivation... Hence, the volume of experimental work required to provide the empirical "laws" needed to solve the increasingly complex problems of engineering design becomes especially unwieldy".

It is good to realize that the macroscopic load-displacement relationships depend largely on processes acting at a lower size level. The macroscopic behaviour becomes predictable, at least qualitatively, from knowledge of the internal structure of the material. This approach has been followed for some time now for modelling the behaviour of geologic materials [e.g. Brodsky 1985, Costin 1983, Costin & Stone 1986, Horii & Nemat-Nasser 1985, Moss & Gupta 1982, Stevens & Holcomb 1980], and more recently also in the field of concrete mechanics [Ortiz 1985]. An approach, taking into account processes acting at a lower size level seems inevitable when fracture conditions are investigated, or when anisotropy can occur. Such an approach seems inevitable especially when the influence of the experimental environment on the measured load-displacement response of the material becomes significant.

2.1 *Physical Model*

Based on the experimental observations in part 1, a physical model for concrete fracture is proposed. Below, the principal outline of the model is given, whereas the hypothesis is worked out for the "post-failure" region.

Isolated microcracking

Consider a specimen loaded in uniaxial or multiaxial compression at low confinement such that brittle failure can occur (see section 1.4). Due to the heterogeneous material structure [at the submacroscopic level, see Wittmann 1982], crack nucleation and propagation will occur when an external load P is applied. From a mechanics point of view any material or geometric discontinuity may serve as a stress concentrator, and hence promote nucleation and growth of cracks [Horii & Nemat-Nasser, 1985]. The increase of crack length will however be restricted while the heterogeneity of the material provides not only for "crack initiators", but for several crack arrest mechanisms as well [see Gücklich 1963, and Shah & McGarry 1971]. For example, a crack approaching an interface with higher stiffness only will propagate when the external load is increased.
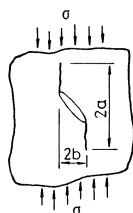

Fig. 2.1. Crack growth from an inclined crack in a compressive stress field, after Glücklich 1963.

Cracks in a compressive stress field are arrested while the cracks tend to propagate parallel to the compressive direction as indicated by Glücklich 1963 and Sammis & Ashby 1985 (see Fig. 2.1).

When it is assumed that linear elastic fracture mechanics concepts are valid at the submacroscopic level, the energy released due to the extension of N cracks with semi-major axis a_i ($i = 1,2,...,N$) in a plate of unit thickness, to $a_i + \Delta a_i$ ($\Delta a_i \ll a_i$), under the action of a local tensile stress $\sigma_i(p)$ (which depends on the external applied nominal stress p), and a geometrical factor Y_i, can be written as

$$\Delta W_{I,c} = \sum_{i=1}^{N} \left(2a_i \cdot \Delta a_i + (\Delta a_i)^2\right) \cdot \frac{\pi \sigma_i(p)^2}{E} \cdot Y_i \qquad (2.1)$$

where $\Delta W_{I,c}$ denotes the energy released upon reaching the external stress level p, and where E is the average elastic modulus of the composite material. The factor Y_i will depend on the local geometry of a crack, but also on the size of the crack compared to the specimen dimensions. In fact Y_i will be close to 1 if the microcrack size is small compared to the specimens dimensions.

The average elastic modulus of the material is assumed to remain constant during cracking, and only the stiffness of the specimen will decrease during crack propagation. When a material with the same elastic stiffness E as the heterogeneous material is considered, but now without cracks, the amount of energy stored in a specimen with volume $V_s = H \cdot W \cdot 1$, is equal to

$$W_s = \tfrac{1}{2}E\varepsilon_0^2 \, V_s = \tfrac{1}{2}\frac{(p')^2}{E} \cdot V_s \qquad (2.2)$$

The parameters ε_0, p and p' are explained in Fig. 2.2. It should be mentioned that no distinction between cracktypes is made in the present analysis. In concrete technology, cracks are often distinguished according to the material or interface where they appear [e.g. Hsu et al. 1963]. Here the cracks merely serve as a mechanism through which energy is released.

The energy released due to crack extension of isolated microcracks is small compared to the total energy stored in the specimen. The geometrical factor in eq. (2.1) depends on
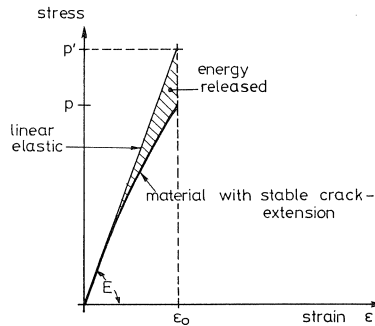

Fig. 2.2.   Energy release due to stable microcrack propagation.

the crack length increment Δa_i and will be several orders of magnitude smaller than the geometrical factor in eq. (2.2), i.e. the specimen volume. The total number of cracks should become very large in order to obtain an energy release of the same order of magnitude as the stored energy. No such increase of number of isolated microcracks has ever been observed at low levels of external stress i.e. $p < 0.3\sigma_{peak}$ [e.g. Carrasquillo et al. 1981, Attiogbe & Darwin 1985, Hsu et al. 1963].

Due to several crack arrest mechanisms, which depend largely on the material structure (e.g. stiffness ratio between aggregate and matrix material, porosity), crack propagation will occur distributed over the entire specimen volume. This is the reason for using the continuum variables stress and strain in Fig. 2.2.

Crack joining

When the size and number of isolated microcracks increases, the distance between two neighbouring crack tips gradually decreases, and the conditions for joining of two or more separate microcracks into a single and longer combined crack [definition after Carrasquillo et al. 1981] are created. The amount of energy released in a crack joining event is considerably larger when compared to the extension of two isolated micro-cracks (under the assumption that the same amount of new cracks surface is formed). The amount of energy released when two isolated microcracks extend from a to $a + \Delta a$ in a plate of unit thickness, under the action of a local tensile stress $\sigma(p)$, can be calculated from eq. (2.1) when the geometrical factor Y is known:

$$\Delta W_{I,c} = 2 \left(2a \cdot \Delta a + (\Delta a)^2\right) \cdot \frac{\pi \sigma(p)^2}{E} \cdot Y \tag{2.3}$$

When the crack tips are close to one another, a crack joining event is inevitable (Fig. 2.3), and the energy released due to the joining event can be expressed by

$$\Delta W_{I,c}^j = (2a + 2\Delta a)^2 \cdot \frac{\pi \sigma(p)^2}{E} Y^j - 2a^2 \cdot \frac{\pi \sigma(p)^2}{E} Y \tag{2.4}$$

The geometrical factors Y and Y^j (j indicates joining) depend on local conditions and are unknown, but it seems reasonable that they differ only slightly as long as the crack length remains smaller than a characteristic specimen dimension. Under the assumption $Y = Y^j$, the surplus of energy released due to crack joining, compared to the energy released from the extension of two single microcracks, follows after subtracting eq. (2.3) from eq. (2.4):

$$\Delta W_{I,c}^j - \Delta W_{I,c} = \left(2a^2 + 4a \cdot \Delta a + 2(\Delta a)^2\right) \frac{\pi \sigma(p)^2}{E} Y \tag{2.5}$$

The energy release is now governed by the cracklength a, instead of the crack length increment Δa as in the case of isolated crack propagation. In terms of macroscopic stress-strain behaviour, crack joining will be responsible for a significant increase of the curvature of the stress-strain relation. Joining events may appear distributed over the
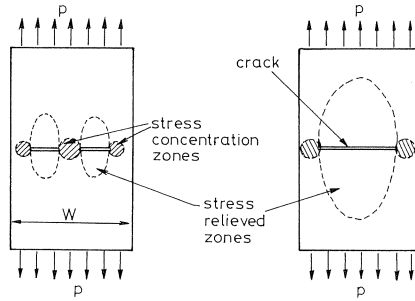
Fig. 2.3.   Increase of stress-relieved zones due to joining of separate microcracks.

complete specimen volume V_s. Yet, if at a certain location a crack joining event occured, it is not likely that a second event will occur nearby. The large increase of stress-relieved zones due to crack joining (Fig. 2.3) will undoubtedly affect the loading conditions of neighbouring cracks. It is postulated that crack joining might even lead to closure of neighbouring microcracks. In fact the mechanism is similar to a branching phenomenon observed in SEM experiments carried out by Diamond and Bentur 1984. They observed a specimen under load, and when two parallel (branching) cracks emanated from a single crack, only one of the crack branches remained active and widened under further increasing load.

Thus crack joining events may proceed distributed over the complete specimen volume, leading to an increase of average crack length, but also to a decrease of the number of active cracks. In this context, a crack situated in a stress-relieved zone can be considered as passive (see Fig. 2.4). It seems reasonable to assume that the continuum variables can still be used.

Due to the crack growth mechanism that was depicted in Fig. 2.1, the combined cracks will be oriented more or less parallel to the major compressive direction. The number of
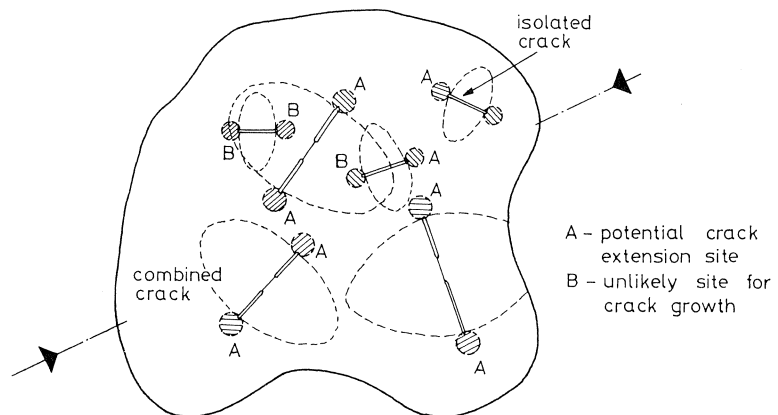

Fig. 2.4.   Development of preferential crack propagation sites due to the increased size of stress-relieved zones.

crack joining events increases under increasing external load, and a significant increase of such events probably occurs when the "minimum volume" boundary is reached (compare with Fig. 1.33). This stress level normally is associated with the long term strength of concrete: when the external load is kept constant at this level, spontaneous fracture will occur after a certain time interval. This may indicate that when the size of the (active) cracks increases, the specimen's response will become increasingly unstable. Crack joining or other crack interaction effects are normally not considered in micromechanics models [e.g. Brodsky 1985, Attiogbe & Darwin 1985, Costin 1983, Moss & Gupta 1982]. Only recently, attention was given to the influence of crack interaction effects on the fracture behaviour as observed in standard triaxial compression experiments [see Horii & Nemat-Nasser, 1985 and Costin & Stone, 1986].

Macrocracking

Upon further increasing external load, the combined cracks will join to form a continuous macrocrack. The size of the stress relieved zones increases, and large volumes of the specimen unload. When an experiment is carried out in "stress-control", a sudden loss of load carrying capacity will be observed. The energy requirement curve (where energy requirement is defined as the total amount of energy needed to deform a specimen up to a certain displacement level, i.e. the area under the load-displacement curve) has reached its maximum slope.

Crackgrowth cannot be controlled by crack arrest mechanisms anymore, and the experiment only wil remain stable when certain boundary conditions are fulfilled. In the experiments described in Part 1, stable microcracking was obtained by using a closed loop servo-controlled loading system in combination with a stiff loading frame. As shown in part 1, the development of the macrocracks is related to a gradual loss of carrying capacity of the specimen, and a softening branch is observed in the stress-displacement diagrams. Localized failure was observed both in the uniaxial compression tests (Fig. 1.17 and 1.18), and in the triaxial compression experiments when the confining stresses were below the brittle-ductile transition. These results confirmed findings from experiments on rock samples [e.g. Bieniawski 1967, Hallbauer et al. 1973, Michelis & Demiris 1984], as well as results obtained in standard triaxial compression tests on concrete cylinders [e.g. Ahmad & Shah 1982, Jamet et al. 1984]. Moreover, as shown in Fig. 1.35, it was found that the macroscopic fracture plane gradually develops through the specimen's cross-section while the overall stress-displacement curve describes a descending branch. This observation is in agreement with the results obtained by Hallbauer et.al. 1973.

As can be seen from Fig. 1.35, the macroscopic fracture plane nucleated from one of the corners, which may be the result of local stress-concentrations. Nevertheless, the results presented, indicate that during the steep part of the descending branch a localized macroscopic fracture plane gradually develops through the specimen's cross-section.

Similar results were recently observed in uniaxial tensile displacement controlled ex-

periments on double notched concrete and rock specimens [Reinhardt 1984, Cornelissen et al. 1986, Labuz et al. 1985, Labuz 1985]. Note that the tensile loading case represents the limiting case along the "tensile meridian" (see Fig. 1.36). Especially interesting in this context is the result obtained by J.F. Labuz of the University of Colorado in Denver, and which is depicted in Fig. 2.5. In this figure, the load-displacement curve obtained from an experiment on a charcoal granite plate of size 75 x 280 mm^2 (and thickness D = 13 mm), in which two 12.5 mm deep notches were made at half height. At different stages in the descending branch, the optically determined crack length (measured under 100 x magnification) is indicated. The macroscopic crack started at one of the notches, and gradually propagated towards the other side of the specimen. The crack length increased from 16.5 mm just beyond peak to 41.9 mm near the residual level. The boundary conditions in these experiments were such that rotations were allowed in the plane of the plate. Labuz et al. 1985, also indicate that hardly any differences in response occur due to the application of notched specimens. In Fig. 2.6 their result is shown. The main difference between the notched and unnotched specimens is the slightly larger curvature of the notched specimen's load-displacement curve just before the peak load is reached. The softening branches of the two curves have the same shape, indicating that the macroscopic fracture plane develops identical in the two specimens.

Similar findings were reported by Reinhardt [1984], and Cornelissen et al. [1986], who did tests on double notched concrete plates. The boundary conditions in the latter experiments was that the loading platens were kept parallel to one another during the experiments by means of a special guiding system. From non-uniform displacement distribu-
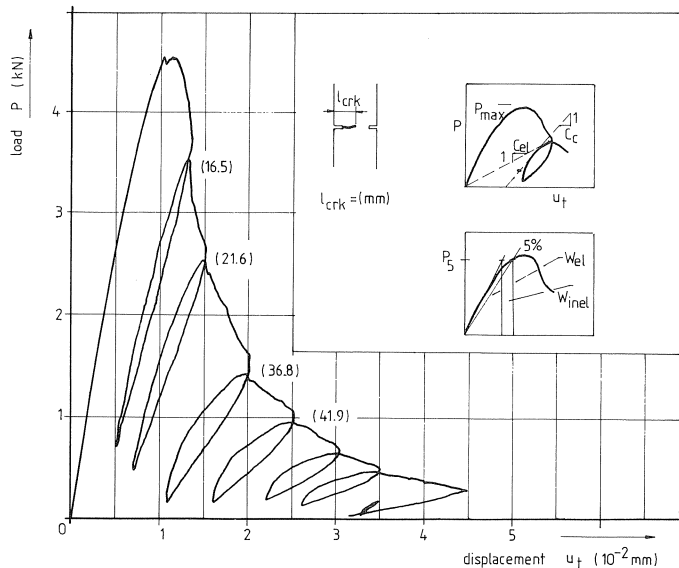

Fig. 2.5. Load-displacement diagram obtained in a direct tension test on a double notched charcoal granite plate, after Labuz 1985.
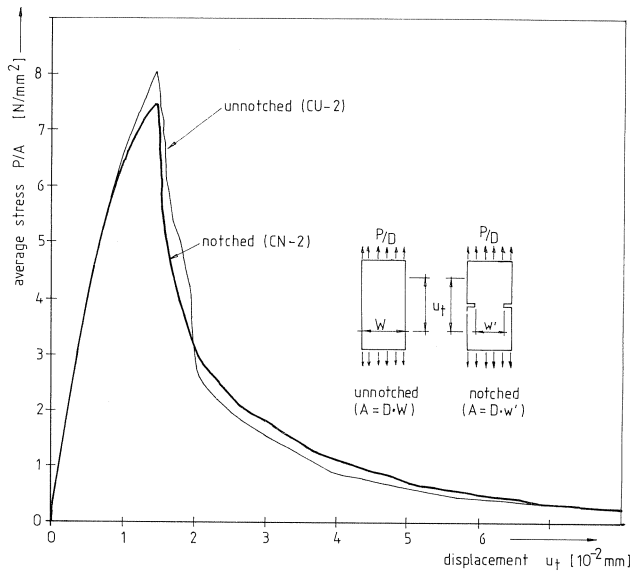
64

Fig. 2.6. Difference in response of notched and unnotched specimens, after Labuz 1985.

tions measured over the width of the plate (between the notches), especially during the steep part of the descending branch, it can be concluded that also in these experiments the macrocrack nucleated from one of the notches whereafter it propagated through the specimen's cross-section.

The differences in boundary conditions may have influence on the details of the macrocrack propagation. As was mentioned in part 1, the allowable rotations of the loading platen in a uniaxial or multiaxial experiment (brittle mode), will determine if either a single macroscopic shear plane will develop, or mutually crossing shear bands (in "hour-glass" configuration), see also Paterson [1978], Newman & Sigvaldason [1965/66] and Michelis & Demiris [1984]. Also in the tensile experiments the allowable rotations of the loading platens are important, as will be discussed in section 2.3.

The three stage fracture process (microcracking, crack joining and localization) is summarized in Fig. 2.7. The process applies to heterogeneous materials with significant differences in the stiffness ratio's of the constituents. In homogeneous materials, the first occurence of microcracking would immediately lead to unstable fracture. The microcracking and joining processes are the result of propagation and arrest mechanisms, which are provided for within the heterogeneous structure of concrete. The appearance of post-peak localization seems a direct result of the joining mechanism. During the fracture process, a gradual increase of the length of the *active* cracks will be observed; the number of *active* cracks decreases until the behaviour of a specimen is determined by a single macrocrack. The mechanism which is proposed, applies for both tensile and compressive loading (brittle field). Yet, the process will be considerably more unstable
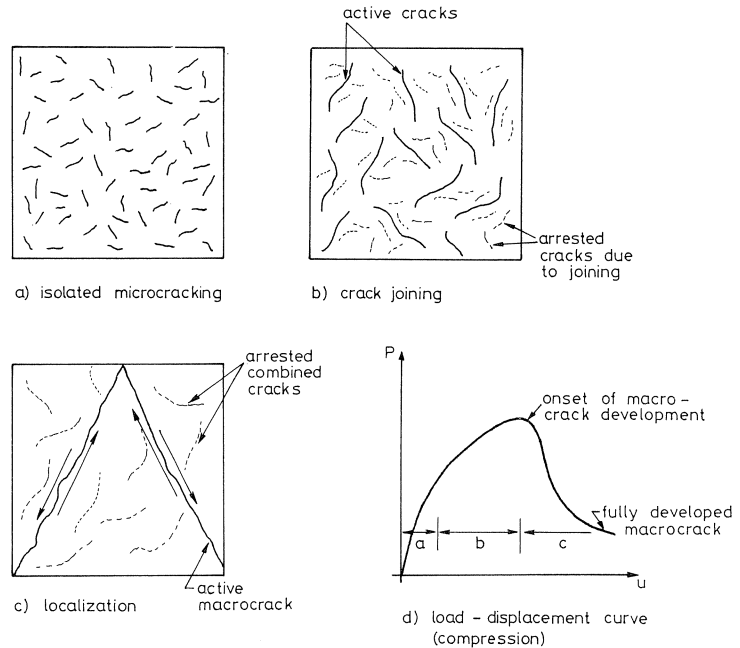
65

Fig. 2.7. Physical model for fracture propagation in concrete: isolated microcracking (Fig. a); crack joining (Fig. b); localization (Fig. c); load-displacement curve (Fig. d).

in direct tension (which is a special case of triaxial extension), while cracks will propagate in a very favourable direction.

More attention to the *structural behaviour of material experiments in the post-peak regime,* i.e. the development of the localization, is given in the next sections. An important aspect of the further discussion is the notion that the localized macroscopic fracture plane develops gradually through the specimen's cross-section while the overall load-displacement curve describes a descending branch. While the same mechanism is observed in tension and compression, emphasis is placed on the tensile loading case in the following discussion.

2.2 A Simple Softening Model

Fracture localization in a plate subjected to uniform tension

Consider a plate with length H, width W and thickness D, as shown in Fig. 2.8. The plate is double notched at half height as indicated, and is made of heterogeneous material: aggregates with a maximum size d_a (it is assumed that $d_a \ll D$) are embedded in a matrix with a significant lower stiffness.

Consider a slice of unit thickness $(D = 1)$, taken from the double notched plate of Fig. 2.8. The slice will intersect with numerous aggregate particles as indicated in Fig. 2.9.a. The aggregates are assumed to be circular inclusions, having the same diameter over the slice thickness. When external loading is applied, microcracks will develop in
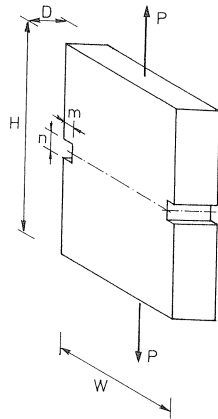
66

Fig. 2.8. Double notched direct tension test.

regions close to the notches, but will immediately be arrested in the steep stress-gradient near the notches, and due to the presence of tough aggregate particles. The results of Labuz 1985, and also those of Gopalaratnam & Shah 1985, as was shown in Fig. 2.6, indicate increased microcracking in notched specimens when compared to un-notched plates.

At sufficient high stress level, a macrocrack will start propagating from one of the notches (assume at point A in Fig. 2.9). The first growth of the crack occurs almost un-disturbed until a first aggregate particle is met. Due to this initial crack extension, the effective load carrying area decreases and a decrease of macroscopic stress will be observed (Fig. 2.9.b). The crack is arrested by the stiff aggregate, and when the bond between aggregate and matrix is still intact, the external load probably has to be in-creased again in order to extend the cracktip to point B (it is assumed that the crack pro-pagates along the interface, rather than through the aggregate). After point B is reached, a more or less spontaneous crackgrowth is possible until another stiffer region is rea-
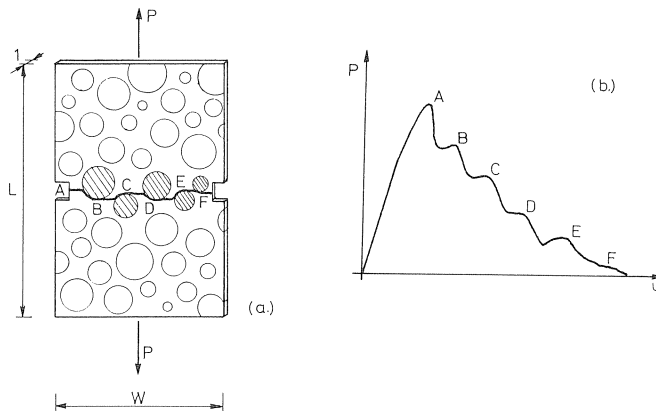

Fig. 2.9. Stable macrocrack propagation in a thin slice containing rigid disks: crackpath (Fig. a), and load-displacement curve (Fig. b).
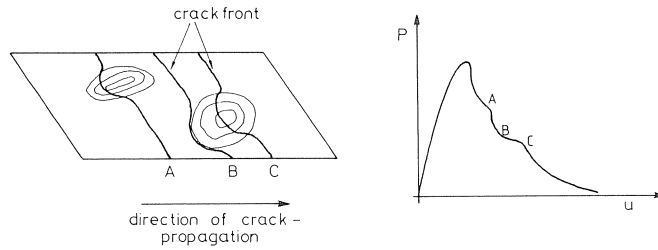
Fig. 2.10. Stable macrocrack growth in a specimen containing a few large rigid inclusions.

ched (aggregate C). Following this pattern, the crack will eventually reach the other side of the specimen. Occasionally crack growth will be accelerated due to the presence of microcracks along the macrocrack path, although recent research by Kachanov [1986], indicates that also shielding of the macrocrack may occur due to the presence of micro-cracks near the macrocrack tip. As a result of this shielding, delayed macrocrack growth will occur.

During crack propagation, the geometry of the specimen is considerably changed: the deformation field is non-uniform, and a "displacement gradient" will develop over the intact area. The load-displacement curve of the slice is not smooth in the descending branch (Fig. 2.9.b) as a direct result of the arresting effect of the larger aggregates. By averaging the effects of all slices a smooth descending branch will be found [as normally is observed in experiments, e.g. Gopalaratnam & Shah 1985, Labuz et al. 1985, Reinhardt 1984].

The rate of crackgrowth, or the displacement u needed to obtain a continuous crack obviously depends on the number and size of the aggregates. When many large aggre-gates are present, delayed crackgrowth occurs and the crackpath will become increas-ingly more tortuous. A few large aggregates in a homogeneous matrix will probably lead to a load-displacement curve as shown in Fig. 2.10. No increase of external load is needed to pass around an aggregate as was discussed before for the case of a thin slice. The crackfront is arrested only partially by a large aggregate particle, yet is allowed to propagate further in the surrounding matrix material. Only when the inclusion is very large compared to the total cross-sectional area of the specimen, a pronounced plateau may be observed in the overall load-displacement curve.
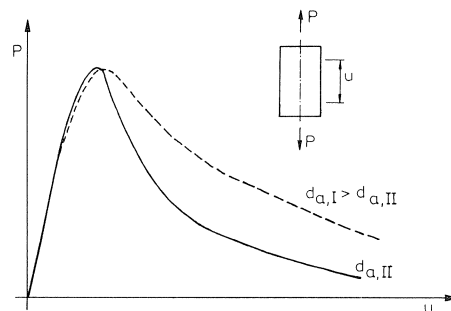

Fig. 2.11. Influence of the maximum aggregate size on the load-displacement curve in direct tension.

Experimentally, it has been shown that the aggregate size has a considerable influence on the slope of the descending branch of the load-displacement curve [Moavenzadeh & Kuguel 1969, Peterson 1981]. An increase of aggregate size, while maintaining a constant aggregate proportion by weight, results in a decreasing slope of the softening branch as shown in Fig. 2.11. Peterson reasoned that the increased tortuosity of the crackpath leads to a higher frictional resistance in a crack. In contrast the new physical model suggests that the increased post-peak ductility with increasing aggregate size may be the result of crack arrest mechanisms.

Linear elastic fracture mechanics

When in a double notched specimen a crack nucleates at one of the notches, a single notched specimen is created (Fig. 2.12). The second notch loses its importance immediately. Using LEFM, the stress intensity factor (SIF) for this *structure* can be determined. Assuming that the macrocrack starts propagating at peak-stress (i.e. $\sigma = \sigma_p$), and *that as a result of the pre-peak microcrack and joining processes an initial notch of size of $a_o/W = 0.05$ is formed,* leads to

$$K_{I,a_0} = 0.449\sigma_p\sqrt{W} \tag{2.6}$$

where the expression for K_I is taken from Broek 1982. It is of no use taking a more accurate value for K_I; the initial notch size is chosen rather arbitrary and will influence the result considerably.

When the size of the crack increases to $a_1/W > 0.05$, the stress intensity factor changes into

$$K_{I,a_1} = Y \cdot \sigma_1 \cdot \sqrt{\frac{a_1}{W}}\sqrt{W} \tag{2.7}$$

Dividing eq. (2.7) by eq. (2.6) yields

$$\frac{K_{I,a_1}}{K_{I,a_0}} = \frac{Y \cdot \sigma_1 \cdot \sqrt{\dfrac{a_1}{W}}\sqrt{W}}{0.449 \cdot \sigma_p \sqrt{W}} \tag{2.8}$$
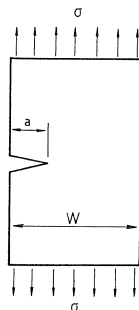
$$K_I = [1.99 - 0.41(\tfrac{a}{W}) + 18.7(\tfrac{a}{W})^2 - 38.48(\tfrac{a}{W})^3 + 53.85(\tfrac{a}{W})^4]\,\sigma\sqrt{a}$$

Fig. 2.12. Single notched direct tension test.

When it is assumed that *during macrocrack growth* K_{I,a_0} is a material constant, i.e. $K_{I,a_0} = K_I^*$, eq. (2.8) can be written as,

$$\frac{\sigma_1}{\sigma_p} = 0.449 / (Y \sqrt{\frac{a_1}{W}}) \qquad (2.9)$$

For an element with increasing cracklength a_1, the decrease of load carrying capacity can be calculated by using eq. (2.9). A decrease of stress is observed when the macrocrack propagates through the specimen's cross-section, as shown in Fig. 2.13. The use of the expression for the SIF becomes debatable for values of a/W close to 1. However for the present analysis this is no objection, other uncertainties remain such as the size of the initial notch at macrocrack nucleation.

It should be mentioned that K_I^* is not similar to the critical stress intensity factor $K_{I,c}$. The value of K_I^* depends on the actual pre-peak microcracking and joining mechanisms in a certain specimen configuration, i.e. the pre-peak microcrack processes determine when a specimen becomes notch sensitive. Also, in view of the discussion in the previous sections, it is quite likely that the size of the initial notch depends on the degree of heterogeneity of the specimen. It is postulated that size-effects in material experiments should be explained from a rigorous micromechanics analysis, taking into account geometrical probabilistic effects, for different specimen geometries and subjected to different loading combinations.

Having obtained this result, a translation from a $\sigma - (a/W)$ to a $\sigma - u$ (crack width) diagram should be made. Using the results of Labuz et al. 1985, and of Gopalaratnam & Shah 1985 (who both used the double notched plates), and results by Peterson 1981 (who used a slightly different specimen geometry), an $(a/W) - u$ relation was determined. This was simply done by comparing the stress decrease in a computed $\sigma - (a/W)$ diagram for a given (a/W), with the corresponding stress decrease in an experimentally observed $\sigma - u$ diagram.

The results are gathered in Fig. 2.14. In all cases an almost linear relationship between a/W and u is found. Deviations appear for larger values of a/W, when the application for the expression of K_I becomes debatable. If the aggregate size increases, i.e. when D/d_a
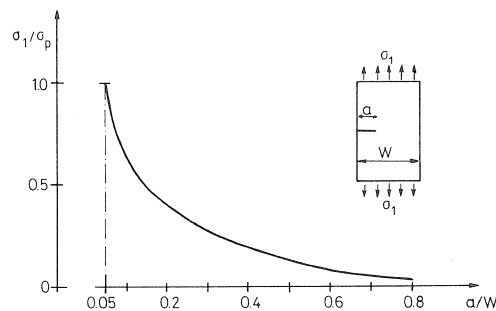

Fig. 2.13. Decrease of load carrying capacity with increasing notch-size in a single notched specimen subjected to direct tension.

70

fig. a.

	d_a [mm]	D/d_a	
x	2	10	PETERSON
+	8	2.5	1981
□	–	>20	GOPALARATNAM
△	5	4	and SHAH
⊙	10	2	1985

fig. b.

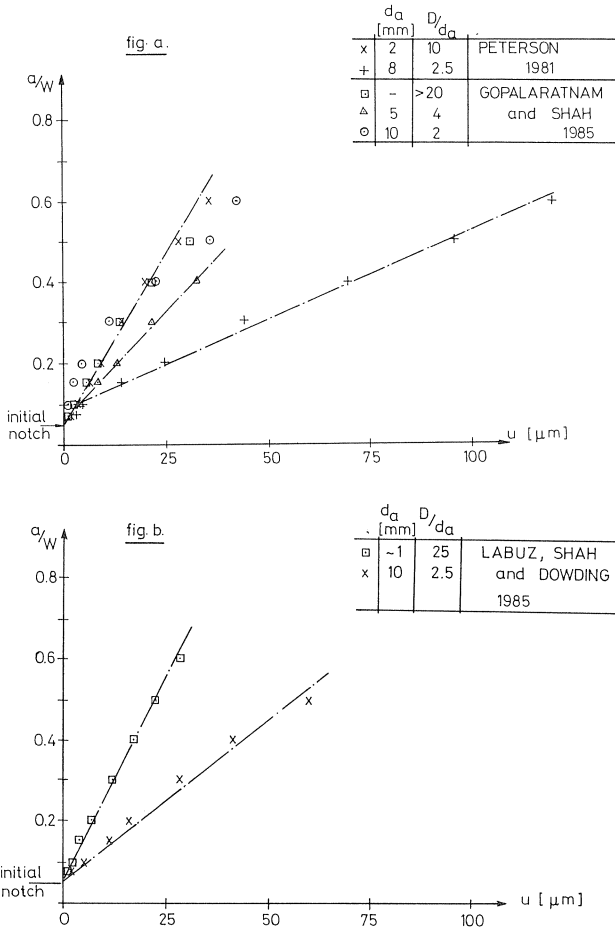|	d_a [mm]	D/d_a	
□	~1	25	LABUZ, SHAH
x	10	2.5	and DOWDING
			1985

Fig. 2.14. Crack width – crack length relationships for direct tension: concrete, mortar and cement paste (Fig. a); charcoal and rockville granite (Fig. b).

decreases, the slope of the $(a/W) - u$ relationship decreases, indicating a more pronounced effect of crack arrest mechanisms. On the other hand, homogeneous materials (i.e. with high values of D/d_a, such as for example the cementpaste tested by Gopalaratnam & Shah or the charcoal granite tested by Labuz et al.), will have an $(a/W) - u$ relationship which is almost parallel to the (a/W) axes, indicating almost pure brittle behaviour. If the size of a specimen of homogeneous material is reduced, the degree of heterogeneity increases, and likely a stable post-peak response can be measured. In fact one might suspect that even for metals a stable post-peak relation can be measured if the specimensize is sufficiently reduced.

The results by Gopalaratnam and Shah for concrete with crushed limestone aggregates of size $d_a = 10$mm, are close to their results for cement paste. This may be explained from the fact that the stiffness of the limestone is not very different from the stiffness of

71

the matrix material, therefore allowing the macrocrack to penetrate into the aggregates [see also Peterson 1981]. The mechanism of Fig. 2.9 does not apply in this case, and the material will act as a rather homogeneous solid.

Experiments on double notched plates also were carried out by Reinhardt 1984, and Cornelissen et al. 1986. The boundary conditions in these experiments (uniform boundary displacement, special attention was given to avoid rotation of the loading platens) were different from those in the experiments carried out by Labuz 1985, and by Gopalaratnam & Shah 1985. The geometrical factor Y in eq. (2.7) depends on the boundary conditions [Cartwright 1979], which implies that eq. (2.7) does not apply for the latter experiments. In the following section some results of a numerical simulation of a direct tension test with non-rotating end-platens will be discussed.

From the above results it may be concluded that, for the case of a direct tension test on a double notched plate, LEFM is applicable in combination with a linear crack length-crack opening relationship. The shape of the softening branch is explained by this relatively simple model, and post-peak ductility is shown to be dependent on the degree of heterogeneity of the specimen.

The same method should be tested for crack propagation through specimens with different shapes and geometries. Furthermore, research is needed in order to determine the influence of aggregate size, shape and stiffness on the post-peak ductility for different structures.

2.3   *Numerical simulation of a direct tension test*

In section 2.1, the outline of a theoretical approach for analyzing the structural response of a macroscopic material experiment was discussed. In the pre-peak region, a continuum solution still seems to be in agreement with the physical observations, yet in the post-peak region when the influence of boundary conditions becomes very pronounced and deformations are confined to narrow regions, the use of a continuum solution is rather debatable. These theoretical considerations culminated in a simple linear elastic fracture mechanics solution for describing the post-peak behaviour observed in a direct tension test on a double notched plate, and indicated that geometrical factors may be more important than assumed in previous models. Consequently, this solution, with a simple relationship between crack opening and crack length, and taking into account the degree of heterogeneity of the specimen, only can be used for describing the response of the double notched test under certain boundary conditions. Describing the behaviour of different specimens (geometries) with the same model is not possible. If such a solution would apply to other structures too, this seems merely a matter of chance. In fact it is believed that from the material experiments a "lower level" material model should be derived, which can be used for analyzing different structures. Such a material model also should be capable of explaining the behaviour as observed in the common macroscopic material experiments. This implies that the influence of the experimental set-up should be eliminated as much as possible, and a possible solution to this problem

may be derived from carrying out experiments with different boundary conditions, and comparing the results. Another aproach may be to simulate the material experiment numerically. In such an approach, the boundary conditions should be taken into account as realistically as possible.

In this section some preliminary results of a numerical simulation of a material experiment are shown. The double notched direct tension test is chosen, mainly because of the simplicity of the structure, but also while it is an interesting extension to the previous section. For the numerical simulation, the program DIANA [De Borst, Kusters, Nauta & De Witte, 1983] has been used with the standard available smeared crack model [Rots et al. 1985]. In this chapter, main emphasis lies on understanding the structural behaviour of the direct tension test, no attempt has been made to improve the available "material models". Instead, a simple parameter study has been carried out from which some interesting conclusions can be drawn.

Smeared crack model

In the current analyses, the smeared crack model, as developed by Rots et.al. [1985], and which is available in the standard version of the DIANA program has been used. Basically this crack-model consists of a 2×2 crackmatrix of which only the diagonal terms are non-zero. The first diagonal term describes the relationship between the crack-stress and the crack-strain normal to the crack plane. The crack is smeared over a band with width h, in a way similar to the model proposed by Bažant & Oh [1983]. The second diagonal term describes the shear stiffness of the crack via a constant shear-retention factor η.

In the standard crack-model, various shapes of the softening branch can be adopted [see Rots 1985], but in the current analyses, only the linear variant has been applied. In this case the ultimate strain in the tensile softening diagram is determined following,

$$\varepsilon_u = 2 \frac{G_f}{f_t \cdot h}$$

(2.10)

For details of the crack model, the reader is refered to Rots et al. [1985], and Rots [1985]. In these publications it was shown that localization of cracking can be simulated with the smeared crack model, which aspect makes is useful for the current analyses as well.

Description of the problem

Important in the previous discussion has been the notion that the deformation distribution in the specimen is non-uniform in the softening branch. This was shown experimentally for the case of uni- and triaxial compression in part 1. Results reported recently by Reinhardt 1984, Cornelissen et al. 1986 and Labuz et al. 1985, indicate that non-uniform deformations also occur in the softening branch measured in direct tension experiments on double notched plates of concrete or rock.

In the numerical simulations, the geometry of the plates as tested by Labuz et al. 1985 has been adopted. These plates of size 280 x 75 mm^2, and thickness 13 mm, were double notched at half height. The element discretization is shown in Fig. 2.15. Eight noded isoparametric elements, numerically integrated by means of a nine point Gaussian scheme, were used. The mesh was refined in the region with the notches. The transition from the coarse to the fine mesh was done by using numerically integrated [three point Gaussian scheme] six noded triangular isoparametric elements. The boundary conditions were such that the far edges of the plate displaced parallel to each other. This is a deviation from the assumptions made in section 2.2, and does not resemble the boundary conditions of the experiments of Labuz et.al., but rather those adopted in the tensile experiments (on 100 mm cubes), which were part of the triaxial series (see section 1.1). Also in the experiments carried out by Reinhardt [1984], and Cornelissen et al. [1986], the same boundary conditions were used.

The material properties were largely varied. Basically a tensile strength of $f_t = 3.0$ N/ mm^2 was used, which corresponds to the macroscopic tensile strength measured in the experiments that were reported in part 1. Experience of Rots et al. shows that the crack localized in a band extending over two rows of Gauss-points, and consequently $h = 5/3$ mm in the current analyses. The shear-retention factor was constant and equal to 0.20. In the analyses, the value of G_f was varried substantially, ranging from very low
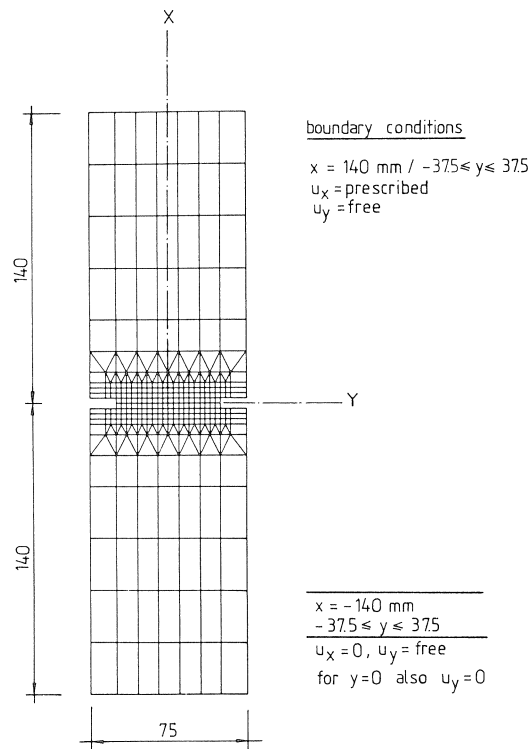

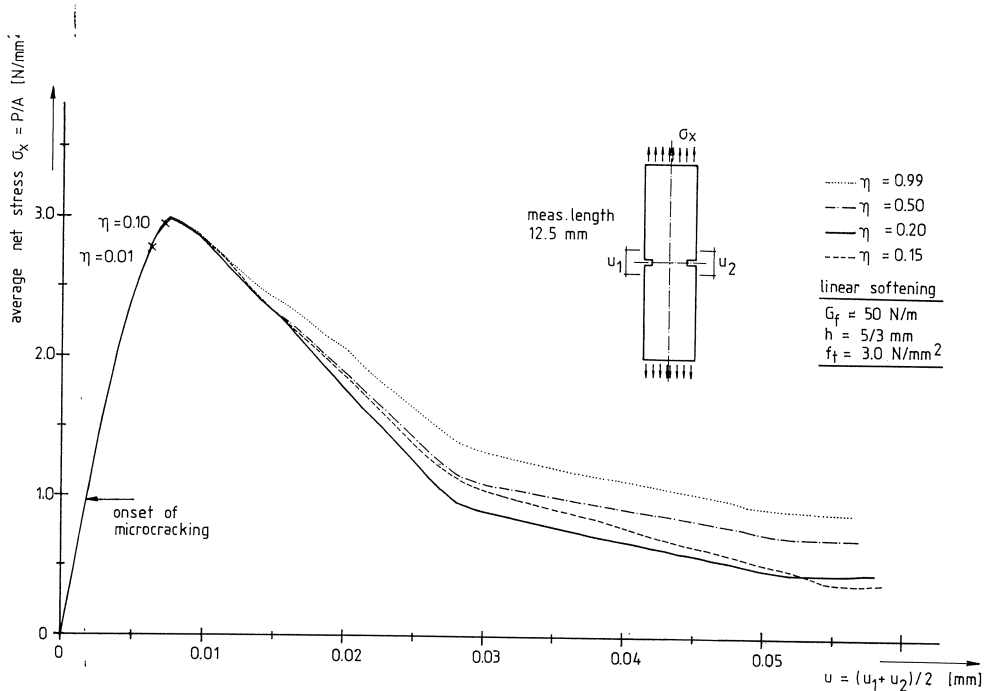Fig. 2.15.   Element discretization and boundary conditions.

average net stress $\sigma_x = P/A$ [N/mm²]

σ_x

meas. length
12.5 mm

u_1 ⊣⊢ u_2

η = 0.99
η = 0.50
η = 0.20
η = 0.15

linear softening

$G_f = 50$ N/m
$h = 5/3$ mm
$f_t = 3.0$ N/mm²

3.0

η = 0.10
η = 0.01

2.0

1.0

onset of
microcracking

0

0   0.01   0.02   0.03   0.04   0.05

$u = (u_1 + u_2)/2$ [mm]

Fig. 2.16. Computed load-displacement curves for a direct tension test, $G_f = 50$ N/m, $f_t = 3$ N/mm², and various values of the shear retention factor η.

values (3.75 − 10 N/m) to normally accepted values for concrete (50 − 100 N/m). By decreasing the tensile strength of four elements (effective length 10 mm) near the left notch, non-symmetrical cracking of the plate, as observed in direct tension tests, is simulated. It is not a necessary condition that the perturbation should be situated near one of the notches. This seems however the most likely place for crack initiation.

Computational results

In a first analysis, the now widely accepted G_f-criterion was used, which was first proposed for concrete by Hillerborg and co-workers [1976], and $G_f = 50$ N/m. In figure 2.16, the computed load-displacement diagram is shown. The displacement is the average of the displacements $u_{x,1}$ and $u_{x,2}$, which were calculated from the relative displacements of two points at mutual distance of 12.5 mm at each side of the plate near the notches (see inset of Fig. 2.16). A fast converging solution was obtained by using the modified Newton Raphson itterative scheme. The computations yielded the expected results. The calculated macroscopic stress is almost equal to the, what we shall refer to as local tensile strength of the material. A variation of the shear-retention factor η, yielded almost similar results as published before by Rots et al. [1985]. When very low values of η were used, the analysis diverged already in the pre-peak region, and no descending branch could be obtained. Note that due to local tensile stress concentrations near the notches, cracking starts at relatively low levels of average stress (indicated with an arrow in Fig.

75

2.16). When η exceeded the value of 0.2, an increaasingly more stable solution was obtained, and as can be seen from Fig. 2.16, the ductility in the post-peak region increased. The computed horizontal branch after the steep part of the descending branch seems to be a direct implication of the crack model. The effects of both diagonal terms in the crack matrix interact, and obviously the contributions cancel.

In spite of the reduced tensile strength of the four elements near the left notch (the local tensile strength was reduced to 2.9 N/mm²), "microcracking" first proceeded over the entire cross-section of the specimen, whereafter all cracks started to open gradually, and a stable softening branch was computed. The cross-section was completely cracked near the peak stress level in the stress-displacement diagram. The "crack strain" of these cracks was however well beyond ε_u. This result is of course no surprise in view of the adopted continuum softening model, which was derived under the assumption that in the softening region deformations are confined to an uniformly and gradually opening narrow band. The localization is confined to a band-width of 2 Gauss points, which confirms the results obtained by Rots et al. [1985]. Obviously the perturbations (viz. the four elements with reduced tensile strength near the left notch) were not large enough for triggering macrocrack propagation from the left notch. Some variations were tried, for example by choosing a different shape of the softening branch, but these were not successful for triggering non-symmetric macrocracking.

In Fig. 2.17, the influence of G_f on the load-displacement behaviour is shown. In these analyses, where G_f was varied between 10 and 100 N/m, the local tensile strength was somewhat higher than in the previous analyses, viz. $f_t = 4.5$ N/mm². The local tensile strength of the four elements near the left notch was equal to $f_t = 4.35$/mm². The impact of the G_f-concept on the computational result is very clear from this figure. For low values of G_f (i.e. $< 50 - 75$ N/m), the numerical analysis was rather unstable in the softening region. The analyses converged very slowly, and the norm energy was not reached in several load-steps. This could not be circumvented by decreasing the size of the load-steps. For the cases with $G_f = 10,25$ and 50 N/m, the softening branches were almost parallel to one another, and only the "peak-stress" level was increased by increasing G_f. Macrocrack growth occured identical in the analysis with low G_f, and the descending branch seems to be a direct consequence of the decrease of effective load-carrying area (compare with the LEFM solution presented in section 2.2).

Only by further increasing G_f, the slope of the softening branch was influenced. Obviously, by choosing the value of G_f too low, the average stress of the specimen is underestimated, or with different words, the influence of the pre-peak microcracking stage is underestimated. Obviously, quite a large part of the energy, needed to fracture the specimen is required for this microcracking process, and by decreasing G_f, we come more and more close to the classical strength criterion, which, as shown by Bažant [1986], does not yield the correct size-effect. Obviously, but this is also the basic assumption in the process-zone model, pre-peak cracking is modelled by estimating the extra energy requirement due to stable microcracking in the ascending branch, from the softening response measured in a direct tension test. However, as already pointed out in section 2.1, the physical processes are completely different in the pre- and post-
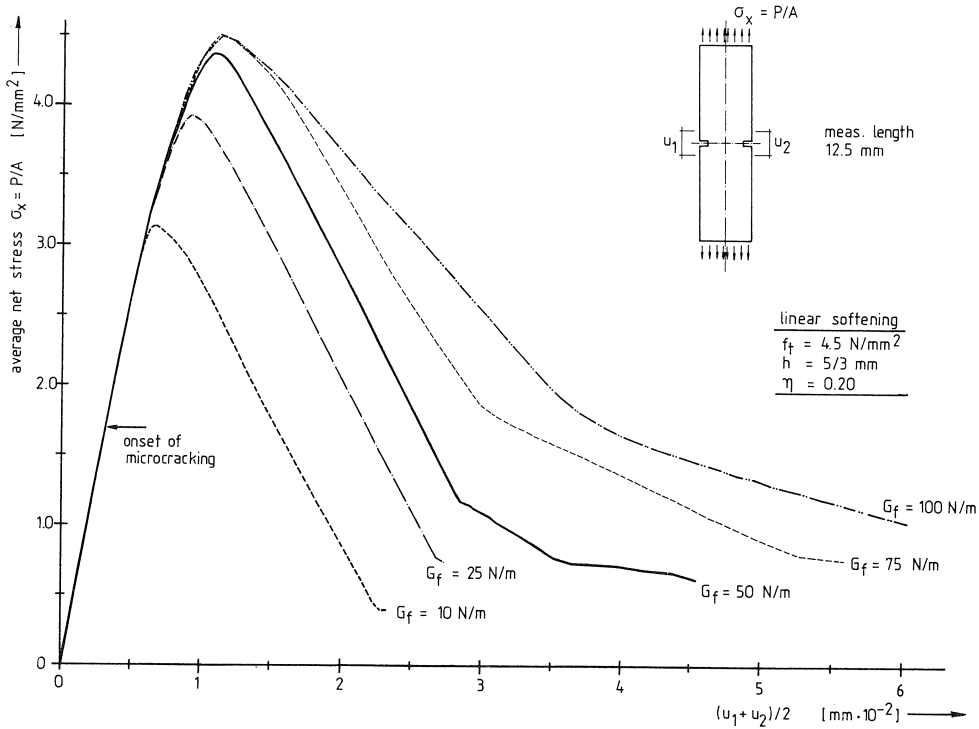
76

Fig. 2.17. Influence of the fracture energy parameter G_f on the load-displacement diagram in direct tension.

peak regions, and for several reasons still to be mentioned, the process-zone model seems physically unacceptable.

The computations with high G_f (i.e. > 50 N/m), showed a gradual opening crack band over the complete cross-section of the specimen. However, in the other computations with low G_f, macrocracking started at the left notch, and then gradually propagated through the specimen's cross-section, which is in agreement with experimental observations [i.e. Reinhardt 1984, Cornelissen et al. 1986, Labuz et al. 1985]. When the local deformations are plotted, as done in Fig. 2.18 for the analysis with $G_f = 10$ N/m, large deformations $(u_{x,1})$ are first measured at the left side of the plate, and much later, about half-way of the descending branch, at the other side of the specimen $(u_{x,2})$. At several stages in the descending branch the length of the macroscopic crack (with "cracks-strains" exceeding ε_u, which in this analysis was equal to .002667), is indicated. The result shows a similar tendency as found in Labuz's experiments (Fig. 2.5). Note however that the boundary conditions in this analysis, and in the experiments carried out by Labuz are different. In the following section, attention is paid to the effect of the boundary conditions on the crack-mechanism.

The results, discussed above, strongly suggest that, as far as the physics of the fracture process are concerned, the G_f model is a too large simplification. Both the experimental
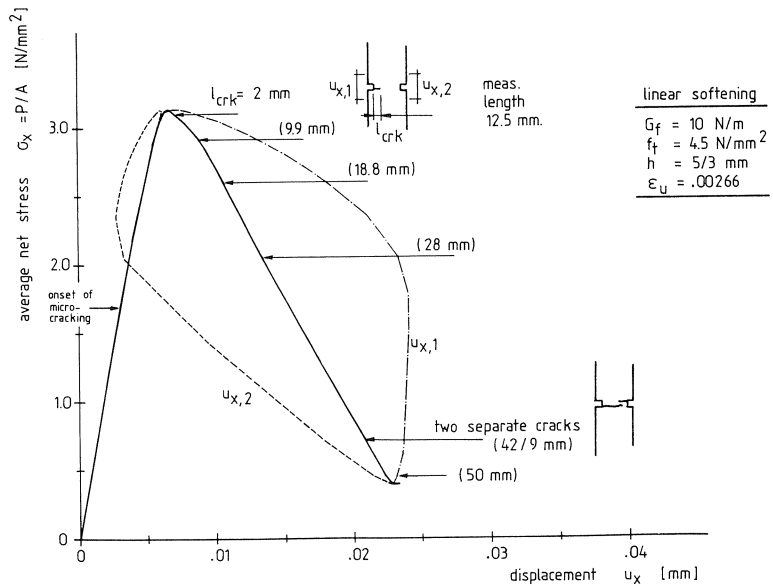
77

average net stress $\sigma_x = P/A$ [N/mm^2]

3.0

2.0

1.0

0

$l_{crk}= 2$ mm

(9.9 mm)

(18.8 mm)

(28 mm)

onset of micro-cracking

$u_{x,1}$

$u_{x,2}$

$u_{x,1}$

$u_{x,2}$

meas. length 12.5 mm.

l_{crk}

linear softening

G_f = 10 N/m
f_t = 4.5 N/mm^2
h = 5/3 mm
ε_u = .00266

two separate cracks (42/9 mm)

(50 mm)

0   .01   .02   .03   .04

displacement u_x [mm]

Fig. 2.18. Computed load-displacement diagrams for a direct tension test ($G_f = 10$ N/m, $f_t = 4.5$ N/mm^2, and $\eta = 0.20$).

results of part 1, and the theoretical considerations, strongly suggest that the microcrack processes and the development of the macroscopic fracture plane should be treated separately. Although the nucleation of the macrocrack is dependent of the pre-peak microcrack processes, its growth seems not influenced by these processes. It seems physically contradictionary to use the "stress-profile" measured in the softening region in a direct tension test, for estimating the energy requirement due to pre-peak microcrack processes of similar specimens, but with different geometries and loadings (such as for example beams subjected to bending).

Crack mechanism

As mentioned before, non-symmetric cracking only could be simulated when low values of G_f were used in the analyses. For high values of G_f, microcracking first spreaded over the complete cross-section of the specimen, which can be explained from the large size of the "fracture process-zone". It should be mentioned that non-symmetric macrocracking was not observed in the analyses with low G_f when the variations in local tensile strength were too small. This may suggest, that non-uniform cracking of the specimens is induced by local material variations. Taking into account statistical variations of material properties seems inevitable when fracture experiments are to be interpreted.

An analysis with low G_f, and low local tensile strength was carried out as well. In this case, as expected, the average (specimen) stress decreased to approximately 2 N/mm^2.

In Fig. 2.19, the incremental deformations at four stages in the analysis are shown. The macrocrack (with "crack strains" exceeding ε_u) initiated near the peak-stress level, and then propagated through the specimen's cross-section. Initially large incremental deformations occured at the left side of the plate only. Eventually however, the incremental deformations also occured at the other side, and the specimen showed local "waggling". As mentioned, the loading platens were kept parallel to each other in the analysis (only the upper platen also could move horizontally), which corresponds to the boundary conditions as adopted in the experiments carried out at Delft University of Technology [Reinhardt 1984, Cornelissen et al. 1986]. Only in these experiments, lateral deformations of the upper loading platen were not allowed (see Fig. 2.15), but an
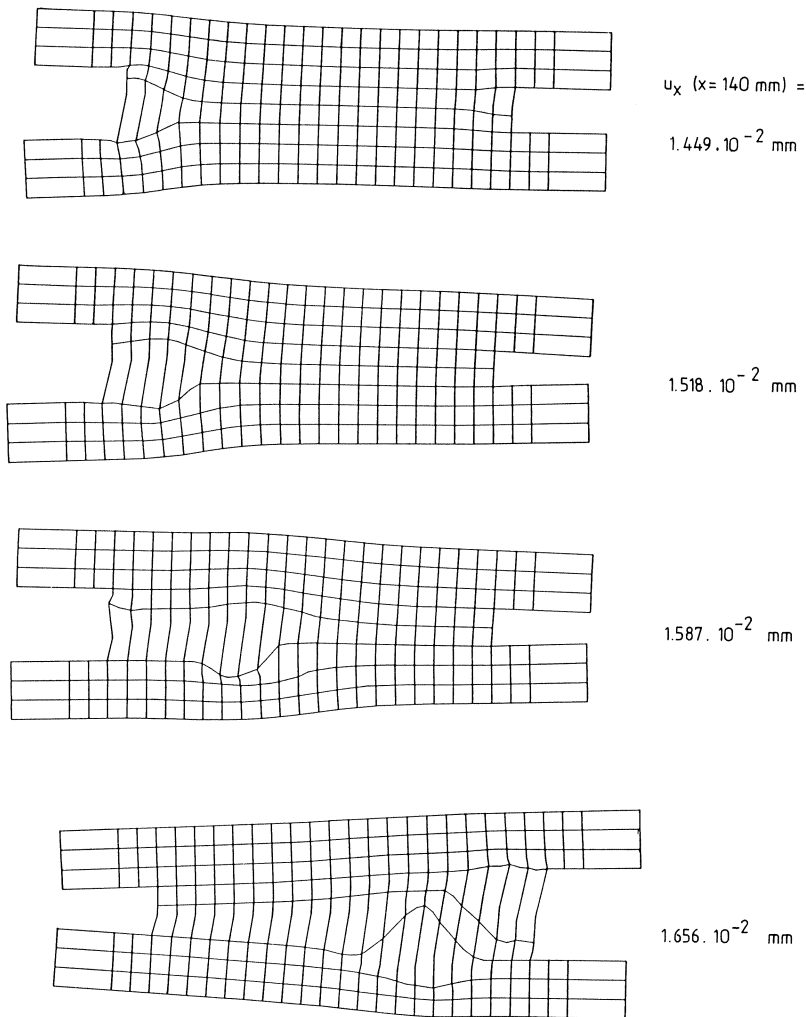
u_x (x = 140 mm) =

$1.449 . 10^{-2}$ mm

$1.518 . 10^{-2}$ mm

$1.587 . 10^{-2}$ mm

$1.656 . 10^{-2}$ mm

Fig. 2.19. Incremental deformations, case $G_f = 3.75$ N/m, $f_t = 3.0$ N/mm², and $\eta = 0.20$. Local "waggling" occurs due to non-symmetric cracking of the plate.

79

additional analysis indicated that the behaviour of the specimen hardly changed when the upper part could not move in the lateral direction. Close scrutiny of the results of the Delft group suggests that local "waggling" also occurs in their experiments [e.g. see the post-peak displacement distributions over the plate in Fig. 16 in Reinhardt 1984]. The displacement jump in this figure (from step 11–14) is accompanied by a characteristic plateau in the softening branch, similar as observed in some of the uniaxial tensile experiments which accompanied the triaxial series (see part 1, and Fig. A2 in the appendix). As a matter of fact a non-uniform distribution of deformations was measured in the latter tensile experiments as well. The current computational results suggest that local variations in material properties may be responsible for the effect, and not excentricities in the experimental set-up as previously assumed. The other result shown in the appendix indicates a more uniform loading, but here of course we may have missed the "waggling". The cubical specimens may show triaxial effects in the sense that local rotations may occur along the other diagonal as the one over which the LVDTs were placed. The "waggling" remains then largely undetected. This may also explain why in the experiments of the Delft group not always the characteristic plateau was observed.

The boundary conditions in Labuz's experiments were different, and rotation of the loading platens was allowed. Under these conditions no local "waggling" can occur: the macrocrack simply nucleates at one of the notches, and propagates gradually towards the other side of the specimen.

In the analysis the characteristic plateau in the softening branch was not found. However, it should be mentioned that the loading (i.e. displacement increment) was applied to the plate at the upper edge. In fact the conditions in the experiment, where usually the average displacement measured with two LVDTs (one at each side of the plate) is
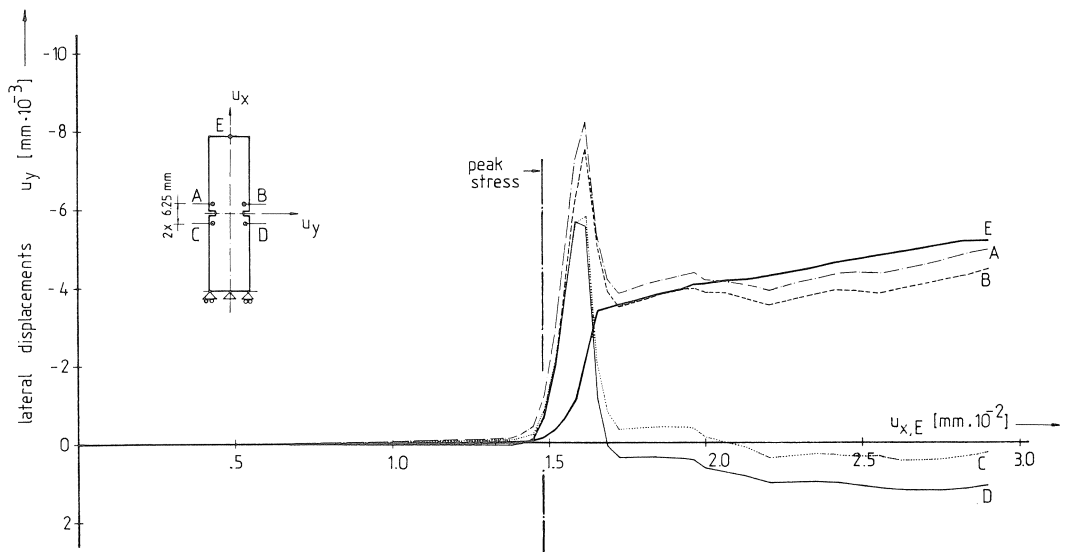

Fig. 2.20. Computed lateral displacement in a direct tension test in which non-symmetric cracking occurs ($G_f = 3.75$ N/m, $f_t = 3.0$ N/mm², and $\eta = 0.20$).

80

used for test-control, should be followed more closely. Probably, then also the convergence will improve [De Borst 1986]. Note that several factors may become important during macrocrack growth such as rate-effects and local unloading. The response of the tensile specimen can only then be simulated successfully if these aspects are included realistically in the model.

As a final result, in Fig. 2.20, the lateral deformations as computed in the latter analysis ($G_f = 3.75$ N/m, and $f_t = 3$ N/mm^2) are shown. The local "waggling" in the post-peak region is accompanied by lateral displacements, and as can be seen from Fig. 2.20, the complete upper part of the specimen has a remaining lateral displacement (compare the lateral displacements of nodes A, B and E, with those of nodes C and D). The lateral displacements were less pronounced in the computations with a high G_f. Lateral displacements also were measured by Cornelissen et al. [1986].

2.4 Concluding remarks

In the previous sections, the principal outline of a physical model for describing the fracture process of plain concrete and similar heterogeneous materials was described. The theoretical considerations, both the analytical fracture mechanics solution for macrocrack propagation in a direct tension test, as well as the numerical simulation of a similar problem, and the experimental results presented in part 1, strongly support the hypothesis that pre-peak microcracking and the development of the macroscopic fracture plane should be treated separately. Consequently, the application of fracture process-zone models, in which basically the pre-peak microcrack process is modelled by applying a "stress-closing profile" derived from the softening branch measured in a direct tension experiment, seems physically unacceptable. The fact that in bending the process-zone model yields proper results seems merely a matter of change. As shown in the previous sections, deformation distributions become highly non-uniform in a direct tension test as soon as the descending branch is reached. Under certain conditions the macrocrack propagates through the tensile specimen under the simultaneous development of a stress- and deformation gradient, similar to the gradient observed in bending. The notion that stress and strain are non-uniformly distributed in the softening region in uniaxial and multiaxial compression experiments (with the restriction that brittle failure occurs), has been known for some time now [e.g. see Read & Hegemier 1984, Hegemier & Read 1985 and Van Mier 1984a, b), and as shown in this paper, should be extended to uniaxial tension.

The behaviour of a double notched tensile specimen can also be simulated when the local tensile strength of the material is increased and when simultaneously the fracture energy (or process-zone size) is reduced considerably. The notion of a higher local strength than the macroscopically determined "specimen" strength is not new [e.g. Grudemo 1979]. In fact, the softening phenomenon is explained from the constantly changing specimen geometry, and the arresting effect of large aggregates along the

macrocrack path is simulated with the small process zone. Recent research by Tait & Garret [1986], indicates that the process zone may indeed be considerably smaller than previously assumed. This latter approach is however only a very rough approximation, and on a lower size level the crackpath will be rather tortuous. Consequently, the direct tension test on a plate of heterogeneous material should be treated as a mixed mode problem. Pure mode I cracking is possible in a plate of homogeneous material only.

It seems logical that the response of the material becomes more linear as soon as the resolution of the model is increased. Decreasing the scale of the models implies that more simple material characterizations may be used. Locally the response of the constituents will become increasingly more simple. On the other hand, the basic question must be raised if the gain in simplifying the material models is not nullified by the increasingly complex material structure which must be taken into account. The problem might be solved by choosing a proper averaging technique.

The influence of the specimen's geometry and boundary conditions seems to be larger than previously suspected, and future efforts should be aimed at eliminating these influences as much as possible. It is questionable if "material properties" measured at the macroscopic level from specimens with given geometry and boundary conditions are transferable to different geometries and boundary conditions. Reducing the scale of the material model may be one solution to the problem. Here the point of view is supported that when "macroscopic material experiments" are understood in detail, and also when their response can be simulated accurately with a lower level material characterization, the chances that this material law will serve also under different boundary conditions and for different geometries becomes increasingly larger.

Conclusions

In addition to the concluding remarks made in sections 1.6 and 2.4, the following conclusions can be drawn:

1. Localized fracture modes are observed for all multiaxial loading combinations below the brittle-ductile transition. Differences in the loading combinations are manifested in different orientations and properties of the macroscopic fracture planes.

2. The brittle-ductile transition occurs at relatively low levels of confining stress for loading combinations resembling conventional triaxial compression (i.e. when two large tensile deformations can develop). For loading combinations leading to only one large tensile displacement (out of plane cracking or extension), the transition occurs at a much higher confinement level, and was not reached in the current investigation.

3. The macroscopic fracture plane develops non-uniformly through the specimen's cross-section while the overall load-displacement curve describes a descending branch.

4. The nucleation of the macroscopic fracture plane is dependent of the pre-peak

82

microcrack processes. However, as indicated by the rotation experiments, the growth of the macroscopic fracture plane through the specimen's cross-section must be considered as an independent process which is hardly affected by the presence of microcracks.

5. The notion of a fracture process zone for describing softening behaviour as observed in displacement controlled uniaxial and multiaxial tension and compression experiments seems not correct. The shape of the softening branch can be explained from the changing geometry of a specimen when the macroscopic fracture plane develops through the specimen's cross-section.

6. The physical explanation for delayed crackgrowth in heterogeneous materials is that at the sub-macroscopic level combined mode I and mode II cracking occurs. Increased ductility (in the softening region) in specimens containing large aggregates (with higher stiffness than the surrounding matrix), must be explained from the arresting effects of the aggregates, which enforce macroscopic crack growth along a tortuous path.

7. A three stage fracture process is proposed. A gradual transition from distributed microcracking (which can be modelled as a continuum), to discrete macrocracking (where geometrical influences and boundary conditions largely control the stability of the process), is modelled by a process refered to as crack joining. The details of the crack joining process need further research, as these are important for determining the conditions under which macroscopic fracture may proceed.

Notation

The following symbols are used in this paper:

A specimen cross-section $= D.W$
a semi-crack length
Δa semi-crack length increment
d_a maximum aggregate size
D specimen thickness
E modulus of elasticity
f_c uniaxial compressive strength
f_t uniaxial tensile strength
G_f fracture energy
h crack band width
H specimen height
K_I stress intensity factor, mode I
K_{Ic} critical stress intensity factor, mode I
K_I^* stress intensity factor during macrocrack growth
N number of cracks
p nominal stress $(= P/A)$
P external load
u_i total principal specimen displacements (i = 1,2,3)
u_i' total principal specimen/brush displacements (i = 1,2,3)
V_s specimen volume $(= D.W.H)$
W specimen width
ΔW_{Ic} energy released due to mode I crack extension
ΔW_{Ic}^j energy released due to mode I crack joining
Y geometrical factor
α σ_2/σ_1 or u'_2/u'_1
β σ_3/σ_1
ε_i principal strains (i = 1,2,3)
ε_u ultimate strain of the tensile strain-softening diagram
η shear retention factor
φ shear band inclination with respect to the major principal stress
σ_i principal stress (i = 1,2,3)
v poisson's ratio

References

AHMAD, S. H. and S. P. SHAH (1982), Complete Triaxial Stress-Strain Curves For Concrete, J. Struct. Div., ASCE, 108(4), 728–742

ANDENAES, E., K. H. GERSTLE and H. Y. KO (1977), Response of Mortar and Concrete to Biaxial Compression, J. Eng. Mech. Div., ASCE, 103(4), 515–526.

ATTIOGBE, E. K. and D. DARWIN (1985), Submicroscopic Cracking of Cement Paste and Mortar in Compression, Structural Engineering and Engineering Materials Report no. 16, University of Kansas, Lawrence, Kansas.

BAŽANT, Z. P. and L. PANULA (1978), Statistical Stability Effects in Concrete Failure, J. Eng. Mech. Div., ASCE, 104(5), 1195–1212.

BAŽANT, Z. P. (1983), Comment on Orthotropic Models for Concrete and Geomaterials, J. Eng. Mech., ASCE., 109(3), 849–865.

BAŽANT, Z. P. (1986), Mechanics of Distributed Cracking, Appl. Mech. Rev., 39(5), 675–705.

BERTACCHI, P. and R. BELLOTTI (1972), Experimental Research on Deformation and Failure of Concrete under Triaxial Loads, in Proceedings RILEM Symposium on The Deformation and the Rupture of Solids Subjected to Multiaxial Stress, paper I/3, 37–52.

BAŽANT, Z. P. (1986), Mechanics of Distributed Cracking, Appl. Mech. Rev., 39(5), 675–705.

BERTACCHI, P. and R. BELLOTTI (1972), Experimental Research on Deformation and Failure of Concrete under Triaxial Loads, in Proceedings RILEM Symposium on The Deformation and the Rupture of Solids Subjected to Multiaxial Stress, paper 1/3, 37–52.

BIENIAWSKI, Z. I. (1967), Mechanism of Brittle Fracture of Rock, Part I, II and III, Int. J. Rock. Mech. Min. Sci., 4, 395–430.

BRODSY, N. S. (1985), An Investigation of the Fracture of Granite under Triaxial Stress, PhD dissertation, University of Colorado, Boulder, Dept. of Geological Sciences.

BROEK, D. (1982), Elementary Engineering Fracture Mechanics, Martinus Nijhoff Publishers, 3rd revised edition.

BUYUKOZTURK, O. and J. G. ZISMAN (1982), Behavior of Concrete in Biaxial Cyclic Compression, Report, Massachussets Institute of Technology, pp. 39.

CARRASQUILLO, R. L., F. O. SLATE and A. H. NILSON (1981), Micro-cracking and Behavior of High Strength Concrete Subject to Short Term Loading, ACI Journal, 78(3), 179–186.

CARTWRIGHT, D. J. (1979), Stress Intensity Factor Determination, in Developments in Fracture Mechanics -1, ed. G. G. Chell, Applied Science Publishers ltd., 29–66.

CHEN, W. F. (1982), Plasticity in Reinforced Concrete, McGraw Hill, New York.

COCHRAN, W. G. and G. M. COX (1957), Experimental Designs, John Wiley & Sons inc., New York, 2nd edition.

CORNELISSEN, H. A. W., D. A. HORDIJK and H. W. REINHARDT (1986), Experimental Determination of Crack Softening Characteristics of Normalweight and Lightweight Concrete, in Fracture Mechanics and Structural Aspects of Concrete HERON, 31(2).

COSTIN, L. S. (1983), A Microcrack Model for the Deformation and Failure of Brittle Rock, J. Geophys. Res., 88, 9485–9492.

COSTIN, L. S. and C. M. STONE (1986), Analysis of Triaxial Testing using a Fracture Damage Model, Proc. Soc. Expt. Mech. Spring Conference, New Orleans, LA, June 8–13.

DE BORST, R., G. M. A. KUSTERS, P. NAUTA and F. C. DE WITTE (1983), DIANA – A Comprehensive but Flexible Finite Element System, Finite Element Systems Handbook, 3rd edition, Springer Verlag, Berlin, Germany.

DE BORST, R. (1986), Non-Linear Analysis of Frictional Materials, PhD Dissertation, Delft University of Technology, Delft, The Netherlands.

DIAMOND, S. and A. BENTUR (1984), On the Cracking in Concrete and Fiber Reinforced Cements, in Application of Fracture Mechanics to Cementitious Composites, NATO-ARW, Northwestern University, ed. S. P. Shah, 51–139.

DOUGILL, J. W. (1976), On Stable Progressively Fracturing Solids, ZAMP, 27(4), 423–437.

FREUDENTHAL, A. M. (1950), The Inelastic Behaviour of Engineering Materials and Structures John Wiley and Sons, Inc., New York, NY.

GERSTLE, K. H. et al. (1978), Strength of Concrete under Multiaxial Stress-States, in Douglas McHenry International Symposium on Concrete and Concrete Structures, American Concrete Institute Publication SP55-5, 103–131.

GERSTLE, K. H. et al. (1980), Behaviour of Concrete under Multiaxial Stress-States, J. Eng. Mech. Div., ASCE, 106(6), 1383–1403.

GLÜCKLICH, J. (1983), Fracture of Plain Concrete, J. Eng. Mech. Div., ASCE, 89(6), 127–138.

GOPALARATNAM, V. S. and S. P. SHAH (1985), Softening Response of Plain Concrete in Direct Tension, ACI Journal, 82(3), 310–323.

GRUDEMO, A. (1979), Microcracks, Fracture Mechanism, and Strength of the Cement Paste Matrix, Cement & Concrete Research, 9(1), 19–34.

HALLBAUER, D. K., H. WAGNER and N. G. W. COOK (1973), Some Observations Concerning the Microscopic and Mechanical Behaviour of Quartzite Specimens in Stiff, Triaxial Compression Tests, Int. J. Rock Mech. Min. Sci. & Geomech. Abstr., 10, 713–726.

HAN, D. J. and W. F. CHEN (1984), On Strain-Space Plasticity Formulation for Hardening-Softening Materials with Elasto-Plastic Coupling, Structural Engineering Report, CE-STR-84-85, School of Civil Engineering, Purdue University, West Lafayette, Indiana.

HEGEMIER, G. A. and H. E. READ (1985), On Deformation and Failure of Brittle Solids: Some Outstanding Issues, Mechanics of Materials, 4, 215–259.

HILLERBORG, A., M. MODÉER and P. E. PETERSON (1976), Analysis of Crack Formation and Crack Growth in Concrete by means of Fracture Mechanics and Finite Elements, Cement & Concrete Research, 6(6), 773–782.

HILSDORF, H. (1965), Die bestimmung der Zweiachsiger Festigkeit des Betons, Deutscher Ausschuss für Stahlbeton, Heft 173.

HORII, H. and S. NEMAT-NASSER (1985), Compression-Induced Microcrack Growth in Brittle Solids: Axial Splitting and Shear Failure, J. Geophys. Res., 90, 3105–3125.

HSU, T. T. C. et al. (1963), Microcracking of Plain Concrete and the Shape of the Stress-Strain Curve, ACI Journal, 60(2), 209–224.

HUGHES, B. P. and J. E. ASH (1970), Anisotropy and Failure Criteria for Concrete, Materials and Structures, RILEM, 3(18), 371–374.

HURLBUT, B. (1985) Experimental and Computational Strain-Softening Investigation of Concrete, MS Thesis, Civil Engineering Department, University of Colorado, Boulder.

ISENBERG, J. (1968), Properties of Concrete change when Microcracking occurs, in Causes, Mechanism and Control of Cracking in Concrete, ACI Special Publication SP-20, 29–41.

JAMET, P., A. MILLARD and G. NAHAS (1984), Triaxial Behaviour of a Micro-concrete Complete Stress-Strain Curves for Confining Pressures Ranging from 0 to 100 MPa, RILEM-CEB Symposium on Concrete under Multiaxial Conditions, INSA Toulouse, vol. 1, 133–140.

KACHANOV, M. (1986), Elastic Solids with many Cracks and Crack-Damage Interactions, lecture, presented at Delft University of Technology, June 25, 1986.

KO, H. Y. and S. STURE (1974), Three-dimensional Mechanical Characterization of Anisotropic Composites, Journal of Composite Materials, 8(4), 178–190.

KOBAYASHI, S. and W. KOYANAGI (1972), Fracture Criteria of Cement Paste, Mortar and Concrete Subjected to Multiaxial Compressive Stresses, in Proceedings RILEM Symposium on The Deformation and the Rupture of Solids Subjected to Multiaxial Stress, paper I/9, 131–148.

KOTSOVOS, M. D. (1983), Effect of Testing Techniques on the Post-Ultimate Behaviour of Concrete in Compression, Materials and Structures, RILEM, Vol. 16, no. 91, 3–12.

KUPFER, H. B. (1973), Das Verhalten des Betons unter Mehrachsiger Kurzzeitbelastung unter besonderer Berücksichtigung der Zweiachsiger Beanspruchung, Deutcher Ausschuss für Stahlbeton, Heft 229, Teil I.

LABUZ, J. F., S. P. SHAH, and C. H. DOWDING (1985), Experimental Analysis of Crack Propagation in Granite, Int. J. Rock Mech. Min. Sci. & Geomech. Abstr., 22(2), 85–98.

LABUZ, J. F. (1985), A Study of the Fracture Process Zone in Rock, PhD dissertation, Northwestern University, Evanston, Illinois.

LAUNAY, P., H. GACHON and P. POITEVIN (1970), Déformation et Résistance ultime du Béton sous étreinte Triaxiale, Annales de l'institut technique du Bâtiment et des Travaux Publics, no. 269, 23–48.

LINSE, D. (1978), Lösung Versuchstechnischer Fragen bei der Ermittlung des Festigkeits und Verformungs Verhaltens von Beton unter Dreiachsiger Belastung, Deutcher Ausschuss für Stahlbeton, Heft 292.

LIU, T. C. Y., A. H. NILSON and F. O. SLATE (1972), Stress-Strain Response and Fracture of Concrete in Uniaxial and Biaxial Compression, ACI Journal, 69(5), 291–295.

MEIER, R. W., H. Y. KO and S. STURE (1985), A Direct Tensile Loading Apparatus Combined with a Cubical Test Cell for Testing Rocks and Concrete, Geotechnical Testing Journal, GTJODJ, 8(2), 71–78.

MICHELIS, P. N. and C. A. DEMIRIS (1984), Conception et Construction d'une Vraie Cellule Tri-axiale, C. R. Acad. Sc. Paris, t.299, Série II, no. 8, 375–378.

MICHELIS, P. N. (1985a), A True Triaxial Cell for Low and High Pressure Experiments, Int. J. Rock Mech. Min. Sci. & Geomech. Abstr., 22(3), 183–188.

MICHELIS, P. N. (1985b), Polyaxial Yielding of Granular Rock, J. Eng. Mech., ASCE, 111(8), 1049–1066.

MILLS, L. L. and R. M. ZIMMERMANN (1970), Compressive Strength of Plain Concrete under Multiaxial Loading Conditions, ACI Journal, 67(10), 802–807.

MOAVENZADEH, F. and R. KUGUEL (1969), Fracture of Concrete, Journal of Materials, 4(3), 497–519.

MOSS, W. C. and Y. M. GUPTA (1982), A Constitutive Model Describing Dilatancy and Cracking in Brittle Rocks, J. Geophys. Res., 87, 2985–2998.

NELISSEN, L. J. M. (1972), Biaxial Testing of Normal Concrete, HERON, 18(1).

NEWMAN, J. B. (1979), Concrete under Complex Stress, in Developments in Concrete Techno-logy -1, ed. F. D. Lydon, Applied Science Publishers ltd., London, 151–220.

NEWMAN, K. and O. T. SIGVALDASON (1965/66), Testing Machine and Specimen Characteristics and their Effect on the Mode of Deformation, Failure and Strength of Materials, Proc. Inst. Mech. Engrs., Vol. 180, Part 3A, 399–410.

ORTIZ, M. (1985), A Constitutive Theory for the Inelastic Behaviour of Concrete, Mechanics of Materials, 4(1), 67–93.

ORTIZ, M. (1986), An Analytical Study of the Localized Failure Modes of Concrete, paper sub-mitted to J. Eng. Mech., ASCE.

OTTOSEN, N. S. (1984), Evaluation of Concrete Cylinder Tests Using Finite Elements, J. Eng. Mech., ASCE, 110(3), 465–481.

PALANISWAMY, R. and S. P. SHAH (1974), Fracture and Stress-Strain Relationship of Concrete under Triaxial Compression, J. Struct. Div., ASCE, 100(5), 901–916.

PATERSON, M. S. (1978), Experimental Rock Deformation – The Brittle Field, Springer Verlag.

PETERSON, P. E. (1981), Crack Growth and Development of Fracture Zones in Plain Concrete and Similar Materials, Report TVBM-1006, Division of Building Materials, University of Lund, Sweden.

PODGORSKI, J. (1985), General Failure Criterion for Isotropic Media, J. Eng. Mech., ASCE, 111(2), 188–201.

READ, H. E. and G. A. HEGEMIER (1984), Strain-Softening of Rock, Soil and Concrete – A Review Article, Mechanics of Materials, 3, 271.

REINHARDT, H. W. (1984), Fracture Mechanics of an Elastic Softening Material like Concrete, HERON, 29(2).

ROTS, J. G., P. NAUTA, G. M. A. KUSTERS and J. BLAAUWENDRAAD (1985), Smeared Crack Ap-proach and Fracture Localization in Concrete, HERON, 30(1).

ROTS, J. G. (1985), Strain-Softening Analysis of Concrete Fracture Specimens, in Proceedings Int. Conf. on Fracture Mechanics of Concrete, ed. F. H. Wittman, EPF Lausanne, Oct. 1–3, 1985, 115–126.

ROY, H. E. H. and M. A. SOZEN (1964), Ductility of Concrete, in ACI Special Publication SP 12, Flexural Mechanics of Reinforced Concrete, 231–235.

SAMMIS, C. G. and M. F. ASHBY (1985), The Failure of Brittle Porous Solids under Compressive Stress States, to appear in Acta. Met.

SCAVUZZO, R., T. STANKOWSKY, K. H. GERSTLE, and H. Y. KO (1983), Stress-Strain Curves of Concrete under Multiaxial Load Histories, Research Report, CEAE Department, University of Colorado, Boulder, Colorado.

SCHICKERT, G. and H. WINKLER (1977), Versuchsergebnisse zur Festigkeit und Verformung von Beton bei Mehraxialer Druckbeanspruchung, Deutscher Ausschuss für Stahlbeton, Heft 277.

SCHICKERT, G. (1980), Schwellenwerte beim Betondruckversuch, Deutscher Ausschuss für Stahlbeton, Heft 312.

SHAH, S. P. and F. J. McGARRY (1971), Griffith Fracture Criterion and Concrete, J. Eng. Mech. Div., ASCE, 97(6), 1663–1676.

STEVENS, J. L. and D. J. HOLCOMB (1980), A Theoretical Investigation of the Sliding Crack Model of Dilatancy, J. Geophys. Res., 85, 7091–7100.

STROEVEN, P. (1973), Some Aspects of the Micromechanics of Concrete, PhD dissertation, Delft University of Technology, Delft, The Netherlands.

STURE, S. and C. S. DESAI (1979), Fluid Cushion Triaxial or Multiaxial Testing Device, Geotechnical Testing Journal, GTJODJ, 2(1), 20–33.

Sture, S. and H. Y. KO (1978), Strain-Softening of Brittle Geologic Materials, Journ. Num. Anal. Methods in Geo. Mech., Vol. 2, 237–253.

SUARIS, W. and S. P. SHAH (1982), Mechanical Properties of Materials Subjected to Impact, in Proceedings of the Symposium on Concrete Structures under Impact and Impulsive Loading, Introductory Report, BAM Berlin, June 2–4 1982, 33–62.

TAIT, R. B. and G. G. GARRET (1986), In Situ Double Torsion Fracture Studies of Cement Mortar and Cement Paste inside a Scanning Electron Microscope, Cement & Concrete Research, 16(2), 143–155.

VAN MIER, J. G. M. (1984a), Complete Stress-Strain Behaviour and Damaging Status of Concrete under Multiaxial Conditions, in RILEM-CEB symposium on Concrete under Multiaxial Conditions, INSA Toulouse, session 3, experimental results, pp. 75–85.

VAN MIER, J. G. M. (1984b), Strain-Softening of Concrete under Multiaxial Loading Conditions, PhD dissertation, Eindhoven University of Technology, Eindhoven, The Netherlands.

VAN MIER, J. G. M. (1985), Influence of Damage Orientation Distribution on the Multiaxial Stress-Strain Behaviour of Concrete, Cement & Concrete Research, 15(5), pp. 849–862.

VAN MIER, J. G. M. (1986a), Multiaxial Strain-Softening of Concrete, part I: Fracture, Materials and Structures, RILEM, Vol. 19, no. 111, pp. 179–190.

VAN MIER, J. G. M. (1986b), Multiaxial Strain-Softening of Concrete, part II: Load-histories, Materials and Structures, RILEM, Vol. 19, no. 111, pp. 190–200.

VAN MIER, J. G. M. and R. DE BORST (1986), 2D Representation of 3D Limit Surfaces, To appear as Technical Note in J. Eng. Mech, November 1986.

VERMEER, P. A. and R. DE BORST (1984), Non-associated Plasticity for Soils, Concrete and Rock, HERON, 29(3).

WINKLER, H. (1985), Grundsätzliche Untersuchungen zum Geräteeinfluss bei der mehraxialen Druckprüfung von Beton, Deutcher Ausschuss für Stahlbeton, Heft 366.

WITTMANN, F. H. (1982), Creep and Shrinkage Mechanisms, in Creep and Shrinkage in Concrete Structures, ed. by Z. P. Bažant and F. H. Wittmann, Wiley.

Uniaxial compression and tension results for series 8/9
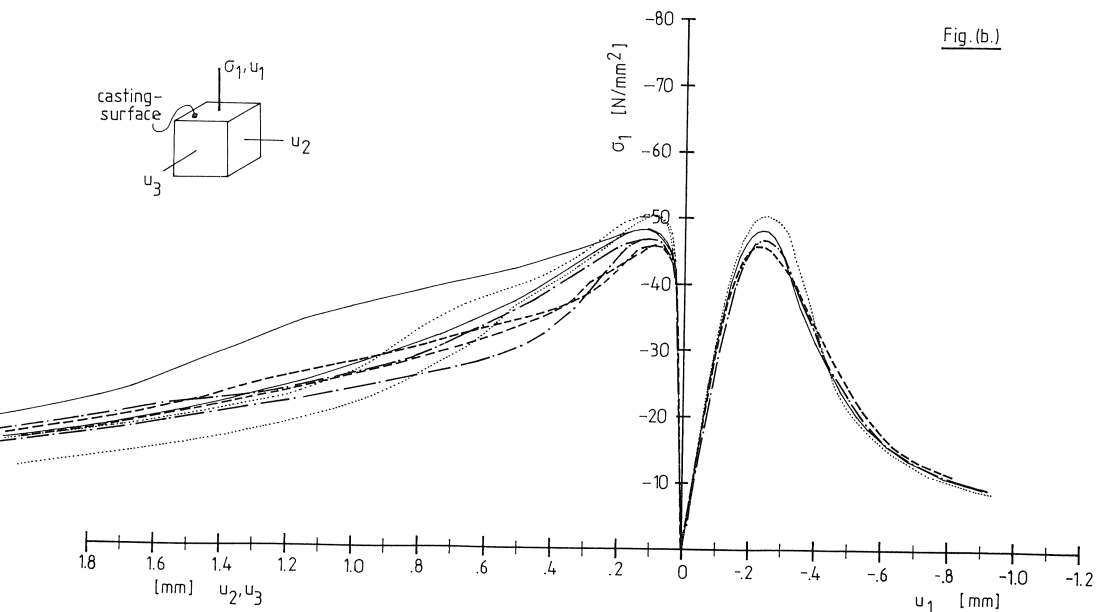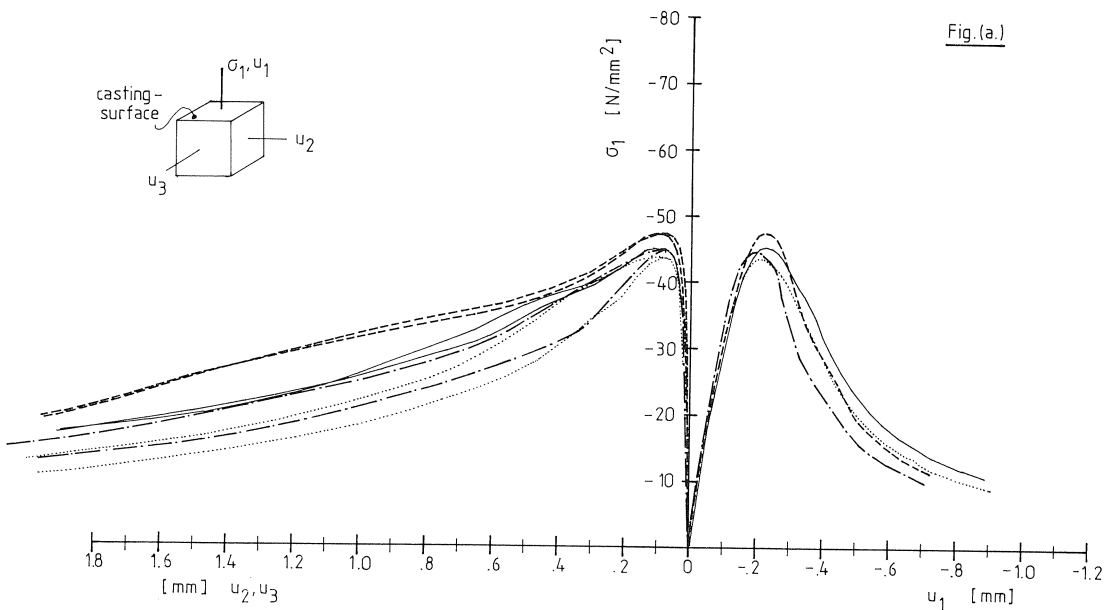
A1. Uniaxial compressive stress-displacement curves for batch 8A/8B (Fig. a), and for batch 9A/9B (Fig. b).
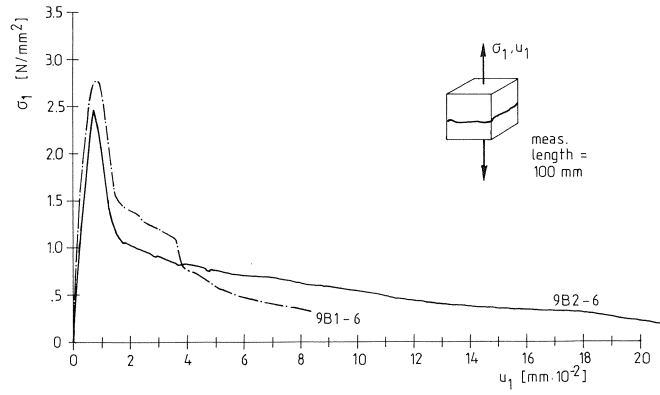
A2. Uniaxial tensile stress-displacement curves for batch 9B (specimens 9B1–6 and 9B2–6).